Single optically active defects in semiconductors for quantum technologies : from the NV center in diamond to single defects in silicon

Alrik Durand

To cite this version:

Alrik Durand. Single optically active defects in semiconductors for quantum technologies : from the NV center in diamond to single defects in silicon. Electronics. Université Montpellier, 2021. English. NNT : 2021MONTS128 . tel-04120217

HAL Id: tel-04120217
https://theses.hal.science/tel-04120217
Submitted on 7 Jun 2023

THÈSE POUR OBTENIR LE GRADE DE DOCTEUR DE L'UNIVERSITÉ DE MONTPELLIER

En Physique

École doctorale : Information, Structure, Systèmes

Unité de recherche UMR 5221

Single optically active defects in semiconductors for quantum technologies:
From the NV center in diamond to single defects in silicon

Présentée par Alrik DURAND
Le 15 décembre 2021

Sous la direction de Vincent JACQUES
et Anaïs DRÉAU

Devant le jury composé de

Eleni DIAMANTI, Directrice de recherche, LIP6 - Paris	Rapportrice
Carole DIEDERICHS, Maitresse de conférences, LPENS – Paris	Rapportrice
Éric ANGLARET, Professeur, L2C - Montpellier	Président du jury
Gabriel HÉTET, Maître de conférences, LPENS - Paris	Examinateur
Jean-Philippe POIZAT, Directeur de recherche, Institut Néel – Grenoble	Examinateur
Guillaume CASSABOIS, Professeur, L2C - Montpellier	Invité
Anaïs DRÉAU, Chargée de recherche, L2C - Montpellier	Co-encadrante de thèse
Vincent JACQUES, Directeur de recherche, L2C – Montpellier	Directeur de thèse

UNIVERSITÉ
DE MONTPELLIER

Acknowledgements

During the three and half years, I spent at the Laboratoire Charles Coulomb as a PhD student, I really have the feeling that I had a great chance to work and interact with exceptional people, both scientifically and humanly.

First, I would like to thank the S2QT team, which was like a second family for me during all this time. In particular, I would like to thank Anaïs Dréau, my thesis supervisor and "Jedi master" for her advices, her support and hey joyfulness. I would like to thank Vincent Jacques, my thesis director, for his unwavering support and the sharpness of his remarks.

I owe a lot to Guillaume Cassabois for the time he spent answering my never-ending puzzling questions about the physics of defects in silicon, Pierre Valvin for his constant help in the lab and for the galaxies and nebulas he made me discover. I also want to acknowledge the help from the other permanent researchers of the team: Isabelle Robert-Philip, Bernard Gil and since recently, Aurore Finco.

I need to thank all the PhD students I've worked with during these last three years, in particular Walid Redjem and Yoann Baron, with whom I shared the study of single defects in silicon, but also Thomas Pelini, Rana Tanos, Angela Haykal, Florentin Fabre, Maxime Rollo and Adrien Rousseau.

This thesis would not have been possible without the help of our many researchers from other institutions. Primarily, Jean-Michel Gérard at CEA Grenoble for his simulations on the light emission and the invaluable purified silicon samples. Tobias Herzig and Sébastien Pezzagna at Leipzig University for the actual creation of all these beautiful single defects. Marco Abbarchi at Marseille University for his help with the flash annealing. Adam Gali and Péter Udvarhelyi in Budapest University for the theoretical modelling of the G and W centers, as well as for taking the time to explain them to us! Lukas Razinkovas and Audrius Alkauskas at Vilnius University for helping us understand our measurements on the NV center, even two years afterwards.

My thanks also go to Carole Diedrichs, Eleni Diamanti, Éric Anglaret, Gabriel Hétet and Jean-Philippe Poizat for doing me the honor of being part of the defence jury of my thesis. I also thank Éric Anglaret for chairing this jury, as well as Carole Diedrichs and Eleni Diamanti for agreeing to be "rapportrices".

I want also to thank Pierre Lefebvre, director of the Laboratoire Charles Coulomb, for welcoming me in the laboratory, where I had a wonderful time. From all the people at L2C, I especially want to thank as well Christian Lhenoret and Thomas Cohen for the mechanical parts, Yves Treguier and Remi Jelinek for the help with the electronics, Laurent Nehlig for the

IT support, and the many people who supported my activities, including Béatrice Tomberli, Jean-Christophe Art and Stéphanie Martegoutes.

I owe the opportunity of this thesis to the DGA, as well as to the I2S doctoral school, which put their faith in me and agreed to finance my work.

Finally, I would like to thank all the people with whom I've spent my time outside the lab, and who helped me survive the writing of this manuscript. My gratitude especially goes to Charlène and for her support and her encouragement. Last, I thank my family for their continual help and trust during all these years.

Contents

Introduction

Scientific advances induced by the development of quantum mechanics at the beginning of the 20th century have enabled many technological breakthroughs. Understanding the behavior of matter at the atomic scale and its interaction with light gave rise to the *first quantum revolution*. This has produced many commonplace technological items such as the transistor which is at the core of all microprocessors, the LEDs for lighting, the ubiquitous laser for telecommunications, optical reading, cutting or 3D-printing, and magnetic resonance imaging in medicine. At the end of the 20th century, scientific and technical progress has led to a paradigm shift from the control of large sets of quantum systems to that of individual quantum systems. This *second quantum revolution* [1] has given birth to quantum technologies, that aim to exploit the properties of quantum mechanics to create new devices offering capabilities which are either better than the standard technologies, or do not possess any equivalence in the classical realm. These innovations include in particular ultrasensitive nanoscale sensors [2], communications whose security is ensured by quantum laws [3], simulators to investigate complex systems [4] or computers with processing performances unattainable for their classical counterparts [5].

The basic block of quantum technologies is the quantum bit or *qubit*. It is a two-level quantum system whose state can be initialized, coherently manipulated and measured. The physical platforms to implement these qubits are diverse. First of all, there are the quantum systems referred to as “natural” such as cold atoms or trapped ions in vacuum [6], or single photons [7]. Then there are the solid-state qubits that include among others superconducting circuits based on Josephson junctions [8], quantum dots electrically controlled [9] or interfaced with light [10], single dopants detected by electrical means [11] or optically active spin defects in semiconductors [12]. The focus of this PhD work is on these latter systems.

Optically active spin defects for quantum technologies

Spin defects are fluorescent point defects in semiconductors. They can be made of impurities, vacancies, interstitial atoms, or their aggregates. Their ability to localize electrical charges produces a discrete structure of energy levels buried inside the bandgap of the semiconductor, as shown in figure 1. Since they can be excited with laser light and subsequently emit luminescence, these systems behave as solid-state artificial atoms. The detection of their photoluminescence by optical confocal microscopy enables to isolate them at single-defect scale. They then act as single-photon sources useful for applications in quantum cryptography and quantum communications. Some of these fluorescent defects possess an additional quantum resource: a non-zero electron spin whose magnetic resonance can be detected optically. This spin can be used as nanoscale quantum sensors [2], or to store or process quantum information when coupled to other spins and quantum systems.

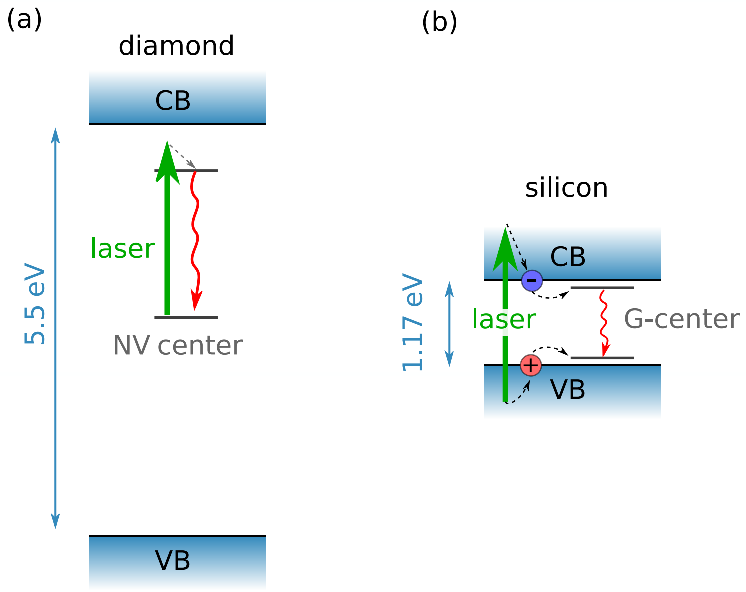

Figure 1: (a) Photoluminescence from the NV center of diamond under green laser excitation. The defect is excited by the absorption of a green laser photon and then emits photoluminescence. **(b)** Photoluminescence from the G-center of silicon under green laser excitation. The above-bandgap laser creates free carriers which are captured by the defects such as the G-center and then leads to a luminescence. CB: Conduction band. VB: Valence band.

In this context, the most studied spin defect is by far a color center of diamond called the nitrogen-vacancy (NV) center (figure 1(a)). It has been detected for the first time at the single-defect scale in 1997 by Gruber *et al.* [13] and investigated intensively for quantum applications since then. Its first use was to demonstrate quantum key distribution using its emission of single photons [14]. But it is mainly its spin properties that make the NV center in diamond an exceptional quantum system because it can serve as a long-lived spin qubit with coherence time reaching 1 ms at room temperature [15]. It has been used to probe at the nanoscale different physical quantities such as magnetic field [16], electric field [17], temperature [18], pressure [19] or magnetic noise [20]. Single-spin scanning magnetometers based on NV centers in diamond are now even commercially available [21]. The electron spin of the NV defect can also be coupled to nuclear spins located nearby in the diamond lattice to create spin registers, currently up to 10 qubits, to implement quantum algorithms [22]. Cooled down at 8K, the electron spin of the defect can be entangled with the single photons it emits. This spin-photon interface allows to remotely generate entanglement between NV centers that are more than one kilometer apart. As the recent demonstration of a 3-node local quantum network indicates [23], the NV center in diamond is one of the most promising candidates in the race to build a quantum communication network. However, a larger-scale implementation of such architecture is hindered by the strong absorption of the NV center emission (around 637 nm) during optical fiber propagation. Furthermore, the diamond is not a platform adapted to wafer-scale industrial processes. To overcome these two drawbacks, one solution relies on investigating other spin defects, which would provide a direct emission at telecom wavelength in materials commonly used in the semiconductor industry.

Silicon carbide (SiC) has opened the way in 2015 with the first isolation of two individual spin defects emitting in the near-infrared [24]. This discovery combined with the SiC technological advantages - in particular with doping and nanofabrication compared to diamond - has launched a boom of SiC research for quantum technologies [25]. Overall, fifteen fluorescent spin defects are currently being investigated in SiC polytypes [12]. Since then, numerous other wide-bandgap semiconductors have followed, with single luminescent defects detected notably in zinc oxide [26], gallium nitride [27] or in 2D-materials like hexagonal boron nitride and transition metal dichalcogenides [28]. Intense experimental and theoretical research efforts are currently invested to understand and control the quantum properties of these single emitters, and establish if they potentially host a spin state useable as a qubit. However in this list of promising semiconductor materials is lacking the ideal platform for large-scale nanotechnologies: silicon. This semiconductor has been overlooked due to its small bandgap of 1.17 eV, five times smaller than the one of diamond (figure 1).

Silicon-based quantum technologies

Silicon is the flagship material of the microelectronics industry. The CMOS process enables complex integration of transistors of only a few tens of nanometers wide on 300-mm single-crystal silicon wafers. On the quantum side, silicon-based electrical qubits, involving either individual dopants [29] or gate-defined quantum dots [9], have already been used to demonstrate the elementary building blocks of scalable integrated quantum circuits. Recently the first electrical quantum chip has been produced from a silicon-on-insulator (SOI) wafer on a manufacturing product line [30]. These individual electrical qubits can be efficiently controlled and detected by all electrical means but have the drawback of being weakly coupled to light [31] or emitting in the mid-infrared range [32] unsuitable for optical fiber propagation. From the optical point of view, silicon is also a valuable platform for integrated photonics whether classical or quantum [33]. Photonic quantum chips able to implement arbitrary 2-qubit gates on photonic qubits have already been fabricated on SOI samples with CMOS-compatible processes [34]. However even if these photonic qubits operate at telecom wavelengths, they are generated inside silicon by probabilistic nonlinear optical processes and therefore cannot be coupled to stationary matter systems, constraining the functionalities of scalable silicon quantum photonics. Individual optically active defects with spin control could fill this gap, but are still lacking in silicon [12].

Fluorescent defects in silicon for quantum technologies

Optically active defects in silicon have been investigated extensively on ensemble measurements since the 1960s. Optical spectroscopy has enabled to identify more than 100 optical lines associated with different families of defects emitting in the near-infrared range [35]. For the moment only a few color centers in silicon are being investigated for quantum applications. A promising defect is for example the T-center in silicon, a complex based on silicon and hydrogen, linked to a telecom emission around 1.3 µm. The coherent control of the electron spin belonging to an ensemble of T-centers created in ^{28}Si was demonstrated in 2020, with associated coherence times exceeding 1 ms [36]. These results have been followed this year by the signature of single-T-defect addressability under resonant excitation [37]. Another promising defect is formed by erbium dopants which have the advantage of presenting extremely narrow optical lines in the telecom band around 1.55 µm. Ensembles of erbium ions have recently been successfully created in silicon waveguides [38]. The disadvantage of these first two defects is that the lifetime of their excited state is very long, respectively 1 µs and 1 ms for T-centers and erbium ions. Their detection at single-defect scale, that is still to be demonstrated, is therefore extremely challenging due to the very low photon emission rates.

Thesis outline

Before searching for individual optically active defect in silicon, I started my PhD by studying the photoluminescence properties of the NV defect in diamond.

The first chapter of the thesis is devoted to the analysis of the dynamics of charge state fluctuations of the NV center in diamond under optical excitation. While being optically illuminated, the NV center in diamond continuously loses and gains an electron, which makes it constantly alternate between the neutral charge state NV^0, and the negatively charge state NV^- that is the one with the interesting spin properties for quantum technologies. Although this defect has been investigated at the single-defect scale for more than two decades, its dynamics under optical illumination is still not fully understood. First, we will present the state of the art of the spin photodynamics of the NV^- center. Next, we will show that the optical excitation cycles populate a long-lived dark state which is in fact a metastable level in the energy level structure of NV^0. Finally, we will develop a new model which encompasses these dynamics and explains other phenomena of the photophysics of the NV center in diamond that were still misunderstood.

The main goal of my PhD was then to demonstrate the optical detection of single fluorescent defects in silicon. At the start of my thesis, it was unclear whether silicon, due to its small bandgap, could accommodate single optically-active defects with electronic states well isolated from its valence and conduction bands. My strategy was to explore a very common carbon complex in silicon called the G-center. The interest for this defect relies first on its emission in the telecom O-band around 1.3 µm [39], that is therefore suitable for long-distance propagation in optical fibers. Secondly, an electron spin has been previously detected via optically-detected magnetic resonance (ODMR) measurements performed on ensembles in the 1980's [40,41]. Furthermore, research initiated in my research team before my arrival has shown that this defect possesses a short lifetime of roughly 6 ns, which could enable its detection at single-defect scale [39].

To be able to detect individual fluorescent centers in silicon, I have built a new low-temperature microspectroscopy experiment. The analysis of a carbon-implanted silicon sample has first led to the isolation of individual emitters associated with unidentified families of fluorescent defects. Then, weakly implanted samples with respectively carbon and silicon atoms have enabled to detect on an individual scale two defects well known in the literature: the G-center mentioned above, and the W-center in silicon, a fluorescent defect based on interstitial silicon atoms.

The second chapter of this manuscript is devoted to the first detection of individual optically-active defects in silicon. First, we will detail the characteristics of the experimental setup, a low-temperature confocal microscope optimized for the detection of single emitters in the near infrared with an above-bandgap optical excitation (see figure 1 (b)). This new experimental setup has enabled to isolate seven families of fluorescent defects in a carbon-implanted silicon sample, that are not referenced in the literature. These single emitters all emit in the near-infrared, and even at telecom wavelengths for some of them. We will first focus on the most commonly found defect and analyze in detail the properties of its single photon emission and its dynamics under optical excitation. We will then investigate the other six families of single defects and carry out a comparative study of their spectral properties, single photon emission properties and photodynamics.

The third chapter will focus on the detection of single G-centers and single W-centers. First, we will focus on the G-center isolated on an individual scale in a sample with low carbon implantation. After investigating the photophysics of single G-centers, we will show that the analysis of their photon polarization and of their optical fine structure reveals a rotation dynamics of the G-center around its crystalline axis, which varies from one defect to another. Secondly, we will demonstrate the first optical isolation of an intrinsic defect in silicon, the W-center, in a sample implanted with silicon atoms. The spectroscopy and photon emission study of these individual defects will reveal new physical properties of this common radiation damage center in silicon, such as its dipolar emission and coupling to its environment.

Chapter 1

Dynamics of charge state conversion of the NV center in diamond

Contents

Introduction

The negatively-charged nitrogen-vacancy (NV^-) center of diamond is one of the most widely studied spin defect for quantum technologies. Since its first isolation at the single scale in 1997 [13], it has been extensively investigated owing to its remarkable optical and spin properties. The NV^- defect was used in many proof-of-concept experiments such as a single-photon source for quantum cryptography [14], a solid-state spin qubit for quantum information science [42], and a nanoscale quantum sensor of magnetic fields [16], electric fields [17], temperature [18] or magnetic noise [20] over a large range of temperatures including above 300 K. Commercial devices using NV^- centers for sensing are now available for labs across the world [21]. At low temperature, the NV^- defect also provides a robust spin-photon interface, which has been used to entangle two spin-defects separated by 1.3 km [43].

Despite extensive studies, some aspects of the NV^- center photophysics still remain to be clarified, such as the dynamics of its charge state fluctuations. Conversion between the different charge states have been investigated both theoretically [44, 45] and experimentally [46–50], but no clear picture of the complete charge conversion mechanisms is available to date. A recent theoretical work [51] predicts the presence of several ionization processes that would switch the NV center from its negatively charged state NV^- to its neutral charged state NV^0. One of these processes includes a transition through a metastable level of NV^0. In this chapter, we detect for the first time the populations trapped in this metastable level by using an original method based on time-resolved photoluminescence. We then build a new model to describe the dynamics of the NV center in diamond under optical excitation.

In a first section, we present the properties of the negatively charged NV^- center and introduce the simple model commonly used to understand its spin-dependent photodynamics (**§1.1**). In a second section, we detect the presence of the NV^0 metastable level and measure experimentally its lifetime and recombination dynamics (**§1.2**). Finally, in a third section, we build a new model of the defect photophysics under optical illumination at room temperature, which takes into account the charge state conversion dynamics (**§1.3**).

1.1 Photophysics of the NV^- center in diamond

1.1.1 Presentation of the NV^- center

The NV^- center is a defect of diamond formed by a substitutional nitrogen atom sitting next to a vacancy in the carbon lattice (figure 1.1(a)). This system possesses six electrons: three originates from the unpaired electrons of the three carbon atoms adjacent to the vacancy, two are given by the nitrogen atom and one last electron is captured by the defect from the diamond lattice. We will see later that without this last electron, the NV center is found in the neutral charge state NV^0, but for now we focus on the properties of the negatively charged state. The electrons are localized at the position of the defect and lead to deep electronic levels located inside the bandgap of diamond ($E_g \approx 5.5\,\text{eV}$), as sketched in figure 1.1(b). Optical transitions between these electronic levels can lead to photoluminescence of the defect. At room temperature, the NV^- center can be excited with a green laser (532 nm) and then emits fluorescence in the red part of the spectrum, either directly or a via phonon-assisted recombination. The photoluminescence spectrum of a single NV^- center recorded at room temperature is shown in figure 1.1(c). The defect exhibits an emission peak at 637 nm corresponding to the zero-phonon line (ZPL) and a broad phonon-sideband spanning from 650 nm to 850 nm.

1.1.2 Spin-dynamics under optical illumination

The NV^- center possesses two unpaired electrons, leading to a spin triplet ground level ($S = 1$) with three spin projections $m_s = 0$, $m_s = +1$ and $m_s = -1$ along the intrinsic quantification axis of the defect. This axis joins the nitrogen atom and the vacancy, along a $\langle 1\,1\,1 \rangle$ crystal direction. Electron-electron interaction results in a small energy difference between the spin sublevel $m_s = 0$ and the degenerate spin sublevels $m_s = \pm 1$ by an energy $D \approx 2.87\,\text{GHz}$ (figure 1.2).

The defect can be excited from the spin triplet ground level to the first excited level, which

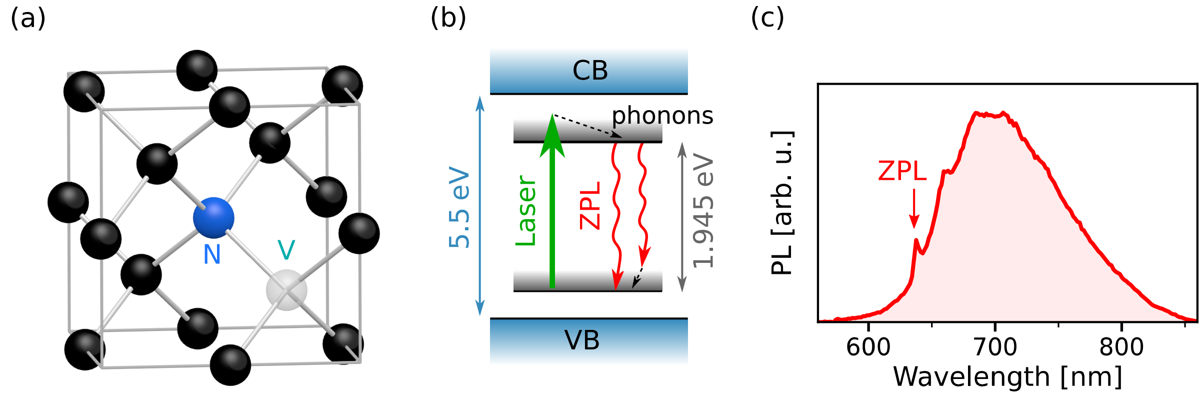

Figure 1.1: The NV$^-$ center of diamond. **(a)** Atomic representation of the NV defect. A substitutional nitrogen atom (blue) sits next to a vacancy (white) in the diamond lattice. **(b)** Simplified energy-level structure of the NV$^-$ center. The NV$^-$ can be excited by a green laser and emits red photoluminescence either at the zero-phonon line wavelength or via phonon-assisted recombination. CB: Conduction band. VB: Valence band. **(c)** Photoluminescence (PL) spectrum of the NV$^-$ center at room temperature. An arrow indicates the position of the zero-phonon line (ZPL) at 637 nm (1.945 eV).

is also a spin triplet, via optical transitions that conserve the spin projection ($\Delta m_s = 0$). Once in the excited level, the NV defect can relax via two possible paths. Either it decays directly to the ground level by emitting a red photon via spin conserving transitions (typical lifetime $\approx$ 10 ns [53]), or it decays non-radiatively through a metastable level, which is a spin singlet ($S = 0$) and has a long lifetime ($\tau_{M^{(-)}} \approx 200$ ns [53]). The probability of the non-radiative decay is spin-dependent and is much more likely for the excited $m_s = \pm 1$ sublevel than for the excited $m_s = 0$ sublevel. From the metastable level, the system ends up with roughly equal probability in the ground sublevels $m_s = 0$ or $m_s = \pm 1$. Such a spin-dependent non-radiative decay is at the heart of the NV center spin polarization under optical illumination, as described below.

Spin polarization and detection by optical illumination

Boltzmann's statistic dictates that the populations of each ground state spin sublevel are $\approx 1/3$ at equilibrium. However under optical illumination, the populations in the $m_s = 0$ sublevel mostly undergo spin-conserving optical transitions, while, on the other hand, the populations in the $m_s = \pm 1$ sublevels are likely to decay via the metastable level and to experience a spin-flip. After a few optical cycles, the probability to be in the $m_s = 0$ sublevel stabilizes around $\approx$80 % [53], corresponding to an efficient spin polarization of the NV$^-$ center electronic spin.

Furthermore, as the populations in the excited $m_s = \pm 1$ sublevels likely undergo non-radiative decay via the metastable level, they generate less photoluminescence than the populations in the $m_s = 0$ sublevel. As a result, the NV$^-$ center photoluminescence directly reflects its spin sublevel populations, which are commonly referred to as the *bright* spin sublevel for $m_s = 0$ and the *dark* spin sublevel for $m_s = \pm 1$. An interesting consequence is that the photolumines-

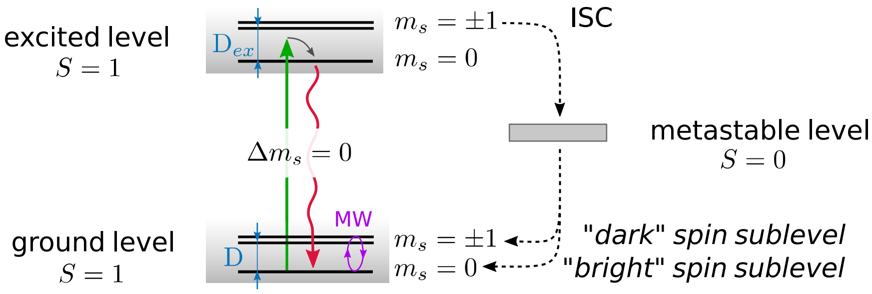

Figure 1.2: NV$^-$ center spin-dynamics under optical illumination. The system can be excited from the spin triplet ground level to the spin triplet excited level via spin-conserving transitions ($\Delta m_s = 0$). It can then decay either radiatively or non-radiatively via intersystem crossing (ISC) through a spin singlet metastable level. The spin-dependent non-radiative decay leads to a spin polarization under optical excitation and to a spin-dependent photoluminescence intensity. The zero-field splitting (ZFS) is $D = 2.87\,\text{GHz}$ for the ground level and $D_{ex} = 1.42\,\text{GHz}$ for the excited level [52].

cence signal can be used to detect the electron spin transitions between the sublevels.

Optically detected magnetic resonance

The optical detection of magnetic resonances (ODMR) is done by recording the fluorescence intensity while sweeping the frequency of a microwave magnetic field. A typical measurement is plotted in figure 1.3(a). When the microwave magnetic field is resonant with one of the electron spin resonance transitions $m_s = 0 \leftrightarrow m_s = \pm1$, it induces a population transfer between the spin sublevels, leading to a 30 % drop in the total photoluminescence. When a magnetic field is applied, the Zeeman effect shifts the energies of $m_s = -1$ and $m_s = +1$, which results in a splitting of the ODMR lines, as shown in figure 1.3(b). Interestingly, each line is shifted by $\pm\gamma_e B$, where $\gamma_e = 28.0\,\text{MHz/mT}$ is the NV center electronic spin gyromagnetic factor. This measurement therefore allows the quantitative measurement of the magnetic field at the position of the NV center, and forms the basis of the applications of NV defects in diamond for magnetic imaging.

In this chapter, all the experiments are performed at zero magnetic field $B = 0$, and the $m_s = \pm1$ sublevels are therefore degenerated.

Coherent control

In addition to continuous excitation, laser illumination and spin manipulation can be performed consecutively in pulsed experiments schemes. A typical sequence to coherently control the NV$^-$ spin is illustrated in figure 1.3(c). The electron spin is initialized into the $m_s = 0$ spin sublevel via a first laser pulse. Then a coherent manipulation of the spin is performed by applying a pulsed microwave magnetic field of duration τ. Finally, the spin state is readout via a second laser pulse. As this second laser pulse re-polarizes the spin after a given time, only the photoluminescence signal recorded at the beginning of the pulse is used for readout. The sequence is repeated a large number of times while increasing the duration τ of the microwave pulse and the resulting signal is plotted in figure 1.3(d). The high photoluminescence level corresponds to spin populations mostly in $m_s = 0$ and the low signal to populations mostly in $m_s = \pm 1$. The oscillation of the signal reflects the coherent manipulation of the NV$^-$ center spin, also referred to as Rabi oscillations.

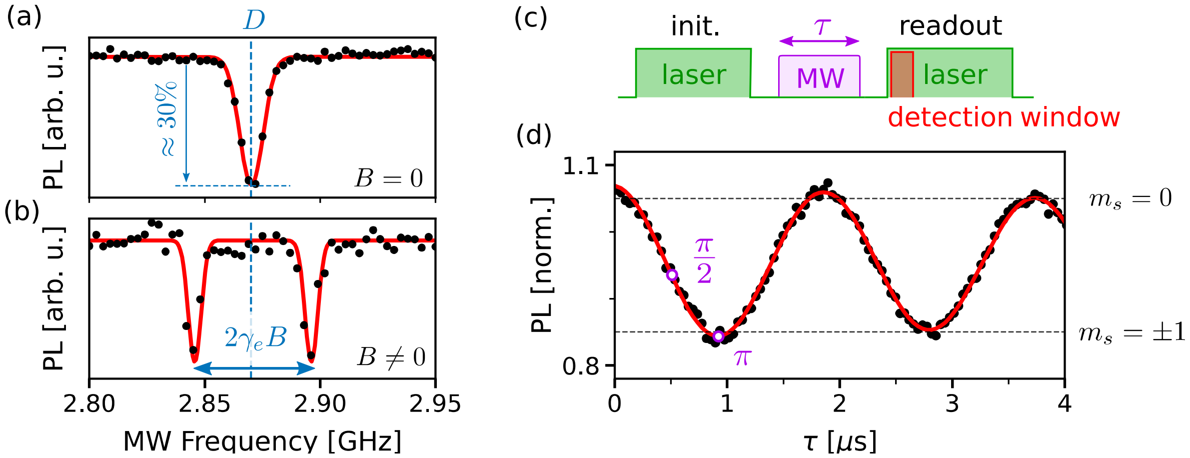

Figure 1.3: Electron spin resonance of the NV$^-$ center. **(a, b)** Optically detected magnetic resonance (ODMR) spectra recorded at zero field (a) and for $B \approx 0.9\,\mathrm{mT}$ (b). The photoluminescence signal is plotted versus the frequency of the applied microwave magnetic field. **(c)** Experimental sequence used to perform the coherent control of the NV$^-$ spin between the $m_s = 0$ and $m_s = \pm 1$ spin sublevels. A first laser pulse polarizes the defect spin populations. A pulse of microwave (MW) magnetic field of length τ manipulates the spin. A second laser pulse readouts the spin state by recording the spin-dependent photoluminescence signal over a detection window of 300 ns at the beginning of the pulse. **(d)** Typical Rabi oscillations signal recorded with the experimental sequence shown in (c). The signal is normalized by the luminescence level at the end of the readout pulse. The measurement allows the determination of the pulse length for a $\pi/2$ pulse where the spin is in a coherent superposition of $m_s = 0$ and $m_s = \pm 1$, or a π pulse where all the populations have been transferred into $m_s = \pm 1$.

The measurement of the Rabi oscillations enables the determination of the duration of a $\pi/2$ pulse which transfers the populations from $m_s = 0$ to a coherent superposition of $m_s = 0$ and $m_s = \pm 1$. Another important duration, which is frequently used in this chapter, is the π pulse which sends most of the ground-level spin populations into $m_s = \pm 1$.

Further understanding of the NV$^-$ center photoluminescence signal in a pulsed laser sequence can be offered by looking at the time-resolved photoluminescence, as discussed in the next subsection.

1.1.3 Time-resolved photoluminescence

The study of the photoluminescence over the nano and microsecond timescale is capital to understand the dynamics of the NV center. Experiments typically involve laser pulses to initialize and readout the state of the defect. Two examples of simple experimental sequences are shown in figure 1.4. The first sequence (figure 1.4(a)) consists of an initialization laser pulse to induce spin polarization into $m_s = 0$. After a time delay in the dark, a second laser pulse is applied to readout the spin populations. A delay of 2 µs is systematically used in this chapter to let the populations trapped in the NV$^-$ metastable level decay to the ground level before the readout pulse. The photoluminescence is recorded with a sub-nanosecond time resolution by detecting the arrival of the photons compared to a synchronization pulse at the start of the sequence. The *time-resolved photoluminescence* is then recorded by repeating the sequence for several millions of iterations in a few seconds, and by building an histogram of the photons detection times. The result obtained while applying this simple sequence is plotted in figure 1.4(b). It displays a photoluminescence signal going from 0 to ≈ 200 kilo·counts per second (kc/s) when the laser is turned on. It first shows an initial spike, then reaches a steady state of photoluminescence. When the laser is turned off, the photoluminescence goes back to zero. The initial spike, commonly called the *overshoot*, is linked to the metastable level of NV$^-$ slowly trapping populations and therefore reducing the level of photoluminescence.

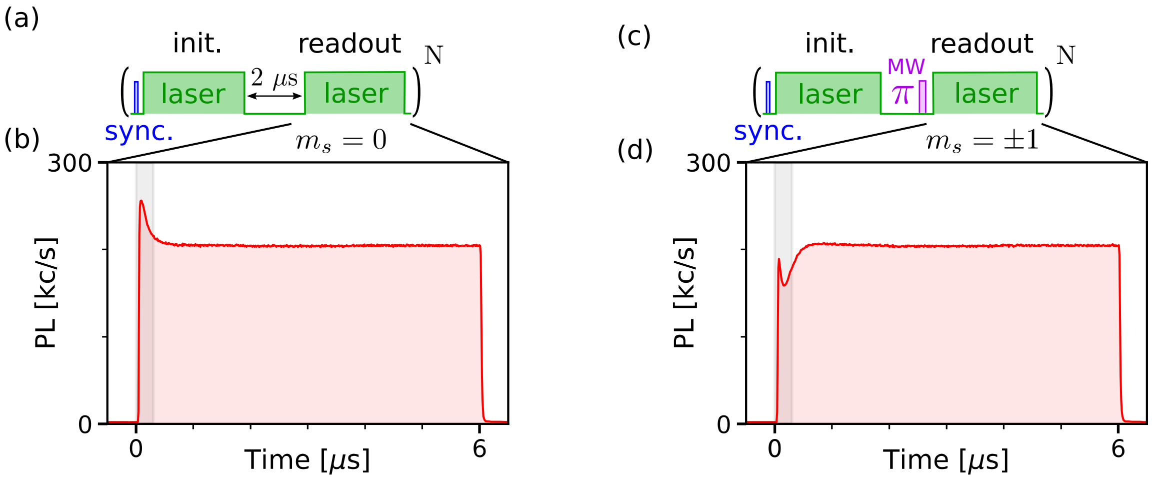

Figure 1.4: Time-resolved photoluminescence of the NV$^-$ center **(a, c)** Laser sequences used to probe the NV$^-$ center evolution. A first 6 µs laser pulse initializes the spin into $m_s = 0$. After 2 µs in the dark, a second laser pulse of 6 µs is applied to read the photoluminescence. In (c) a microwave π pulse is added to transfer the spin populations initially in $m_s = 0$ to $m_s = \pm 1$. A synchronization (sync.) pulse is always used as a reference clock. The sequence is repeated a large number of times (N) to record the photoluminescence signal. **(b, d)** Time-resolved photoluminescence recorded under green laser illumination (400 µW) while applying the sequences shown in (a, c) respectively. The shaded squares at the beginning of the pulses correspond to the windows of 300 ns typically used to integrate the spin-dependent signal.

To investigate the impact of the spin sublevels populations onto the photoluminescence signal, a second experimental sequence (figure 1.4(c)) is performed. After the first laser pulse used to initialize the spin populations into $m_s = 0$, a microwave π pulse is applied to convert the populations to $m_s = \pm 1$. The photoluminescence of the second readout pulse is plotted in figure 1.4(d) and shows some differences with the first measurement. Besides a smaller overshoot linked to the NV$^-$ metastable level, the major difference is the lower photoluminescence signal recorded at the start of the readout laser pulse. This lower luminescence reflects the larger populations in the dark spin sublevel $m_s = \pm 1$ when the laser is switched on. After a few hundred nanoseconds, the signal gets back to the steady state. The difference of photoluminescence signals at the beginning of the readout pulse is at the heart of the spin readout via time-resolved luminescence. In all experiments, a time window of typically 300 ns is used to integrate the spin-dependent signal.

1.1.4 Modeling of the NV$^-$ center dynamics via a 5-level system

A precise understanding of the NV$^-$ center dynamics can help choosing the best experimental conditions for optimizing the spin readout contrast, such as the laser power and the laser delays. To this end, we perform a simulation of the evolution of the spin populations by means of a rate equation model.

To explain the time-resolved photoluminescence signal produced by the NV$^-$ center, the standard method is to use a 5-level model of the defect dynamics [53, 54]. This standard model is illustrated in figure 1.5. It includes 5 levels to represent (i) the NV$^-$ ground levels G$^{(-)}$, (ii) the excited levels E$^{(-)}$ and (iii) the metastable level M$^{(-)}$. The spin conserving optical transitions are described by the laser-dependent pumping rate Π and the radiative recombination rate Γ, while the non-radiative decay via the metastable level is described by the rates k_{ij}. Typical values of the rates found in the literature are given in table 1.1 [54].

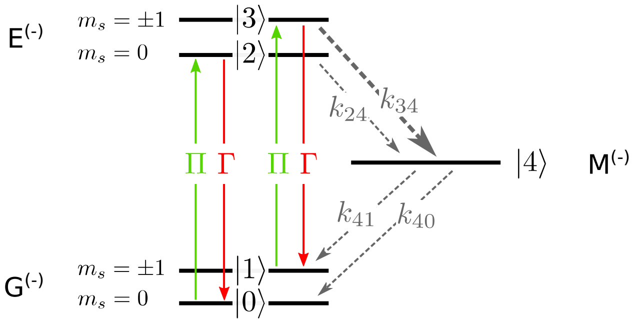

Figure 1.5: 5-level model of the NV$^-$ center dynamics. The spin conserving optical transitions are given by Π and Γ while the non-radiative decay through the metastable level is given by the rates k_{ij}. The typical values of each transition rate are given in table 1.1.

To derive the time-resolved photoluminescence signal from this model, the evolution of the populations can be simulated by solving the linear rate equations. In practice, the matrix of rates associated to the 5 differential equations is computed and diagonalized numerically to evaluate the populations at each time. I developed a custom code in Python to perform this simulation. The result obtained for a laser excitation pulse is shown in figure 1.6. This simulation corresponds to the experiments shown in figure 1.4 for spin populations prepared in either $m_s = 0$ or in $m_s = \pm 1$, by applying an additional microwave π pulse. Upon laser illumination, both the excited levels and metastable level populations increase, while the ground-level pop-

Γ	k_{24}	k_{34}	k_{40}	k_{41}
65.9 MHz	11.4 MHz	92 MHz	4.84 MHz	2.35 MHz
Π	η			
89.2 MHz/mW	1.62×10^{-2}			

Table 1.1: Numerical values of the parameters used in the 5-level model simulation. The rates from the first line are typical rates taken from the literature [54]. The parameters from the second line are setup-dependent and correspond to the laser excitation rate Π and the photon collection efficiency η. Their value was determined by matching the resulting simulation to the experimental data.

ulations decrease. As the defect photoluminescence is at all times linear with the excited-level populations, the photoluminescence signal S is computed as $S = P_{E(-)} \times \eta\Gamma$, where $P_{E(-)}$ is the total population of the excited levels, Γ is the radiative recombination rate, and η is the collection efficiency of the experimental setup (see table 1.1). The experimental photoluminescence signal, as well as the results of the corresponding simulations for several laser powers, are displayed in figures 1.4(c) and (d). The overshoot linked to the populations trapped in $\mathrm{M}^{(-)}$ is quantitatively reproduced, as well as the spin-dependent signal. The signal dependency on the laser power is also well reproduced, confirming the accuracy of the 5-level model to describe these simple experiments.

The 5-level model is commonly used in NV center experiments to explain the photoluminescence dynamics. This model has for example been used to optimize the experimental conditions for measuring the NV^- spin most effectively [54]. However this model does not include the charge state conversion of the NV defect. We will see in section 1.3.2 that this charge state conversion can have a strong impact on the time-resolved photoluminescence signal in some particular experimental conditions. Before describing these results, we first discuss the process of charge state conversion in the next subsection.

1.1.5 Photochromism between charge states

Photochromism is the reversible transformation of a luminescent object between two forms which emit at different wavelengths. In the case of the NV center, the defect can exist in multiple charge states depending on the diamond Fermi level, and on the laser excitation. In bulk ultra-pure diamond crystals and under green laser excitation, which correspond to the standard experimental conditions of many NV center experiments, only the photoluminescence from the negative charge state (NV^-) is visible (see figure 1.1). Illumination of the same defect with a blue laser, on the other hand, generates photoluminescence corresponding to the neutral charge state (NV^0) of the NV centers [55]. The NV^0 photoluminescence is also observed with green illumination in samples where the Fermi level has been modified via doping [55] or in nanodiamonds [56]. Alternatively, the Fermi level can be locally tuned electrically with Schottky junctions to switch dynamically between the two charge states via a voltage control [57]. Under

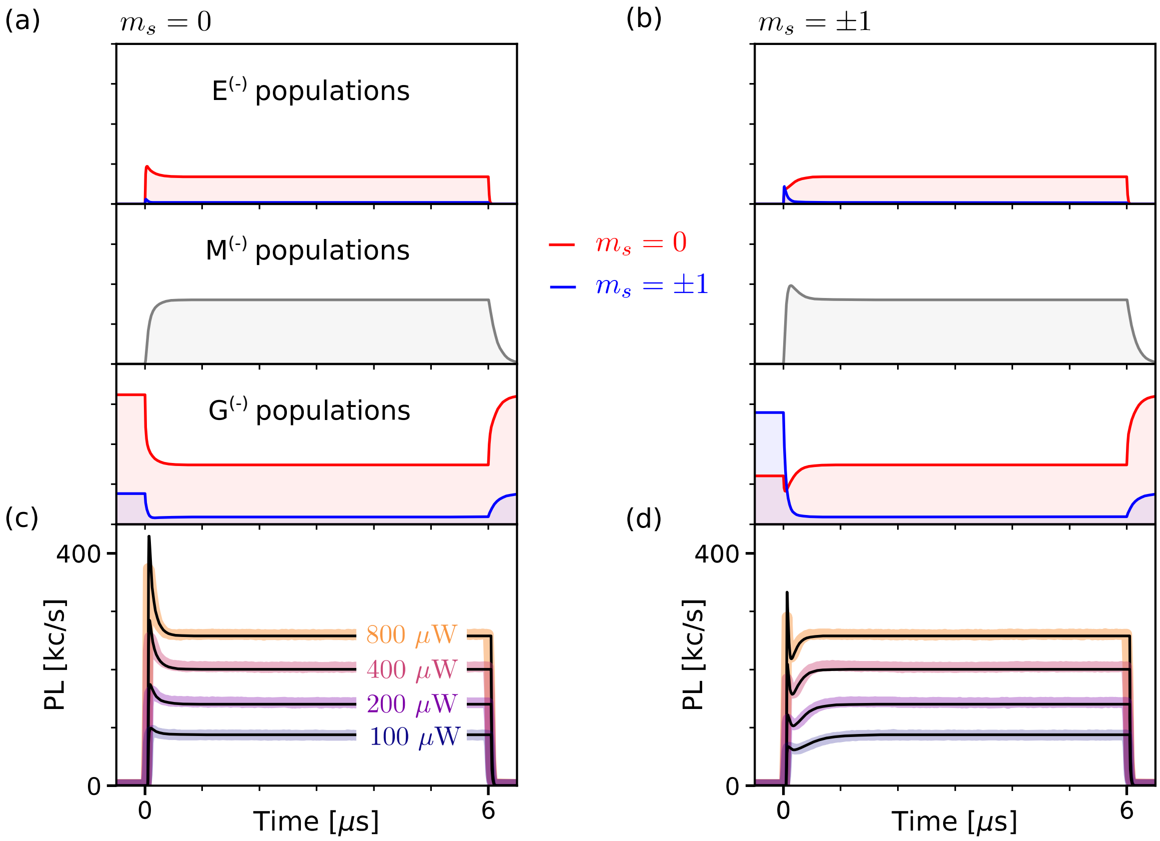

Figure 1.6: Evolution of populations for the 5-level model under pulsed illumination. **(a, b)** Populations given by the simulated 5-level model under the laser sequences shown in figures 1.4(a) and (c), respectively. The populations are plotted between 0 and 100 % for each spin sublevels and correspond to an excitation power of 400 µW. **(c, d)** Time-resolved photoluminescence recorded at four laser powers for both prepared spin sublevel populations. The photoluminescence signal S computed from the 5-level model is superposed as a black line. It is computed by $S = P_{E^{(-)}} \times \eta\Gamma$ where $P_{E^{(-)}}$ is the total excited-levels population.

illumination, charge state switching induced by the laser leads to an equilibrium. Measurements of nuclear magnetic resonance (NMR) have also revealed that under green illumination, the NV centers only spend 70 % of their time in the negative charge state (NV$^-$) and 30 % in a dark state, which was attributed to the neutral charge state (NV^0) [46].

The NV center photochromism can be a detrimental source of error for optical manipulation of the defect. Conversely, this photochromism can be used as a resource: *spin-to-charge conversion* is a protocol using spin-dependent ionization to perform an efficient readout of the NV$^-$ spin state [58]. Another usage of this phenomenon is *ground state depletion microscopy* where a donut shaped laser beam can ionize the NV centers around a focus point while letting the ones in the very center unaffected. Such a method can be used to achieve an optical resolution of 12 nm with an excitation wavelength above 500 nm [59].

Before dealing with the charge state switching mechanisms, we first give a brief description of the neutral charge state of the NV defect.

The NV^0 charge state

The neutral charge state (NV^0) of the NV center has a spin doublet ($S = 1/2$) both in its ground G$^{(0)}$ and excited levels E$^{(0)}$ (figure 1.7(a)). The photoluminescence spectrum of the neutral state consists of a zero-phonon line at 575 nm and a large phonon-sideband up to 750 nm (figure 1.7(a)). The neutral state is also predicted to possess a metastable level M$^{(0)}$ with an electron spin $S = 3/2$ [44]. Up to now, the only measurement corroborating the evidence of this metastable level was an EPR signal associated to a $S = 3/2$ signal measured under optical illumination [60].

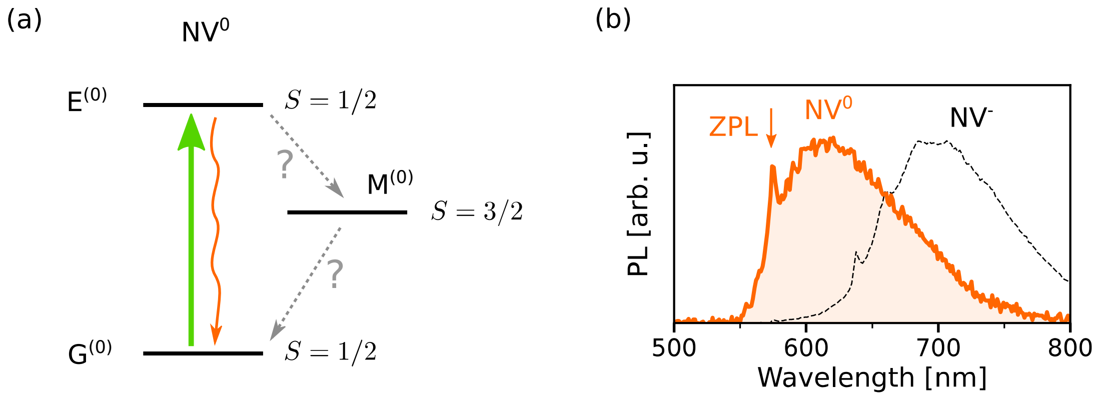

Figure 1.7: Neutral charge state of the NV center of diamond (NV^0). **(a)** Energy level structure of NV^0. Continuous arrows symbolize radiative transitions while dashed arrows are non-radiative decays. **(b)** Photoluminescence spectrum of NV^0 recorded on nano-diamonds at room temperature, taken from [56]. The spectrum of the NV$^-$ from figure 1.1 is reproduced in dashed line for comparison.

Vocabulary note

The NV center has mostly been studied in the negative charge state because of its spin properties, as a result, its conversion to the neutral form NV^0 is generally referred to as *ionization* and the inverse process NV^0 →NV$^-$ as *recombination*. To conform with the NV center literature, we keep this convention.

Ionization processes

Multiple ionization processes have been observed experimentally. The simplest process is a direct ionization from the NV$^-$ ground level, which promotes an electron to the conduction band. This direct ionization requires a wavelength smaller than 477 nm to overcome an energy barrier of 2.6(1) eV [48]. Here we limit ourselves to the processes induced by the standard illumination with a 532 nm green laser and therefore do not consider it further.

Ionization under green laser excitation is a two-photon process [48]. Figure 1.8(a) illustrates one ionization path: the NV$^-$ center first reach the excited level by the absorption of a first green laser photon. Before it has the time to decay, a second absorption sends an electron into the conduction band, resulting in the NV^0 charge state. It was recently pointed out by theory that the resulting level is the NV^0 metastable level, denoted M$^{(0)}$ in figure 1.8(a) [51].

A second two-photon ionization process can happen from the metastable level of NV$^-$ and is depicted in figure 1.8(b). From this metastable level, the defect absorbs a green laser photon, ejecting an electron to the conduction band, and ends up in the ground level of the neutral charge state G$^{(0)}$. This second ionization process has been less investigated and is often not included in the NV centers dynamics models [53, 54]. Theoretical computation have estimated that the absorption cross section from the NV$^-$ metastable level is 14 times smaller compared to that of the NV$^-$ excited level at 532 nm [51].

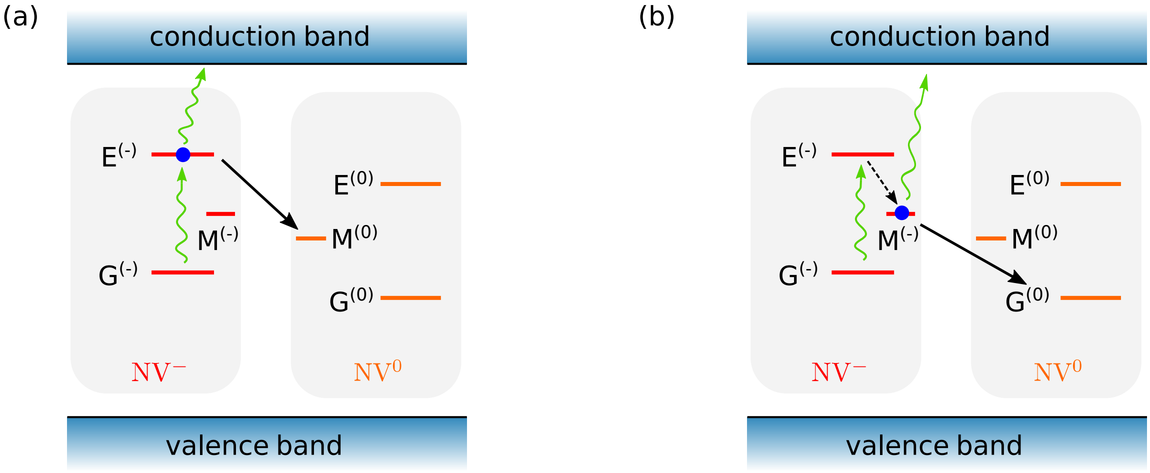

Figure 1.8: Schematic illustration of the photo-induced ionization of the NV center. The curvy green arrows symbolize the laser-induced electronic transitions, while the black arrows represent the resulting transitions between the levels of the NV defect. **(a)** Two-photon ionization via the NV$^-$ excited level. **(b)** Two-photo ionization via the NV$^-$ metastable level.

Theory therefore predicts that the ionization of the NV center induced by the 532 nm laser should mostly populate the metastable level of NV^0. We will now check experimentally for the presence of this NV^0 metastable level and investigate new phenomena of the charge state dynamics under green laser illumination.

1.2 Evidence of the NV^0 metastable level

The NV^0 metastable level involved in the main ionization process likely has an impact on the photodynamics of the defect. Considering that this metastable level is a long-lived trapping state, it should lead to a decrease of the photoluminescence signal, similarly to the NV$^-$ metastable level. To investigate such effect, we develop an original pulsed sequence based on a dual excitation scheme.

1.2.1 Population trapping into the NV^0 metastable level

We investigate native NV defects in an ultra-pure synthetic type IIa diamond crystal prepared using microwave assisted chemical vapor deposition (CVD) growth on a (1 0 0)-oriented substrate (Element Six). Individual NV defects are optically addressed at room temperature using a standard confocal optical microscope. A laser operating at 532 nm is focused onto the sample through a high-numerical aperture oil-immersion microscope objective (Olympus, 60x, NA=1.35). The NV photoluminescence is collected by the same objective, focused on a 50 µm diameter pinhole and finally detected by a photon-counting detection system. The modulation of the laser is implemented by two independent free space acousto-optic modulators (AOM) (AA Opto Electronic). The two independent AOM are used to perform the dual excitation scheme. Further details about the experimental setup is given in [61].

Time-resolved photoluminescence in dual excitation scheme

To probe the pumping into a trapping NV^0 metastable level, we apply a sequence of two laser pulses, as illustrated in figure 1.9(a). The first laser pulse of 10 µs initializes the NV defect into an equilibrium, eventually trapping some populations into M$^{(0)}$. The NV is then left in the dark during 2 µs so that the populations in M$^{(-)}$ have fully decayed to the ground level ($\tau_{M^{(-)}} \approx 200\,\text{ns}$). A second laser pulse finally reads the NV$^-$ ground-level populations by recording the spin-dependent signal produced at the beginning of the pulse. The key idea of the dual excitation scheme is to vary the laser power of the initialization laser pulse - in order to tune the charge state equilibrium - while using a constant readout laser power.

The time-resolved photoluminescence signals recorded for three different initialization powers are plotted in figure 1.9(b). The photoluminescence signal recorded during the initialization pulse increases with the optical power, through a standard saturation behavior. The readout signal is mostly similar as all the curves are acquired at the same readout power. Interestingly, some slight variations are, however, observed at the start of the readout pulse. To examine these differences in more detail, a zoom into the data is shown in figure 1.9(c). It appears that for low (resp. high) initialization power, the readout photoluminescence signal is stronger (resp. weaker). By increasing the initialization laser power, the readout signal decreases, and even goes below the steady state photoluminescence level obtained at the end of the pulse.

Two phenomena could explain the dependency of the readout signal on the initialization power:

1. A power-dependent spin polarization efficiency resulting in a variation of the photoluminescence signal.
2. The presence of an additional metastable level, which population increases with the optical power.

To discriminate between these two hypotheses, a second experiment is performed where an additional microwave π pulse is applied after the initialization laser pulse. In this case, the populations are prepared in the $m_s = \pm 1$ spin sublevels. The readout signal for this second

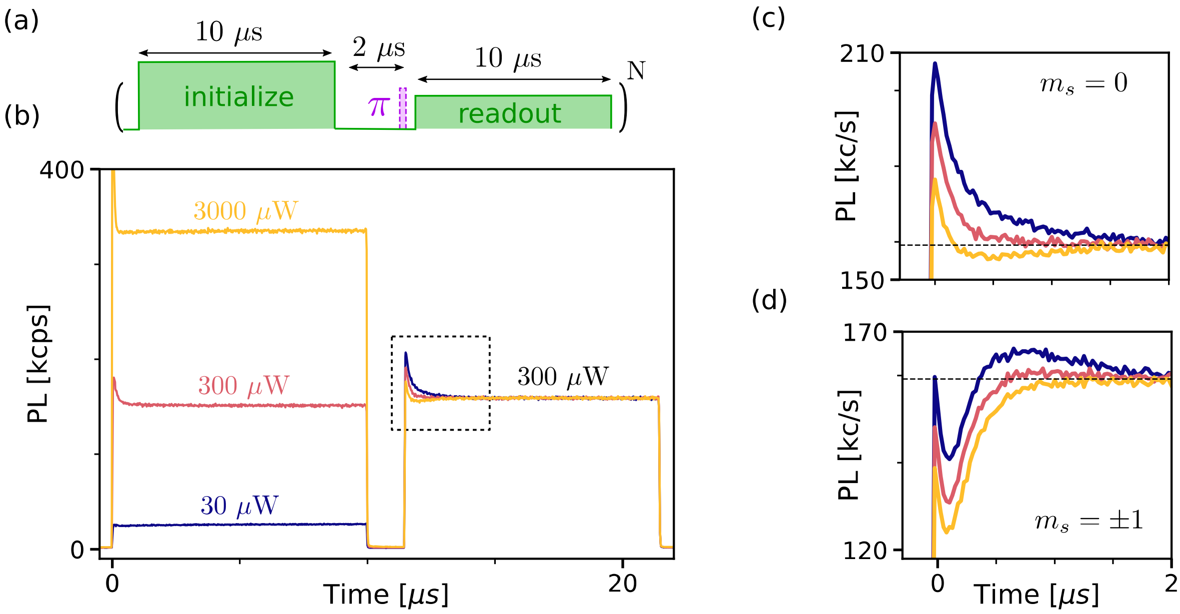

Figure 1.9: Time-resolved photoluminescence in the dual excitation scheme. **(a)** Schematics of the dual excitation scheme. A first laser pulse is used for initialization while a second laser pulse is used for readout. A similar sequence is acquired with and without applying a microwave π pulse to probe the NV center when the spin populations are prepared in the $m_s = \pm 1$ or $m_s = 0$ sublevels, respectively. **(b)** Time-resolved photoluminescence signal recorded for three different initialization powers. The readout power is always set to 300 µW, corresponding to the saturation power of the NV center. **(c, d)** Zoom on the photoluminescence signal at the beginning of the readout pulse for spin populations prepared in $m_s = 0$ (c) or $m_s = \pm 1$ (d).

experiment is plotted in figure 1.9(d). Considering that the spin polarization is simply reduced at high initialization power, then the experiment performed without applying a π pulse would show a lower readout signal at high initialization power, as observed experimentally. By applying a π pulse, the reduced spin polarization would then lead to a decrease of the transferred populations into $m_s = \pm 1$, corresponding to a higher luminescence signal. To put it differently, applying a π pulse should reverse the order of the curves in the readout signal. As shown in figure 1.9(d), our experiment indicates the opposite behavior. For high initialization power, the readout signal remains lower after applying the π pulse. This observation therefore rules out the hypothesis of a power-dependent spin polarization efficiency.

On the other hand, the presence of a metastable level is fully compatible with our observations: if the lower readout signal is linked to some populations trapped in a metastable level, the π pulse, which only affects the ground-level spin populations, would not induce any change in the observed behavior. A lower readout luminescence would then be expected for a high initialization power for both measurements, as observed experimentally.

The ionization from the NV$^-$ excited level has been predicted to populate a metastable level: the metastable level of NV^0. We therefore attribute the missing photoluminescence to the presence of populations trapped in this level. In the following sections, we perform additional experiments supporting this hypothesis.

Evolution of the trapped populations with the optical power

To analyze quantitatively the fraction of the missing photons in the readout signal, the photoluminescence is integrated over the first 300 ns of the readout pulse (figure 1.10(a, b)). In order to compare the readout signals from independent acquisitions, which can suffer from small laser fluctuations, the integrated signal is normalized by the average photoluminescence recorded during a reference window at the end of the readout pulse. Figure 1.10(c) plots the resulting integrated photoluminescence signal versus the initialization power. The data are shown both for the NV defect prepared in $m_s = 0$ and $m_s = \pm 1$. As observed qualitatively before, the readout photoluminescence decreases with the initialization power for both prepared spin sublevels.

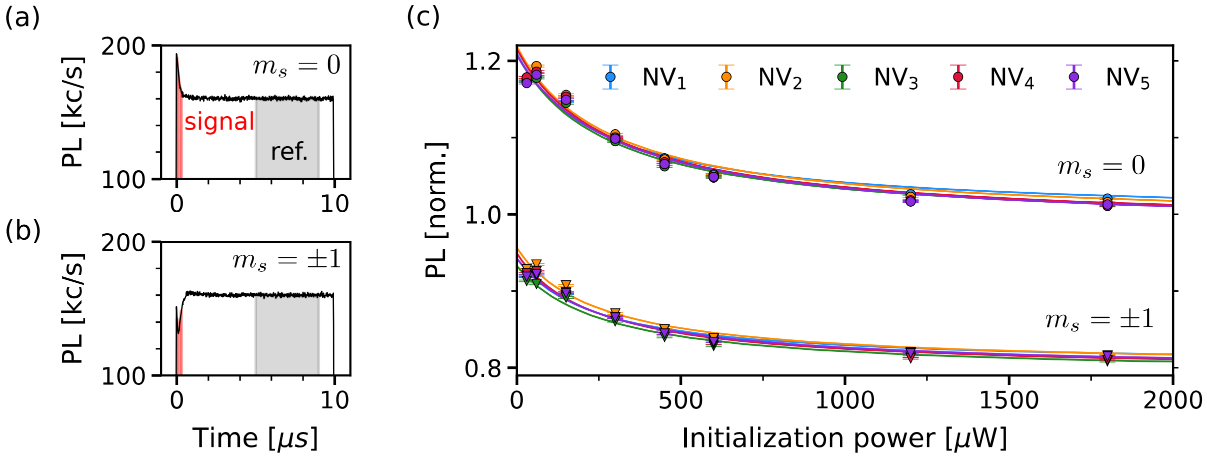

Figure 1.10: Evolution of the readout photoluminescence signal with the excitation laser power. **(a, b)** Time-resolved photoluminescence reproduced from figure 1.9, without and with a microwave π pulse, respectively. The signal is integrated over a window of 300 ns and normalized by the average signal of a reference window (ref.) taken at the end of the readout pulse. **(c)** Integrated photoluminescence signal versus the initialization power. Measurements are repeated on 5 different NV centers. Experimental data are fitted with equation 1.1, giving a saturation power $P_0 = 280(30)\,\mu$W, a value corresponding to the saturation power of the NV center optical transition in our setup.

Interestingly, the quantitative analysis reveals that the loss of photons saturates at high initialization power. Considering that this lack of photoluminescence signal relates to the populations trapped in a metastable level, this observation indicates that these populations increase with the laser power but saturate for high initialization power. Remarkably, the change in photoluminescence is around 20 %, indicating that a large number of populations are trapped in this level. To extract the saturation power of the trapping transition, the experimental data are fitted by a standard saturation model described by the equation:

$$I(P) = A_0 \times \frac{1}{1 + P_0/P} + B_0, \tag{1.1}$$

where I is the photoluminescence signal, P is the laser power, A_0 is the contrast amplitude, B_0 is an offset and P_0 is the saturation power. A saturation power of $P_0 = 280(30)\,\mu$W is extracted, which corresponds to the saturation power of the NV center optical transition in our experimental setup. The fact that the NV center optical transition and the metastable level transition saturate at the same laser power suggests a link between the trapping transition and the excited-level populations. This observation supports an ionization process from the NV$^-$ excited level which leads to the NV^0 metastable level, as sketched in figure 1.8(a).

The signals recorded for the two spin populations ($m_s = 0$ and $m_s = \pm 1$) are shifted vertically because of the spin-dependent photoluminescence properties, but display similar dynamics. This similarity indicates that the trapped populations are not affected by the microwave π pulse. We can therefore conclude that the trapped populations and spin dynamics are independent to first order.

Importantly, the same measurement repeated on 5 single NV centers unveils an identical behavior. This reproducibility confirms that this phenomenon is intrinsic to the NV center dynamics, and further supports the hypothesis of a trapping mechanism into the NV^0 metastable level.

1.2.2 Lifetime of the metastable levels

An important property of the NV^0 metastable level is its intrinsic lifetime, which corresponds to the decay towards the NV^0 ground level. Before measuring this lifetime, it is first helpful to consider how the NV$^-$ metastable level lifetime is commonly measured.

Lifetime of the NV$^-$ metastable level

The NV$^-$ metastable level lifetime can be measured by using the experimental sequence shown in figure 1.11(a) [53]. A first laser pulse initializes the system into a steady state, in which some populations are trapped into the NV$^-$ metastable level. Then, the NV defect is left in the dark for a time τ, during which these populations decay to the ground level. After this time τ, a second laser pulse probes the NV center spin populations. The time-resolved photoluminescence signal of the readout pulse for several delays τ is plotted in figure 1.11(b). To visualize the signal contrast, the photoluminescence signal is normalized by its steady state level recorded at the end of the pulse. The measurement reveals that the overshoot is small for short delays, and then gets larger on a timescale of $\approx 1\,\mu\text{s}$. This evolution corresponds to the decay in the dark of the populations trapped in the NV$^-$ metastable level. By measuring the increase of the overshoot signal with the time delay τ, it is possible to extract the lifetime of the NV$^-$ metastable level.

To get a precise value of the lifetime, a standard method is to integrate the readout luminescence counts over a given detection window. Here a window of 100 ns is chosen, corresponding to the beginning of the overshoot (shaded areas in figure 1.11(b)). The average value of the integrated signal is plotted versus the pulse delay τ in figure 1.11(c). The photoluminescence signal displays an increase with an exponential behavior, which corresponds to the NV$^-$ metastable level populations decay. By fitting the data points with an exponential model, a characteristic lifetime $\tau_{M^{(-)}} = 206(2)$ ns is extracted, corresponding to the NV$^-$ metastable level lifetime.

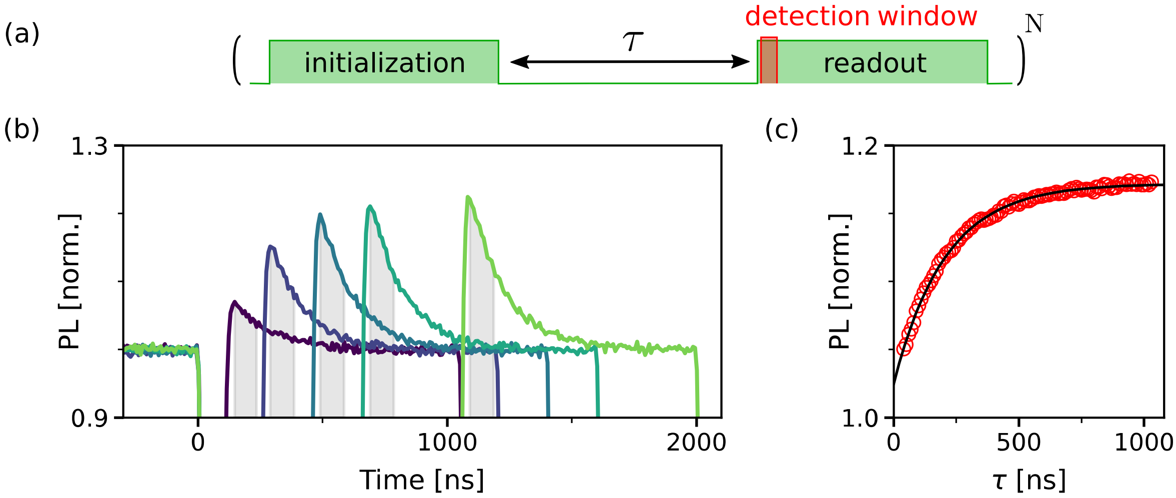

Figure 1.11: Measurement of the NV$^-$ metastable state lifetime. **(a)** Laser sequence used for the measurement of the NV$^-$. **(b)** Time-resolved photoluminescence for several pulse delays τ. The data shown correspond to delays τ of 50, 200, 400, 600 and 1000 ns. The photoluminescence is normalized by its steady state level. The gray areas at the beginnings of the readouts pulses show the integration window of 100 ns. **(c)** Integrated photoluminescence signal as a function of the pulse delay τ. The data are fitted with an exponential model to extract the NV$^-$ metastable lifetime of 206(2) ns.

This value matches the typical values found in the literature for single NV centers at room temperature [53].

As the overshoot is a general signature of populations trapped in a metastable level, a similar method can be exploited to investigate the decay of the NV^0 metastable level populations.

Lifetime of the NV^0 metastable level

To measure the lifetime of the NV^0 metastable level, a method identical to the measurement of the NV$^-$ metastable level lifetime is used. As illustrated in figure 1.12(a), a first laser pulse is applied to initialize the system and induce populations in the NV^0 metastable level. The NV center is then left in the dark for a time τ during which the trapped populations can decay. Finally, a second laser pulse probes the NV$^-$ ground-level populations. The minimum pulse delay is chosen to be 2 µs such that the NV$^-$ metastable level ($\tau_{M(-)} \approx 200$ ns) is systematically empty and can therefore be ignored. The time-resolved photoluminescence signal during the readout pulse is displayed in figure 1.12(b). The signal is again normalized by its steady state level recorded at the end of the pulse. A close examination shows a slight increase in the overshoot for longer pulse delays τ.

To quantify the photoluminescence variation, the average signal over the first 300 ns is integrated and plotted in figure 1.12(c). The integrated signal displays an increase over the [2 µs, 50 µs] window. This increase is attributed to the decay of the populations trapped in the metastable level of NV^0. To check for experimental artifact induced by the laser excitation, the experimental sequence was repeated by recording the attenuated laser reflection on the diamond

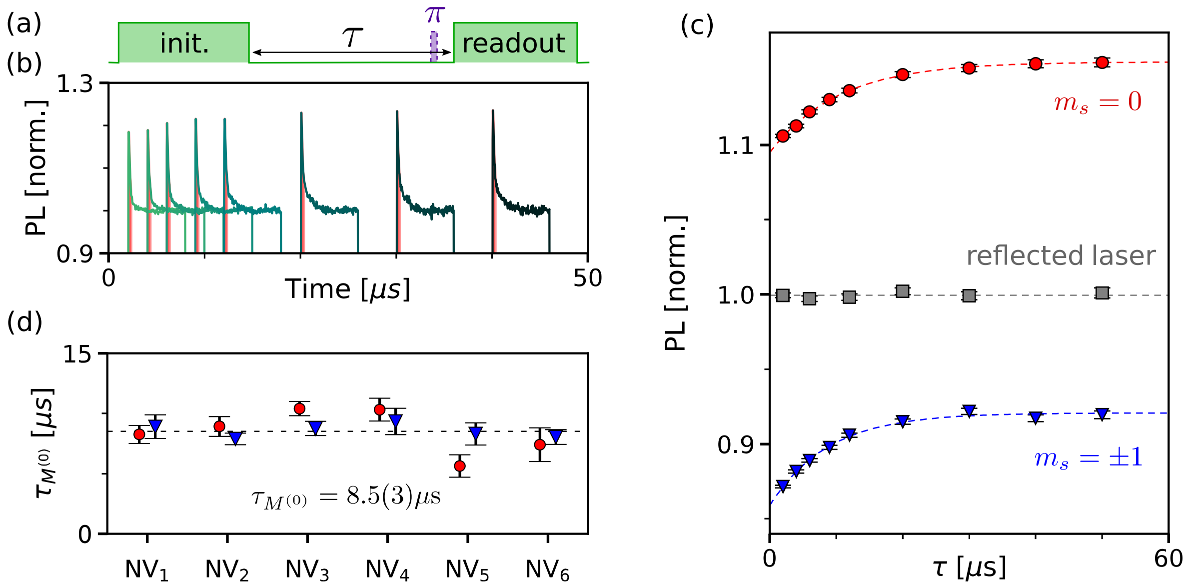

Figure 1.12: Measurement of the NV^0 metastable level lifetime. **(a)** Experimental sequence used to measure the NV^0 metastable lifetime. **(b)** Time-resolved photoluminescence of several readout pulses. The signal is normalized by its steady state level. The laser power is 300 µW, corresponding to the saturation power of the NV center optical transition. The average photoluminescence is integrated over the first 300 ns of the readout pulse (shaded in red). **(c)** Integrated photoluminescence signal as a function of the delay τ. The same sequence has been acquired on the reflection of the laser to check for experimental artifacts. Data are fitted with an exponential function to extract a lifetime $\tau_{M^{(0)}}$. **(d)** Lifetimes $\tau_{M^{(0)}}$ extracted for 6 different NV centers for both prepared spin populations. A dashed line shows the average lifetime of 8.5(3) µs.

surface. Densities were used to avoid damaging and saturating the single photon detector. The resulting signal is shown in figure 1.12(c). It is perfectly constant with the delay τ, confirming that the photoluminescence evolution originates from the NV center. To look for any effect related to the prepared spin populations, a similar sequence with a microwave π pulse applied before the readout laser pulse was also recorded (figure 1.12(c)). The photoluminescence signal for this second experiment is overall lower because of the spin-dependent photoluminescence, but exhibits a similar evolution with only an offset, indicating that the decay is not spin-dependent.

To extract the lifetime of the metastable level, the data are fitted with an exponential function. The resulting lifetimes $\tau_{M^{(0)}}$ for 6 single NV centers and for both prepared spin populations are plotted in figure 1.12(d). Remarkably, these lifetimes are similar for all NV centers and for both spin populations. An average value of $\tau_{M^{(0)}} = 8.5(3)$ µs is computed from all the data points. The reproducibility over 6 NV centers corroborates (i) that the populations decay process is intrinsic to the NV center dynamics and (ii) that the assignment to the NV^0 metastable level is plausible. It is also the first measurement of the metastable level lifetime of NV^0.

Influence of the $M^{(0)}$ level on the NV center time-resolved photoluminescence signal

The measurements of the lifetimes of $M^{(-)}$ and $M^{(0)}$ are very similar: they both rely on the same laser sequence and data analysis but on different timescales. To get a full picture of the NV center dynamics, we repeat the experiment on an expanded time range from 10 ns to 10 ms, spanning 6 orders of magnitude. The resulting signal, which is the integrated readout pulse photoluminescence over the initial 300 ns, is plotted versus the delay τ in figure 1.13. The photoluminescence evolution can be divided in two successive increases (I) and (II), and a decrease (III) for the longest pulse delays.

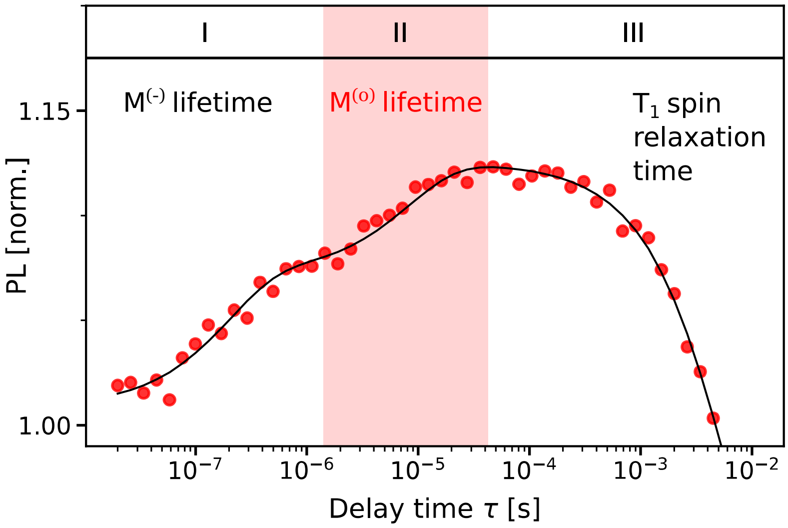

Figure 1.13: Integrated photoluminescence signal of the readout pulse versus delay time τ. The signal displays two successive increases linked to the decay of the $M^{(-)}$ level (I), and of the $M^{(0)}$ level (II). The photoluminescence decreases at longer timescale (III) corresponds to the longitudinal spin relaxation time (T_1) of the NV defect. The solid line is a sum of three exponential functions with characteristic times of $\tau_{M^{(-)}} = 200$ ns, $\tau_{M^{(0)}} = 8.5$ µs and $T_1 = 6$ ms.

(I) The first increase corresponds to the decay of the populations trapped in the NV^- metastable level $M^{(-)}$ with a lifetime $\tau_{M^{(-)}} \approx 200$ ns, as measured previously in figure 1.11.

(II) The second increase is the newly evidenced increase of photoluminescence caused by the decay of the populations trapped in the NV^0 metastable level $M^{(0)}$, with a lifetime $\tau_{M^{(0)}} = 8.5(3)$ µs.

(III) The decrease at the long timescale reflects the decline of the NV^- spin polarization from the $m_s = 0$ bright sublevel toward a Boltzmann statistics, within the characteristic longitudinal spin relaxation time $T_1 \approx 6$ ms. At room temperature, this phenomenon is caused by the interaction between the defect and the phonons of the diamond lattice [62].

To support this interpretation, a solid line is plotted in figure 1.13, depicting the sum of three exponential functions with characteristic times fixed to the three values mentioned above. The solid line matches entirely the experimental points over 6 orders of magnitude.

In this subsection we evidenced a photoluminescence recovery in the dark, linked to the decay of populations trapped in the metastable level $M^{(0)}$. We will now investigate the process of recombination from this trapping level by laser excitation.

1.2.3 Recombination dynamics

Ionization of the NV$^-$ center is the process in which it loses an electron and is converted to the neutral charge state NV^0. We have shown that this process can engender populations in a metastable level $M^{(0)}$, a long-lived trapping level. The recovery to the negative charge state NV$^-$ is called recombination. This recombination under the 532 nm green laser excitation can happen from the NV^0 excited level [48], but recombination could also occur from $M^{(0)}$. To test this hypothesis, we investigate the shift of the equilibrium between the charge states NV$^-$ and NV^0 under optical illumination, to look for a NV^0 → NV$^-$ recovery.

To perform this study, we capitalize on several newly established facts.

1. Large laser power can prepare populations in the NV^0 metastable level, with a saturation behavior (§1.2.1).
2. The initial photoluminescence of a readout pulse can be used to probe the $M^{(0)}$ populations by measuring the missing photons.
3. The spin sublevels populations and the NV^0 metastable level populations are mostly independent.
4. The initialization power has little impact on the spin polarization efficiency.

To probe the recovery from $M^{(0)}$ under illumination, we develop the experimental sequence illustrated in figure 1.14(a). First, a high-power laser pulse (3000 µW) generates a large population trapped into $M^{(0)}$. The NV is then left in the dark for 2 µs, long enough to empty the NV$^-$ metastable level ($\tau_{M^{(-)}} \approx 200\,\text{ns}$) but short enough to consider that $M^{(0)}$ ($\tau_{M^{(0)}} = 8.5(3)\,\mu\text{s}$) is still occupied. We can thus neglect the influence of $M^{(-)}$ in the rest of the analysis. A readout pulse of intermediate power (300 µW) is then applied to the NV center with a dual purpose. As the initialization and readout powers are different, a shift in the equilibrium of the $M^{(0)}$ trapped populations will occur. Since the missing photoluminescence mirrors the $M^{(0)}$ population, the readout pulse probes the evolution of its population. This measurement is compared to a second sequence for which a low initialization power (30 µW) is used, without changing the readout power. Figure 1.14(b) displays the time-resolved photoluminescence signals S_{high} and S_{low} of the two readout pulses respectively. The photoluminescence is normalized by the common steady-state level of photoluminescence at the end of the readout pulses. The difference between the two pulses is solely due to different populations in the NV^0 metastable level populations, as the signal evolution linked to the spin dynamics is similar for the two curves.

By computing the difference $S_{\text{high}} - S_{\text{low}}$, a photoluminescence signal directly related to the evolution of the NV^0 metastable population is extracted (figure 1.14(c)). The resulting signal is negative and goes to zero with an exponential evolution. The negative sign is expected, as the high laser power generates more trapped populations, which reduces the photoluminescence

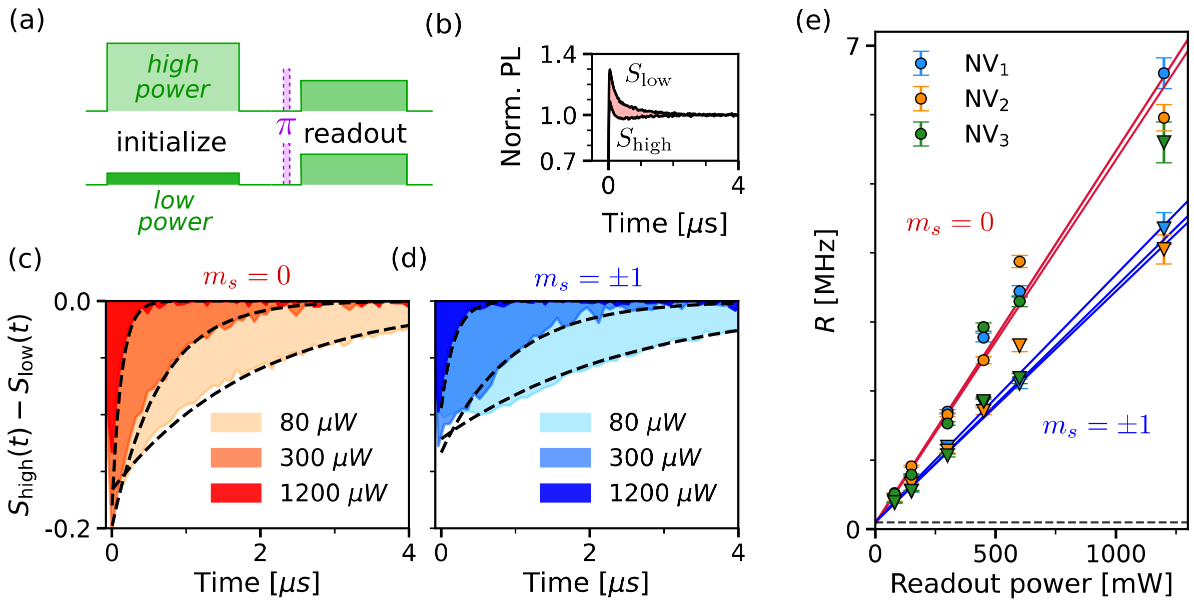

Figure 1.14: Recombination dynamics under laser illumination. **(a)** Schematics of the laser sequence used to probe the recombination dynamics under illumination. **(b)** Time-resolved photoluminescence signals for a readout power of 300 µW when no π pulse is applied. The photoluminescence is normalized by the steady state level integrated at the end of the pulse. **(c, d)** Subtraction of the two readout pulses for three different readout powers. Each curve is fitted with an exponential model (dashed lines) to extract a rate R. **(e)** Rate R versus the readout laser power for three different NV centers. Rates are fitted with a linear model for each NV and each prepared spin populations.

signal in S_{high} compared to S_{low}. The evolution to zero indicates that this difference in population decreases during the readout pulse. Such decrease of the NV^0 populations indicates that there is a recombination process towards the NV$^-$ charge state, at a rate given by the exponential evolution. Remarkably, this recombination rate varies with the readout laser power, as revealed by repeating the experiment at two other readout powers. The observation of a laser-dependent recombination rate proves that there is an optically induced recombination process from the NV^0 metastable level to the negative charge state NV$^-$. Such a recombination mechanism has not been investigated by any theoretical work to date, but could simply correspond to a direct recombination to the ground level of NV$^-$.

To investigate for any spin-dependent effect, the experiment is repeated with a microwave π pulse and the results are plotted in figure 1.14(d). A first observation is that the subtracted photoluminescence after the π pulse is close to the one without it. This similarity confirms that, in first approximation, the spin and the NV^0 metastable level dynamics are independent. Still, a close inspection of the data reveals slightly lower signals and slower recovery rates, suggesting that the two processes could be not fully independent, as we will investigate in the next section.

M$^{(0)}$ recombination rate under illumination

To analyze quantitatively the evolution of the recombination dynamics with the readout laser power, the experimental data shown in figures 1.14(c) and (d) are fitted with an exponential model $S_{\text{high}} - S_{\text{low}} = \alpha_r \times e^{-Rt}$ where R is the decay rate of the signal, and α_r is a free constant. The evolution of the rate R with the laser power is plotted in figure 1.14(e). The experiment is repeated on 3 single NV centers for which all the points are displayed. The rate R displays a linear increase with the laser power, but the slope is slightly lower when a π pulse has been used to prepare the NV$^-$ spin populations in $m_s = \pm 1$.

As the signal $S_{\text{high}} - S_{\text{low}}$ reflects the populations of the NV^0 metastable level, the linear evolution of the rate R indicates that the recombination process to NV$^-$ is linear with the laser power. To extract the slopes, linear fits $R(P) = a_{m_s=i} \times P + b_{m_s=i}$ are performed for each NV center. The average for the 3 defects gives values of $a_{m_s=0} = 5.3(3)\,\text{MHz}\,\text{mW}^{-1}$ and $a_{m_s=\pm 1} = 3.4(3)\,\text{MHz}\,\text{mW}^{-1}$, corresponding to a ratio $\approx 3/2$. Still, caution should be taken before interpreting these rates. The charge state equilibrium that is probed during this experiment is determined both by the ionization and the recombination processes. The measured rate R is therefore not only linked to the recombination. The ionization process from the NV$^-$ excited level depends on the time spent in this level, which itself is spin-dependent owing to the spin-dependent decay rate through the NV$^-$ metastable level. The NV$^-$ excited level lifetime was measured to be around 13.7 ns for $m_s = 0$ while only 7.3 ns for $m_s = \pm 1$ [53], which corresponds to a ratio of ≈ 1.88. This phenomenon is at the origin of the previously mentioned *spin-to-charge* protocol used to readout the NV$^-$ spin state via the spin-dependent ionization [58]. Here the ratio of $\approx 3/2$ could well be explained by this spin-dependent ionization process alone. Furthermore there is no reason to think that the populations in M$^{(0)}$ are affected by the microwave π pulse which interacts only with the ground level of NV$^-$. A direct interpretation of these rates is therefore not possible, but the order of magnitude of $\approx 4\,\text{MHz}\,\text{mW}^{-1}$ corresponds likely to the recombination process.

A remarkable detail is that the rate R extrapolated at zero power is not zero, for all NV centers. An average value of $b_{m_s=i} = 90(30)$ kHz is computed from all the curves. This non-zero rate corresponds to a recombination from the NV^0 metastable level in the dark. Furthermore, this rate matches the value of 118(4) kHz, corresponding to the lifetime of $\tau_{M^{(0)}} = 8.5(3)\,\mu\text{s}$ measured previously. This observation confirms that the recombination process is related to the NV^0 metastable level and corroborates the lifetime measurement performed in the dark.

It should be noted that a close inspection of the experimental points in figure 1.14(e) reveals some differences with a linear trend, given the error bars. These variations can be explained by the complex dynamics of the NV center populations during the ionization and recombination which do not necessarily produce a simple mono-exponential evolution of the photoluminescence signal, as approximated in figures 1.14(c) and (d). The exploration of such details requires a complete picture of the NV center levels and populations evolution which goes beyond the traditional 5-level model used to describe its dynamics. In the third section, we lay the groundwork for such modeling of the NV center dynamics.

1.3 Modeling the dynamics of photochromism

To build a new model of NV center dynamics under green laser illumination, we summarize what we have evidenced in §1.2 into figure 1.15. The 5-level model corresponding to the NV^- levels $\{G^{(-)}, E^{(-)}, M^{(-)}\}$ is depicted, and is at the origin of the photoluminescence signal we collect. The NV^0 levels $\{G^{(0)}, E^{(0)}, M^{(0)}\}$ are also pictured as they matter in the full NV center dynamics. The three newly evidenced transitions are drawn:

1. The ionization process from $E^{(-)}$ to $M^{(0)}$, which was predicted by theory [51] and that was verified experimentally (§1.2.1).
2. The intrinsic decay from $M^{(0)}$ to $G^{(0)}$ with a lifetime $\tau_{M^{(0)}} = 8.5(3)\,\mu s$ (§1.2.2).
3. The recombination process from $M^{(0)}$ to $G^{(-)}$ under illumination that was revealed by probing the equilibrium shift under illumination (§1.2.3).

Both the ionization $M^{(-)} \rightarrow G^{(0)}$ and the recombination $E^{(0)} \rightarrow NV^-$ are also indicated as they have been evidenced experimentally [48, 63, 64] despite having not been directly investigated in our experiments. It should be noted that to explain the increase of the photoluminescence signal during the measurement of the decay $M^{(0)} \rightarrow G^{(0)}$, a fast recombination process via the NV^0 excited level ($G^{(0)} \rightarrow E^{(0)} \rightarrow NV^-$) has to be considered. The coupling $E^{(0)} \rightarrow M^{(0)}$ is not shown, as this transition is symmetry forbidden.

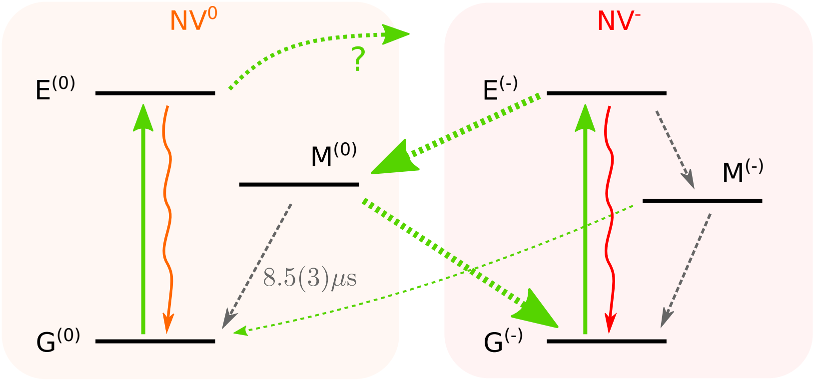

Figure 1.15: Schematics of the NV^- and NV^0 center energy levels, showing the defect ionization and recombination processes. Solid arrows correspond to direct radiative transitions, dashed lines to non-radiative decay of populations, and dotted lines to laser induced non-radiative changes of the charge state.

The resulting picture of the NV center dynamics offers a deeper understanding of the defect evolution, but it remains complex and with some open questions. To model the NV photoluminescence, we can try to build a simplified model which grasps most of the charge state conversion processes.

1.3.1 7-level model for the NV center

To build a simplified level of the NV center, we exploit the fact that the ground and excited levels of NV^0 have a minor role in the dynamics of the defect under green laser illumination.

First, at a laser power of several hundreds of µW, corresponding to the optical saturation power typically used in our experiments, the recombination process from $\mathrm{M}^{(0)}$ (a few MHz from figure 1.14) is much faster than its intrinsic lifetime ($1/\tau_{M^{(0)}} = 0.118(4)\,\mathrm{MHz}$). A consequence is that it is possible - on the first order - to neglect the intrinsic decay of the populations from $\mathrm{M}^{(0)}$ to $\mathrm{G}^{(0)}$. Secondly, since the ionization from $\mathrm{M}^{(-)}$ is small (14 times smaller compared to the ionization from $E^{(-)}$ at 532 nm [51]), this process can also be neglected. We can therefore eliminate the levels $\mathrm{G}^{(0)}$ and $\mathrm{E}^{(0)}$ to model the NV dynamics under optical illumination.

The resulting 7-level model of the NV center dynamics is illustrated in figure 1.16. For the negative charge state NV^-, the 5-level model introduced in figure 1.5 is recycled without modification. The radiative rate Γ, as well as the rates to and from the NV^- metastable level, are unchanged compared to the 5-level model (see values in table 1.1). To include $\mathrm{M}^{(0)}$ in the model, two levels $|5\rangle$ and $|6\rangle$ are added, corresponding to the spin sublevels $m_s = \pm 1/2$ and $m_s = \pm 3/2$ of the NV^0 metastable level, respectively. This division in two separate levels is required, as there are spin-dependent rates in the ionization mechanism. The ratios between these rates are given by the Clebsch-Gordan coefficients of the full electronic state after ionization, and were computed by theory [51]. To get the ratios for the recombination process from the NV^0 metastable level, a collaboration with the group of A. Alkauskas was established. This is precisely the group who predicted the presence of the ionization via the NV^0 metastable level and computed the Clebsch-Gordan for the ionization process [51]. The resulting ratios for ionization and recombination are displayed in figure 1.16.

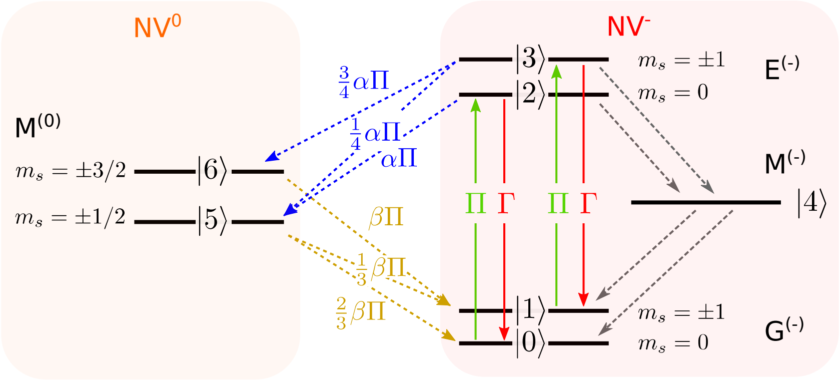

Figure 1.16: The 7-level model developed to describe the NV center photodynamics. When the NV^- is excited, it can decay radiatively (Γ), non radiatively via the NV^- metastable ($|4\rangle$) or be ionized to the NV^0 metastable spin sublevels ($|5\rangle$ and $|6\rangle$).

The inclusion into the model of the NV^0 metastable levels results in 6 additional transitions. Fortunately, these 6 new transitions only add 2 free parameters into the model, which are the magnitudes of the ionization α and of the recombination β. Here the ionization and recombination rates $\alpha\Pi$ and $\beta\Pi$ respectively are expressed relatively to Π, which denotes the NV^- optical excitation rate. This choice enables us to use the value of $\alpha = 0.15$ which was predicted by theory [51]. In the end, only β is unknown, but it will be shown in the next subsection that a value can be determined by matching the model to the time-resolved photoluminescence measurements.

To validate our 7-level model, we can test it by simulating the NV center time-resolved photoluminescence, and compare it to the prediction of the 5-level model.

1.3.2 Time-resolved photoluminescence

In most time-resolved photoluminescence sequences, the 5-level is enough to describe the signal evolution. To test the two models in a regime where the NV^0 metastable level is critical, we go back to the dual excitation scheme with which we evidenced the population trapping into $M^{(0)}$.

Simulations of the time-resolved photoluminescence signal with the 7-level model and with the 5-level model are computed by solving the linear differential equations numerically and are plotted next to the experimental data in figure 1.17. In both simulations the values for the NV^- rates are identical, and are taken from typical values in the literature (see table 1.1). The value of $\alpha = 0.15$ is fixed from the theory prediction. The remaining free parameters are then the recombination amplitude β, and the parameters Π and η, which depend on the experimental setup. As a global fitting procedure did not converge, these parameters were adjusted by hand, by matching the model simulation to the experimental photoluminescence. A best estimate of $\beta = 0.1$ was determined via this method (see table 1.2 for all parameters)

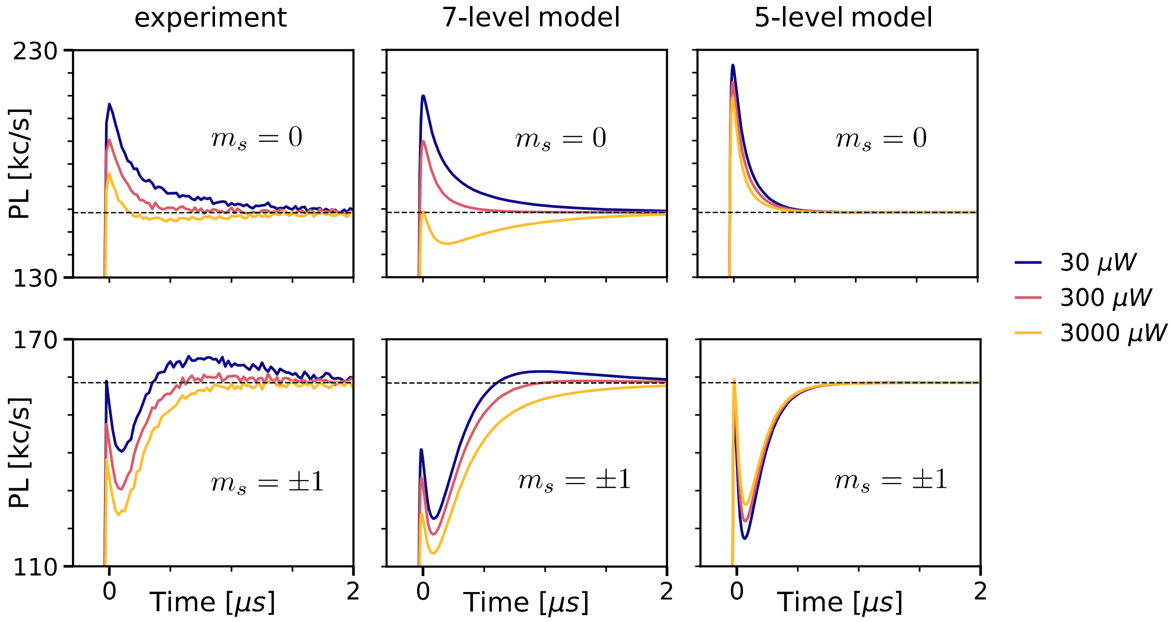

Figure 1.17: Modeling of the time-resolved photoluminescence in the dual excitation scheme. **(left)** Time-resolved photoluminescence of the dual excitation scheme zoomed on the readout pulse repeated from figure 1.9. **(middle, right)** Simulation of the photoluminescence signal given by the 7-level and the 5-level model respectively.

The simulation with the 7-level model shows a strong dependency of the readout signal with the initialization power. It exhibits a qualitative agreement with the experimental data: the

Π	η	α	β
40 MHz/mW	2.6×10^{-2}	0.15	0.10

Table 1.2: Numerical values of the parameters used in the 7-level model simulation. The excitation rate Π and the collection efficiency η have been updated to match the experimental data. The rates of the NV$^-$ transitions are similar to the ones in table 1.1.

readout photoluminescence decreases with initialization power for both prepared spin populations. Remarkably, the simulated signal is going below the steady-state value for $m_s = 0$ and above for $m_s = \pm 1$. The fair agreement between simulations and experiments validates the model and corroborates our interpretation of the NV center photochromism.

In comparison, the simulation with the 5-level displays a poor agreement with the experimental results. The model shows a small dependency of the readout signal on the initialization power, but predicts a reversed ordered of the curves in the case of the spin populations prepared in $m_s = \pm 1$. This reversed contrast is a consequence of the spin depolarization at large laser power, because of more trapped populations in M$^{(-)}$. Such effect indeed happens in the experiment but is a second-order process in terms of photoluminescence signal compared to the populations trapping in M$^{(0)}$.

It should be noted that the value of β determined by matching the model with the experimental data corresponds to the slope of the equilibrium rates under illumination in §1.2.3. The value of $\beta\Pi = 4\,\mathrm{MHz/mW}$ in the simulations matches the slopes measured via the recombination rate under illumination ($R \approx 4\,\mathrm{MHz/mW} \times P$), confirming the interpretation that this slope is the recombination rate.

Despite a qualitative agreement, no fitting of the free parameters could provide a closer match with the experimental data. A closer quantitative agreement should be reachable with a complete set of parameters determined self-consistently with the 7-level model, but such goal is beyond our general investigation of the NV center dynamics.

Here we have demonstrated that the 7-level model can be used to better explain the NV photoluminescence under a pulsed laser sequence. In the last subsection, we will look at the predictions of this model in a regime of continuous optical excitation.

1.3.3 Photophysics under continuous excitation

In this last section, we use the newly established 7-level model to answer open questions regarding the NV center properties under continuous optical illumination. First, the NV center was reported from NMR measurement to be in a dark state attributed to NV^0 for 30 % of the time. However, the underlying mechanism was unclear [46]. Secondly, the photoluminescence of the NV center was reported to decrease at very high laser power, but this behavior is not explained by the 5-level model [47]. Last, the lack of emission from the NV^0 charge state in the photoluminescence spectrum recorded under green laser illumination was in contradiction with the assumption of an average time spent in NV^0 of about 30 %. An analysis of the 7-level model and a detailed inspection of the NV photoluminescence spectrum will clarify this last point.

Level populations under continuous optical illumination

In §1.2.1, we have shown a population trapping around $\approx 20\,\%$ in the NV^0 metastable level. To explore this trapping further we consider the steady-state populations under illumination within the 7-level model. The computation of the populations is done by solving numerically the rate equations at each excitation power. The distribution of the populations between the 7 levels at each laser power are plotted in figure 1.18. The populations are displayed cumulatively so that their sum is 100 % for best visualization.

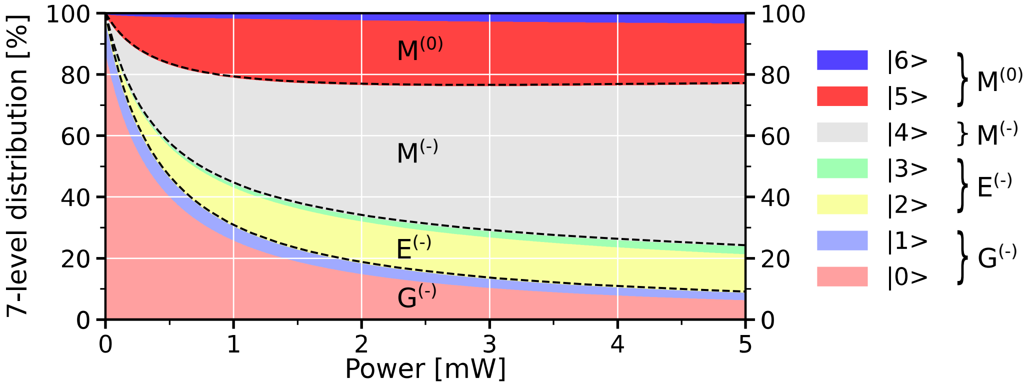

Figure 1.18: Steady-state populations of the 7-level model versus the optical power. The distribution is shown cumulatively so that the total is 100 %. The dashed lines indicate the separations between the levels.

The simulation shows that at low laser power, most of the populations are in the NV$^-$ ground level G$^{(-)}$ as the NV center is barely excited. When the laser power increases, the ground-level populations are transferred to the excited and metastable levels. At high excitation power, the photoluminescence is mostly limited by the NV$^-$ metastable level M$^{(-)}$ which can trap more than 50 % of the populations. The consideration of the full 7-level model reveals that a large percentage of the populations are also trapped in M$^{(0)}$. Remarkably, this population matches the observed population trapped in the NV^0 metastable level in §1.2.1 fairly well. The simulation predicts a trapping of $\approx 20\,\%$ with a saturation behavior. A fitting of the M$^{(0)}$ populations versus the laser power with equation 1.1 results in a saturation power $P_{0,\mathrm{M}^{(0)}} = 253\,\mu\mathrm{W}$, in agreement with $P_0 = 280(30)\,\mu\mathrm{W}$ measured in figure 1.10.

The population trapped in the NV^0 metastable level is close to the dark state population revealed in NMR measurements [46]. We can thus conclude that this dark state corresponds to the NV^0 metastable level, but not to the NV^0 ground or excited levels, as it was sometimes presumed. The analysis of the steady-state populations under illumination can also help us understand why the photoluminescence of the NV$^-$ center can decrease at very large excitation power.

Saturation curve of the NV center

The NV center saturation curve measures the evolution of the defect photoluminescence signal S with the laser excitation power P. Figure 1.19 shows a typical saturation curve recorded on a single NV center. A noteworthy observation is that the NV$^-$ center photoluminescence decreases after a certain point, as was reported early on in ref. [47]. This behavior does not match the prediction of the 5-level model which leads to a standard saturation behavior given by $S(P) = S_{\text{sat}} \times P/(P + P_{\text{sat}})$, where S_{sat} is the photoluminescence signal at saturation and P_{sat} is the saturation power. A *dark level* was invoked to explain this behavior, but no precise physical picture was ever given to explain this observation.

To evaluate the impact of the NV^0 metastable level in this phenomenon, the photoluminescence signal S versus the laser power P was computed within the 7-level model. This simulation simply corresponds to $S = P_{E(-)} \times \eta\Gamma$ where $P_{E(-)}$ is the total excited-levels population. The result of the simulation, plotted in figure 1.19, exhibits a good agreement with the experimental data. It can thus be concluded that the decreased photoluminescence observed at high laser power is directly caused by the population trapping in the NV^0 metastable level.

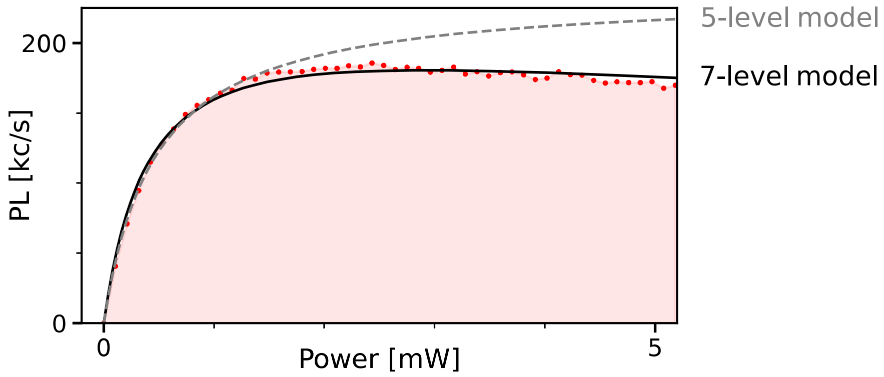

Figure 1.19: Evolution of the photoluminescence signal of a single NV center with the laser excitation power. The simulations of the photoluminescence signal given by the 7-level and 5-level models are shown by solid and dashed lines, respectively.

As discussed previously, the $\approx 30\,\%$ of the populations in NV^0 measured by NMR in 2011 [46] are linked to the NV^0 metastable level and not the ground or excited levels. This observation incidentally explains why no large NV^0 photoluminescence is observed in the photoluminescence spectrum. To check this conclusion, one last experiment is performed to look closer at the NV center photoluminescence spectrum.

Dim emission from NV^0

A puzzling observation to date was that *no photoluminescence* from the neutral charge state NV^0 seemed to be observed under the standard conditions of observation of single NV centers under green laser excitation. A deep analysis of the NV center literature in these typical experimental does not reveal any photoluminescence spectrum with a contribution from the neutral charge sate. To investigate this issue, we recorded well-accumulated photoluminescence spectra from a single NV center.

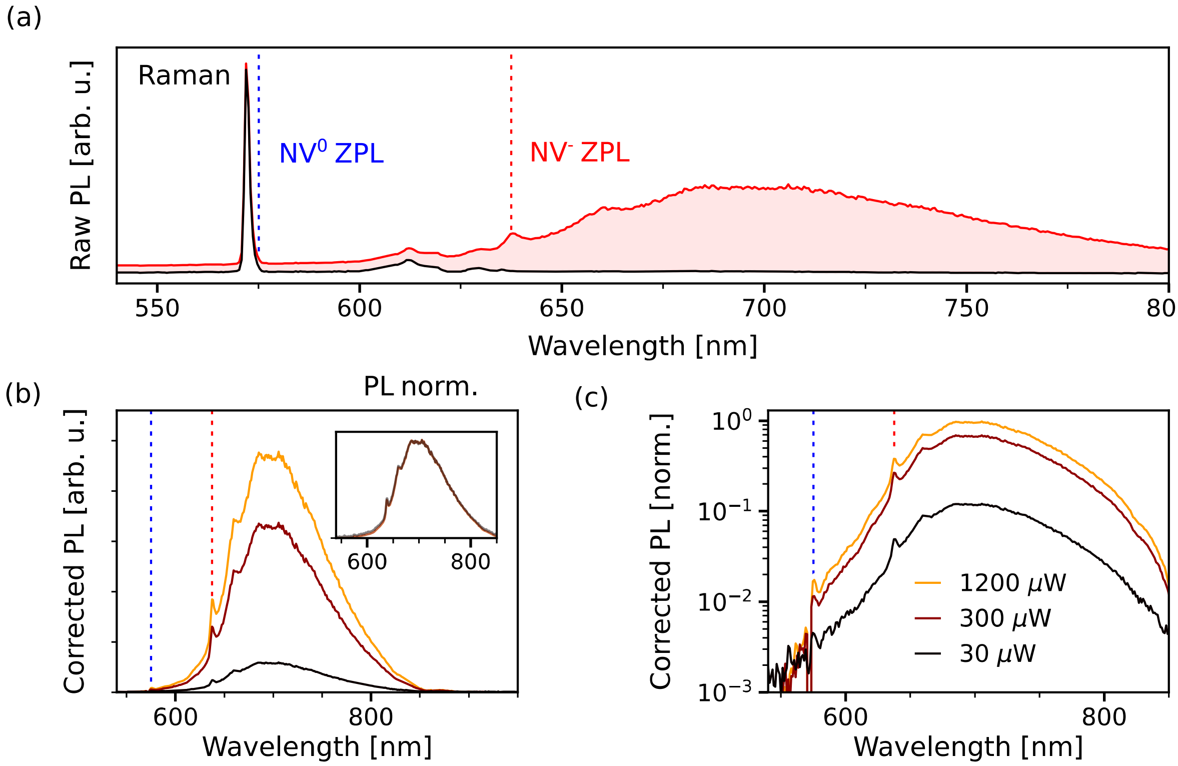

Figure 1.20: Photoluminescence spectra of a single NV center under green excitation at room temperature. **(a)** Raw photoluminescence spectra taken on a single NV center and on the background. The background (black curve) shows only Raman photoluminescence while the data on the defect shows both the Raman and the NV center emission. The corrected spectra is computed from the difference between the two. The spectra are shifted vertically for visualization. **(b)** Background-corrected photoluminescence spectra of a NV center recorded at laser powers of 30 µW, 300 µW and 1200 µW. The dashed lines indicate the NV^- and NV^0 ZPL wavelength. (inset) The spectra normalized in intensity. **(c)** Same spectra as in (b) plotted in semi-logarithmic scale.

An obstacle to this measurement under green laser excitation at 532 nm is the Raman emission of the diamond itself. In particular, diamond has a strong Raman peak at 1332 cm^{-1} [65] which induces an emission line at 572 nm. This Raman peak is very close to the NV^0 ZPL at 575 nm and can therefore hide its presence. To get rid of this parasite signal, spectra were acquired both at the location of the NV center and on a background. This background was taken by moving the laser focus away from the defect laterally by a few micrometers. The acquisition was performed by accumulating the data for a full night while switching between the NV center and the background every 10 s to average-out any fluctuation in laser power or of other external parameters. The raw spectra of the NV center and of the background are plotted in figure 1.20(a). The spectra are shifted vertically for visualization, and vertical dashed lines indicate the position of the zero-phonon lines for NV^0 and NV^-. Both spectra exhibit a strong line at 572 nm as well as a weaker emission around 620 nm, corresponding to the diamond's Raman emission main peak and second-order peaks [65]. The spectrum of the NV center shows an additional emission corresponding to the NV center alone.

The corrected photoluminescence spectrum is then computed by taking the subtraction of both well accumulated curves. The results obtained for 3 different laser powers are shown in figure 1.20(b). The three curves exhibit an increase in photoluminescence signal with the laser power reflecting the general increase in photoluminescence of the defect. When normalized, the curves are identical, as shown when superposed in the inset of figure 1.20(b). The observed emission corresponds to the photoluminescence spectrum of the negatively charged state NV^- with a zero-phonon line at 637 nm and a phonon-sideband. For better visualization, the same data are plotted in logarithmic scale in figure 1.20(c). Remarkably, a small emission peak is visible at 575 nm for each laser power, corresponding exactly to the NV^0 ZPL wavelength. This observation indicates that there is a dim emission from the NV^0 charge state under green illumination. This emission confirms that despite a recombination from the NV^0 metastable level under illumination, a small part of the populations does decay to the ground level of NV^0. These populations lead to a dim emission from the neutral charge state under green illumination, which remains hidden most of the time because of its small contribution to the total photoluminescence owing to the long lifetime of the NV^0 metastable level. Surprisingly, this is in fact the first direct observation of the photochromism of a standard single NV center under green illumination.

1.4 Conclusion

In this chapter we have investigated the NV center charge state dynamics under green laser excitation. Via an original sequence of pulsed laser excitation, we demonstrated the involvement of a long-lived metastable level, which is attributed to the metastable level of the NV^0 charge state. We measured the NV^0 metastable level intrinsic lifetime at room temperature to be 8.5(3) µs, and we showed that this level could also give rise to a direct recombination under laser illumination. By considering the newly established knowledge of the defect dynamics, we built a simplified 7-level model of the NV dynamics and demonstrated a qualitative agreement with the measured time-resolved photoluminescence. Finally, we used the 7-level model to give answers to several open questions regarding the NV center photoluminescence under continuous optical illumination.

The discovery of a hidden dynamics, which has been surprisingly undetected up to now, reveals that there are still many unexplored aspects of the famous NV center defect. Ionization from the NV^- metastable state has been reported [64,66] but remains to be fully characterized. The same goes for the recombination process from the excited level of NV^0 [48]. A complete description of both processes is required to elaborate a *9-level model* of the defect which could include the dim emission from NV^0. The room temperature behavior of the NV^0 metastable level has been studied in this manuscript, but the NV center properties are known to vary with temperature [53,67], therefore requiring further investigation for the cryogenic regime. Last, the uncovered NV^0 metastable level spin has been previously detected by EPR and its zero field splitting measured to be 1685(5) MHz [60]. As the level is involved in the NV dynamics, an optical detection via ODMR could be performed under green illumination but remains to be demonstrated.

The new understanding of the NV center charge state switching might enable improvements of the experimental protocols used in the NV center based applications. At low temperature, ionization is a limiting phenomenon under resonant excitation. The recombination process we uncovered, if similar at the cryogenic regime, could be used to improve the recovery to the negative charge state.

The lessons learned on the NV center also feed our understanding of other spin defects in diamond as well as in other semiconductors. The NV center of diamond is a remarkable platform for spin manipulation which was used at low temperature to demonstrate entanglement between distant spins. For quantum communication as for quantum computing, the diamond material itself is, however, an obstacle to scaling. Traditional materials used in computer chips could offer an easier path to large-scale technologies, but the defects in these materials have remained mostly unexplored. Silicon would be an ideal platform to develop large applications with millions of spin defects, but their study is complex for this material. Due to its small bandgap, defects in silicon are luminescent only at low temperature and emits only above 1 µm in the infrared domain. In the next chapter, we describe the experimental setup that was built for the exploration of such defects.

Chapter

2 Single near-infrared emitters in carbon-implanted silicon

Contents

Introduction

Capitalizing on the great success of the microelectronics industry, silicon is undoubtedly a promising platform for deploying large-scale quantum technologies. Silicon-based electrical qubits associated either to individual dopants [29] or to gate-defined quantum dots [9], have already been used to demonstrate the elementary building blocks towards scalable integrated quantum circuits. Besides requiring operation in a dilution fridge, those matter qubits are still not able to remotely exchange quantum information at long distances because they cannot be efficiently interfaced with optical light. On the other side, photonic qubits at telecom wavelengths can be generated inside silicon by probabilistic non-linear optical processes [33]. Even if they are adapted to long-distance propagation, those photonic qubits are not coupled to matter quantum systems, thus limiting the implementation of scalable silicon quantum photonics. Another type of quantum systems that could fill the gap, but is still lacking in this industry-friendly platform, are optically-active spin defects, that combines an optical interface with a solid-state medium to encode quantum information. A *sine qua non* condition to develop such spin-photon interfaces is first to demonstrate that individual point defects can be optically isolated in silicon.

Silicon features a large number of fluorescent defects emitting in the near-infrared. The report from Davies in 1989 [35] lists more than a hundred of known defects in this material. These defects have been extensively studied during the second half of the twentieth century, as their presence in the material can have a substantial effect on the electrical properties of silicon, which are paramount for semiconductor technologies. Numerous experimental methods have been exploited for their study, including electron paramagnetic resonance [68], deep-level transient spectroscopy [69], optical spectroscopy [35], and optically detected magnetic resonance [41]. All these tools were applied to silicon sample with large ensembles of defects created (i) by irradiation with electron, neutron or gamma ray, (ii) by implantation with ions or even (iii) by boiling silicon samples in water [70]. These studies have, however, always remained at the macroscopic scale on large ensembles of defects. *At the beginning of my thesis, no individual defect had ever been isolated optically at the single scale in silicon.*

The detection of single fluorescent defects in silicon first requires to design an experimental setup of optical microscopy combining a high spatial resolution, and most of all, an extreme sensitivity to detect the very weak light emission produced by single emitters. The study of silicon includes additional constraints as these emitters only emit light at cryogenic temperatures and in the near-infrared, because of the small bandgap of silicon. The design of this experimental setup, which was an empty table at the start of my PhD, will be described in the first section of this chapter (**§2.1**). To investigate individual fluorescent defects in silicon, our studies started with the analysis of a carbon-implanted silicon sample, which was used previously in our group to study the optical properties of dense ensembles of G-centers [39][1]. An in-depth analysis of this carbon-implanted sample, which lasted for about one year, led to the first isolation of single fluorescent emitters in silicon, and has enabled us to isolate seven families of optically-active point defects. Such defects have the particularity of not being reported in the literature to the best of our knowledge, likely because their occurrences are too small to be detected through ensemble measurements. These seven unidentified families of defects in silicon will be labeled SD-0 to SD-6. In the second section of this chapter, we will focus on the study of the most commonly found defect, referred to as SD-0 (**§2.2**). We will analyze in details the properties of its single photon emission and its dynamics under optical excitation. In a last section (**§2.3**), we will then investigate the other six families of single defects, SD-1 to SD-6, and carry out a comparative study of their single photon emission properties.

2.1 Low temperature confocal microscope for single-defect spectroscopy in silicon

To investigate defects in silicon and isolate them optically at the single scale, an experimental setup suited to their observation was built at the beginning of my PhD. The setup has to fulfill several requirements:

---

[1] This defect, which consists of two adjacent substitutional carbon impurities associated with an interstitial silicon atom, will be discussed in details in Chapter 3.

1. The silicon sample needs to be kept at cryogenic temperature, as the defects in this material only operate at low temperature due to its small bandgap.
2. The emitting defects have to be excited with a focused laser and their photoluminescence collected via a confocal microscope, in order to reach the spatial resolution needed to isolate them individually.
3. The microscope needs to be efficient in collecting and detecting the emitted photons, as single emitters can be dim objects with a very low photoluminescence signal.
4. The setup has to be achromatic, as an efficient excitation is performed well above the silicon bandgap with a 532 nm (2.33 eV) laser, while the photon collected from the emission of silicon defects lies in the near infrared with energies smaller than 1.17 eV, that corresponds to the silicon bandgap.

In this section, I will describe the low temperature confocal microscope which I built to isolate single emitters in silicon.

2.1.1 Cryostat operation

Since the silicon samples need to be cooled down to cryogenic temperatures, the first step in building the experimental setup was to install a liquid-Helium cryostat. To enable continuous low temperature operation over long periods of time, a closed-cycle cryostat has been chosen. The temperature of the latter can be tuned between 10 K and up to 300 K.

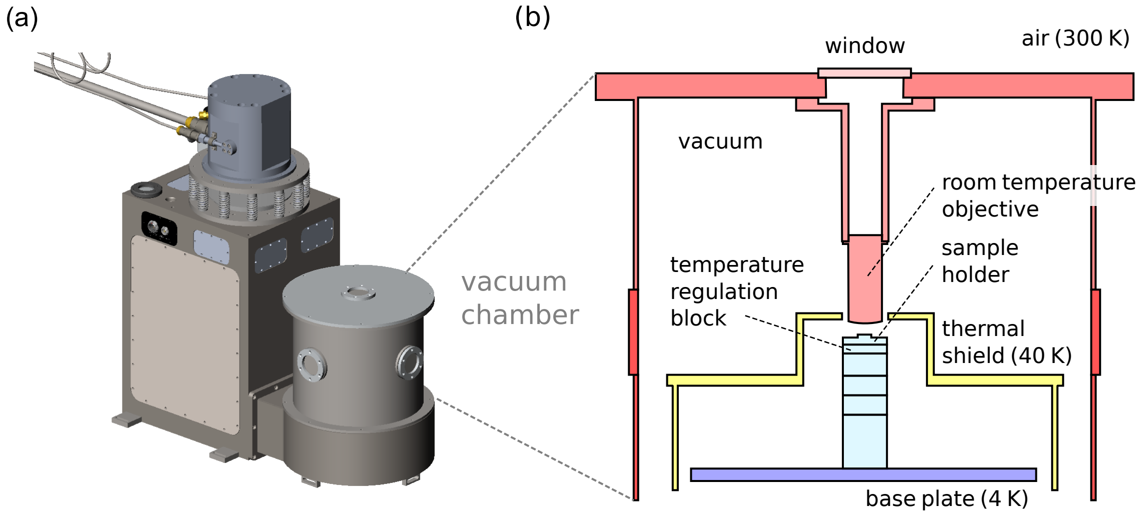

Figure 2.1: **(a)** Optidry 200 cryostat purchased from MyCryoFirm. **(b, c)** Sketch of the vacuum chamber. The parts at 4 K, 40 K and 300 K are shown respectively in blue, yellow and red. The sample tower in blue corresponds to figure 2.3. In this configuration, the microscope objective is maintained at room temperature.

The cryostat is a MyCryoFirm Optidry 200 shown in figure 2.1(a). It is composed of a main body installed on the optical table of the experimental setup, and is linked to a compressor by two Helium-filled flexible tubes. The main body includes a vacuum chamber with a vertical optical access, in which the sample is installed (figure 2.1(b)). The sample is positioned on top of a piezo-nanopositioner tower, detailed in §2.1.2, that is fixed on the base plate of the cryostat at 4 K. A thermal shield cooled to 40 K blocks the radiation heat transfer between the 4 K parts and the outer parts of the cryostat, which are maintained at 300 K. Before turning on the cryostat, a vacuum ($\approx 10^{-3}$ mbar) is done inside it. The typical time required to cool down the system is then around 8 hours, and the time for warming up to room temperature is around 20 hours. The cryostat can operate at low temperature continuously for months.

Inside the vacuum chamber (figure 2.1(b)), a room temperature microscope objective is fixed to the roof, whose temperature is at 300 K. The choice of this design is practical as it enables the use of an achromatic room temperature objective, which provides an efficient photon collection over the near-infrared range, while allowing a laser excitation at 532 nm. The drawback is that the small working distance of 1.5 mm of the microscope objective requires to drill a hole into the thermal shield to get it close to the sample, thus limiting the sample temperature to about 10 K.

The cryostat is an on/off device and does not allow, as it is, to regulate the temperature above this minimal base value. To have a fine control over the sample temperature, a temperature regulation block, which contains a thermistor and a heating resistance, is inserted in the sample tower below the sample holder. The temperature is then regulated by a controller via a proportional-integral-derivative (PID) control loop. This method enables to heat the sample up to 300 K.

Once at low temperature, the silicon sample can be analyzed optically via the vertical access through the top window of the cryostat.

2.1.2 Optical setup

The standard method to detect single emitters in the solid state is confocal scanning microscopy. Its principle is to scan optically a sample with a focused laser and detect luminescence peaks at the location of the fluorescent emitters.

Confocal microscope

A schematics of the confocal setup I built during my PhD is shown in figure 2.2.

Optical excitation of the sample

The optical excitation of the sample is realized by a green 532 nm laser. The laser beam is coupled to a monomode fiber and sent to the main experimental table shown in figure 2.2. The transformation to free space is done via a fiber collimator. Two silver protected mirrors are used on the excitation path for beam alignment. A telescope formed by two lenses is inserted to increase the beam size, in order to match the entrance pupil of the microscope objective, and to compensate for the small chromatic aberrations of this former component between the

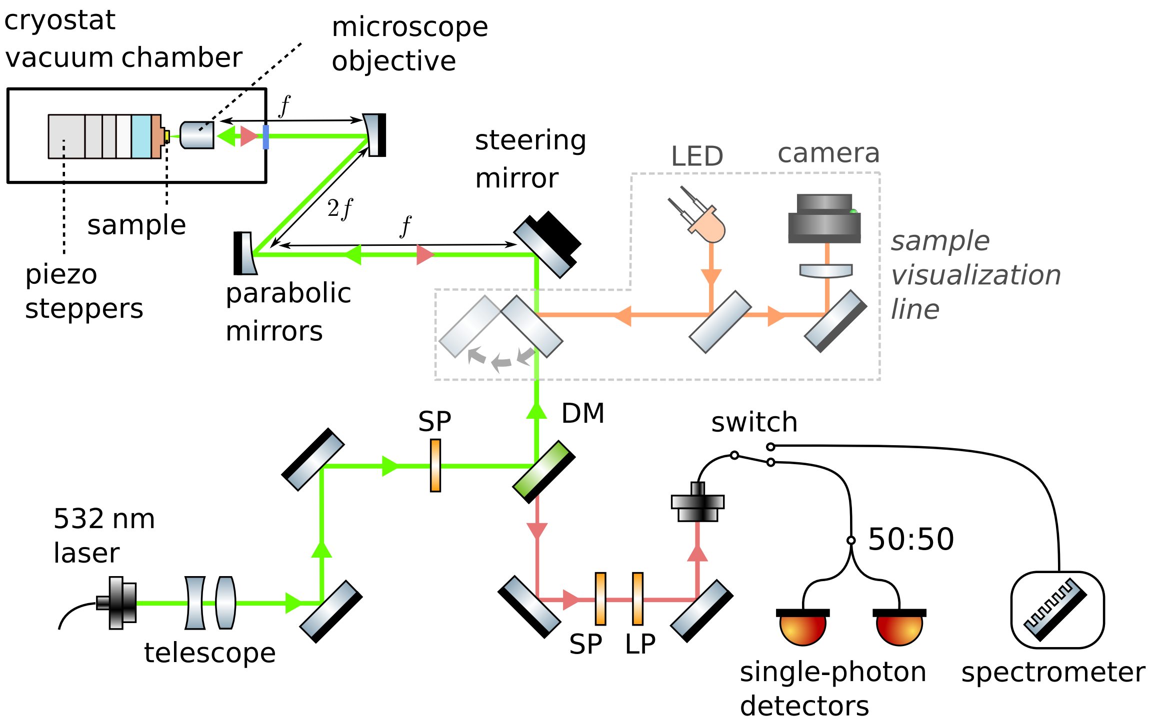

Figure 2.2: Schematic of the optical part of the experimental setup. DM: Dichroic mirror. SP: short-pass filter. LP: long-pass filter. $\lambda/2$: half-wave plate. To visualize the sample before performing measurements, the optical elements inside the dashed borders are added by inserting a movable beamsplitter.

excitation and collection wavelengths. The excitation laser beam then passes through a 1000 nm short-pass filter to remove parasitic light produced by the Raman scattering in the optical fiber.

The laser beam is then reflected by a dichroic mirror with a cut-on wavelength of 1000 nm, and sent to the steering mirror, used to scan the optical excitation over the sample (see §2.1.2). The excitation light is then sent inside the vacuum chamber of the cryostat by going through a fused silica window. The laser beam is focused onto the sample by a high numerical aperture microscope objective (Olympus LCPLN100XIR, achromatic, NA=0.85) located inside the vacuum chamber of the cryostat. To ensure that the laser beam remains inside the entrance pupil of the microscope objective while scanning the laser beam, two parabolic mirrors in a $4f$ configuration are inserted between the steering mirror and the microscope objective. Parabolic mirrors were used instead of simpler lenses to prevent for chromatic aberrations.

Photoluminescence collection

The photoluminescence of the illuminated sample is collected by the same microscope objective and follows the same path backward up to the dichroic mirror where it is transmitted towards the collection line. A long-pass 1050 nm filter is used to remove residual light from the excitation laser. In addition, supplementary short-pass or long-pass filters which are mounted on motorized filter wheels, can be added to the collection line.

The sample photoluminescence is then coupled into a monomode optical fiber with an anti-reflection coating. The fiber coupling is done using a silver reflective collimator to prevent chromatic aberrations. A remote-controlled fibered optical switch then sends the collected photons either to single-photon detectors or to a spectrometer equipped with a nitrogen-cooled InGaAs camera. Two single-photon detectors are used in an Hanbury Brown and Twiss configuration (HBT) [71], in order to perform the second-order autocorrelation measurement, as described in §2.2.1. The detectors used are InGaAs/InP avalanche photodiodes (ID Quantique ID230) working in the single-photon regime, with a quantum efficiency of 10 % at 1.3 µm.

In this setup, the core of the collection monomode fiber ($d = 8.2\,\mu\text{m}$) plays the role of a confocal pinhole that implements a spatial filtering on the collected luminescence, thus enabling to increase the spatial resolution of the microscope and the contrast of the optical scans.

Sample visualization

To image the sample surface, a visualization line can be used by adding a removable pellicle beamsplitter between the dichroic mirror and the steering mirror. This pellicle beamsplitter is mounted on a motorized filter flip mounts. The sample surface is illuminated by an orange LED in conjunction with an aspheric condenser lens with diffuser. Its image is focused on a visualization camera with an achromatic doublet lens. This camera is also very useful to visualize the reflection of the laser on the sample surface during the alignment procedure of the confocal microscope.

Optical scans of the sample

Sample positioning

Our silicon samples have a typical size of 5 by 5 mm and a thickness of 1 mm. As the steering mirror only enables the exploration of an area of about 160 µm × 120 µm, the sample is mounted on a tower of nanopositioners used for coarse positioning on the scale of a few millimeters. This tower, depicted in figure 2.3, is made of three linear piezo-stepper nanopositioners (X, Y, Z)

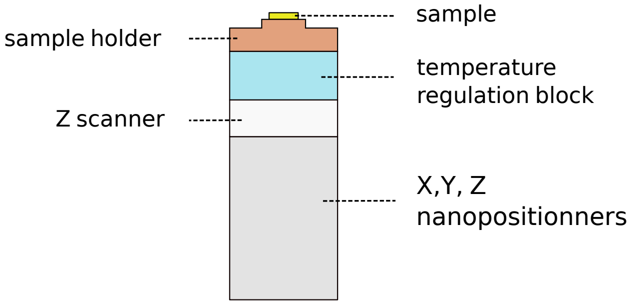

Figure 2.3: Sample tower used to position the sample at the focal point of the microscope objective.

with a range of 5 mm each, and a Z piezo-scanner (30 µm) for fine-positioning. The sample is glued with silver paint on a custom sample holder and a temperature regulation block, which is fixed to the nanopositioners. This tower is used to lift the sample to the microscope objective focal plane before recording optical scans.

Recording photoluminescence raster scan images

To record optical raster images of the sample, the mean photoluminescence intensity is measured at each point of the sample, by scanning the excitation laser spot using the steering mirror. In practice the number of photons per pixel is counted using an acquisition card, which has a clock frequency synchronized with the rotation of the steering mirror. The maximum area of the optical scans can reach 160 µm by 120 µm. Figure 2.4(a) shows a typical photoluminescence raster scan of a carbon-implanted silicon sample recorded with a 20 ms acquisition time per pixel.

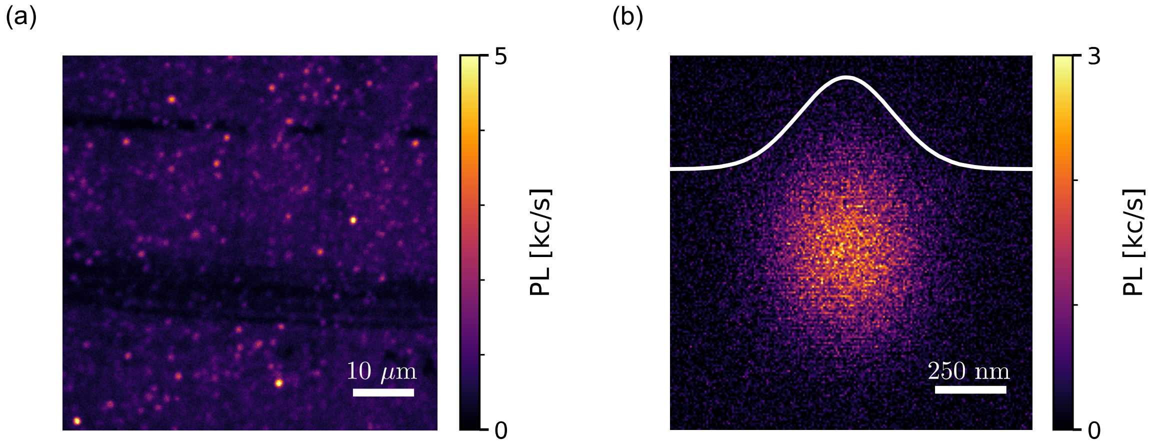

Figure 2.4: Photoluminescence raster scan images. **(a)** Typical photoluminescence scan of a carbon-implanted silicon sample recorded at 10 K, with an excitation laser of 10 µW at 532 nm. The isolated hotspots are associated to the emission of single fluorescent defects, as demonstrated in §2.2.1. **(b)** Zoom on an isolated luminescence spot. The scan is recorded at 1 µW, well below the saturation power of the single defect. A Gaussian fit of an image cut is performed (solid white line) to extract the FWHM resolution of 436(5) nm.

A zoom on one isolated emitter excited below its saturation power is shown in figure 2.4(b). By fitting a linecut of the image to a Gaussian function, we obtain a full width at half maximum (FWHM) of 436(5) nm. This value can be compared to the diffraction-limited resolution of the confocal microscope given by the equation [72]:

$$r = \frac{0.4\lambda}{\mathrm{NA}} \tag{2.1}$$

where r is the resolution defined as the FWHM, λ is the excitation wavelength and NA is the numerical aperture of the microscope objective. Using $\lambda = 532\,\mathrm{nm}$ and $\mathrm{NA} = 0.85$, we find $r \approx 250\,\mathrm{nm}$. As this value is roughly twice smaller than the measured FWHM of the emission spot, we conclude that the spatial resolution of our confocal microscope is not limited by diffraction. This discrepancy might be linked to a problem in the alignment of the setup, but it could also be linked to the excitation process in these optical scans. As the above bandgap laser excitation creates free carriers which eventually recombine at the location of the defect, the diffusion length of these carriers should also be taken into account to determine the effective size of the excitation spot. Since this diffusion length is unknown, we cannot confirm definitively this hypothesis.

The measurement of the photoluminescence raster scans, as well as all the other experiments described in this chapter, require the use of a control software to synchronize the multiple instruments and record the resulting signals. The open source solution used to perform this control is discussed in the next section.

2.1.3 Experimental control and data acquisition

Data acquisition requires a large amount of instrumental interfacing and control. For instance, to record the optical scans of figure 2.4, the steering mirror is rotated to change the position of the excitation laser focus point, the voltage pulses from the single-photon detector are counted synchronously, and an image is constructed pixel by pixel in real time. The realization of hour-long complex acquisitions can require multiple feedback loops: optimizing the focus position to compensate for drifts, swapping the fibered switch, etc. Some of the results presented in this manuscript were acquired continuously for several days in total, limiting the use of *manual* approach.

The need for a user-friendly, advanced but flexible, open-source control software has led to the development of a collaborative Python framework called Qudi [73], which has been initiated by the group of Fedor Jelezko in Ulm (Germany). This efficient modular approach has attracted many labs of the spin defect community to participate in this project. The solution is free and versioned via Git, which enables us to use it extensively for all the setups of our research group.

Qudi - a collaborative Python framework

In our experimental setup, a total of 14 different instruments connected to 4 distinct computers are used. Dedicated computers are required for instruments with particular interfacing (GPIB, PCIe, etc.). To perform each specific acquisition, a set of design rules have been established within Qudi to control every device. Each instrument is controlled by a single Qudi *hardware module*, which handles the communication with the device, and translates the Qudi generic instructions into device-specific instructions.

Logic modules then supervise the *hardware* modules and perform the acquisition control. One challenge for an open-source project is that the models and the manufacturers vary greatly for equivalent instruments. To have *logic* modules compatible with multiple devices, applications programming interfaces (API) labeled simply *interfaces* are defined to standardize the communication of the *logic* modules with the *hardware* modules.

Finally, *graphical user interface (GUI)* modules handle the creation of windows, buttons and plots to interact with the logic modules and visualize the data acquisitions in real time. The clear separation of the *GUI* modules from the *logic* modules allows an alternative control of the acquisitions: user written Python script can interact with the *logic* modules and perform any available action, to create complex new acquisitions and control loops.

The three layer approach (*GUI / logic / hardware*) is at the heart of Qudi's success as it allows a handy operation of complex setups, and the realization of scripted tools. This is particularly useful considering that multiple hundreds of emitters in total have been studied during the course of my PhD. This extensive study has led to the first detection of seven new families of single defects in silicon, which will be presented in the next sections.

2.2 First detection of a single fluorescent defect in silicon

To look for single fluorescent emitters in silicon, which could have many applications for quantum technologies, we start by investigating a silicon sample which has undergone ion implantation to voluntarily create defects in the material. As our initial goal was to detect the G-center in silicon, which is a carbon-related defect, we start from a silicon sample implanted with carbon ions. The silicon sample investigated in this section is a commercial Silicon-On-Insulator (SOI) structure purchased from Soitec, which is the standard platform used for integrated photonics with silicon [74]. The SOI is made of a 220 nm-thick silicon layer separated from the bulk silicon substrate by 1 µm of silicon dioxide (SiO_2) (figure 2.5). The top layer was implanted with carbon ions at a fluence of $5 \times 10^{13}\,\mathrm{cm}^{-2}$. An implantation energy of 36 keV was chosen to ensure that the carbon atoms stop on average 100 nm below the surface and thus remain in the top silicon layer. In order to heal the silicon lattice from the implantation damages, a flash annealing of 20 seconds at 1000 °C under N_2 atmosphere has been subsequently performed.

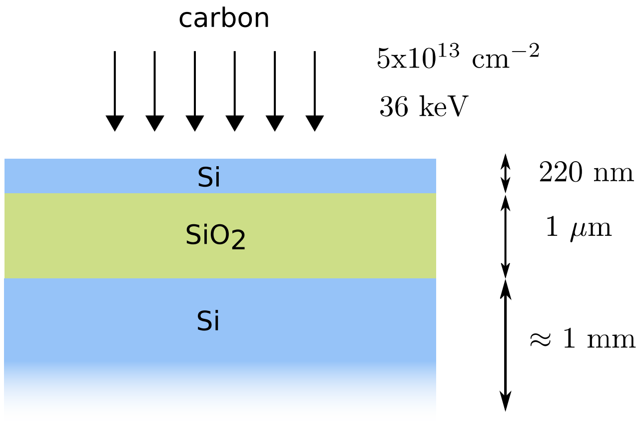

Figure 2.5: A standard commercial silicon-on-insulator structure is implanted with carbon ions with an energy of 36 keV and a fluence of $5 \times 10^{13}\,\mathrm{cm}^{-2}$.

2.2.1 Isolation of single defects

A first step of the sample exploration is to record a photoluminescence scan with an above bandgap excitation at 532 nm. Contrary to the diamond material which is transparent in the visible domain, this wavelength is absorbed by silicon with a penetration depth of 1.3 µm for 532 nm [75]. This light absorption leads to the creation of free carriers (figure 2.6(a)) in the top silicon layer. These free carriers cannot recombine efficiently in pure silicon as it is an indirect bandgap semiconductor, but they can be captured by point defects, which then leads to radiative recombinations. A typical luminescence scan recorded at a temperature of 10 K is displayed in figure 2.6(b). A striking observation is that there are isolated hotspots of emission, which are randomly distributed over a dimmer luminescence background. These hotspots suggest the presence of isolated optically active defects in silicon.

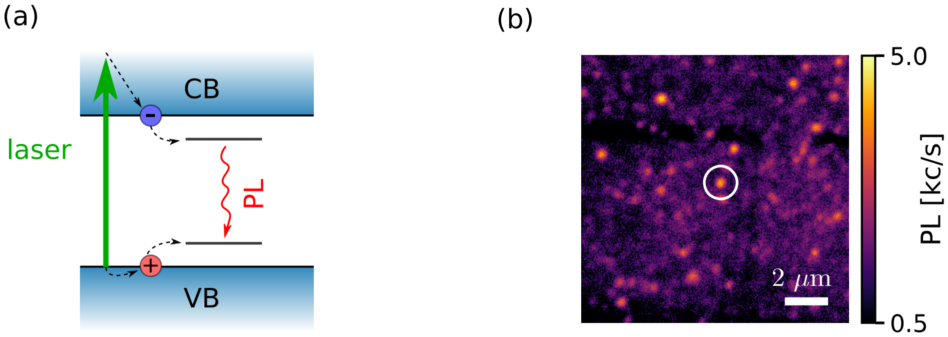

Figure 2.6: (a) Sketch of the photoluminescence process of defects with an above bandgap excitation laser. **(b)** Photoluminescence scan of the carbon-implanted silicon sample recorded at 10 K with a green laser excitation of 10 µW. The emitter circled in white is used to demonstrate the single-photon emission in figure 2.8.

To demonstrate that the localized emission stems from a single defect, the standard method is simply to show that it emits photons one by one. This is commonly done by analyzing the correlations of the luminescence photons via the measurement of the second-order autocorrelation function $g^{(2)}(\tau)$, and then by showing that $g^{(2)}(0) < 0.5$ [76]. The second-order autocorrelation function $g^{(2)}(\tau)$ is defined by the equation [77]:

$$g^{(2)}(\tau) = \frac{< I(t)I(t+\tau) >}{< I(t) >^2}, \tag{2.2}$$

where $I(t)$ is the luminescence signal at time t, and $< \ldots >$ is the temporal average over time. The $g^{(2)}(\tau)$ function is linked to the conditional probability of detecting a photon at time $t = \tau$, given that a photon has been detected at time $t = 0$. For a time τ much longer than the characteristic emission lifetime of the emitter, the photons arrive independently. As a consequence, the intensities $I(t)$ and $I(t + \tau)$ are uncorrelated and therefore $g^{(2)}(\tau \rightarrow \infty) = 1$. At zero delay, on the other hand, as a single defect can only emit one photon at a time, the probability of detecting two photons within a delay much shorter than the excited level lifetime

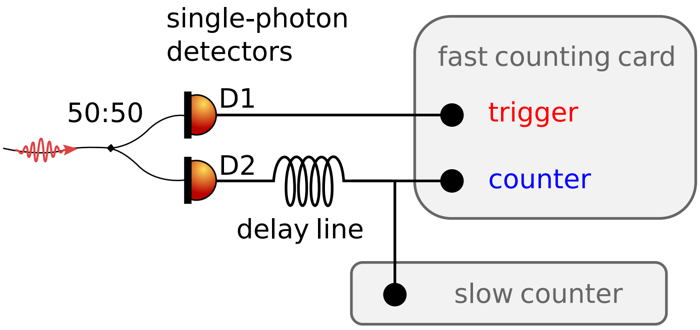

Figure 2.7: Schematics of the Hanbury Brown and Twiss setup.

tends toward zero, *i.e.* $g^{(2)}(0) = 0$. For N identical emitters, this zero-delay value is given by $g^{(2)}(0) = 1 - \frac{1}{N}$ [78]. The emission from a single emitter must therefore fulfill the condition $g^{(2)}(0) < 1/2$, a phenomenon referred to as photon antibunching.

Hanbury Brown and Twiss setup

The measurement of the $g^{(2)}(\tau)$ function can theoretically be done with a single detector. In practice, the deadtime of the detectors (typically 30 ns) is however on the same order or even longer, than the excited level lifetime of the emitter, and thus prevents the detection of a clear antibunching effect. To get rid of this deadtime, we measure the autocorrelation function $g^{(2)}(\tau)$ using two detectors in a Hanbury Brown and Twiss configuration (HBT) [71], as shown in figure 2.7. The idea of this setup is to use two single-photon detectors, D1 and D2, at the output of a 50:50 fibered beamsplitter. A commonly used measurement scheme, referred to as "start-stop" mode, consist in recording the histogram of the time intervals between two *consecutive* single photon detections. Once properly normalized to a Poissonian light source, the recorded histogram is equivalent to the second-order correlation function $g^{(2)}(\tau)$ provided that $\tau \ll R^{-1}$ where R is the photon detection rate [79].

In order to record the $g^{(2)}(\tau)$ function without any temporal restrictions, the HBT setup was rather used to measure $J(\tau)$, defined as the number of photons detected at time τ provided that a photon is detected at time $t = 0$. To this end, a photon detection event on detector D1 was used to trigger the acquisition of a photoluminescence time trace on detector D2 using a large-range time-to-digital converter (Fastcomtec 7889, 100 ps time resolution). After N repetitions of the measurement, the resulting time trace $J(\tau)$ is directly linked to the second-order correlation function through:

$$g^{(2)}(\tau) = \frac{J(\tau)}{NwR_2} \tag{2.3}$$

where w is the bin time of the recorded trace, and R_2 is the photon detection rate on detector D2. To measure R_2 properly, the detector output pulses of detector D2 are duplicated and recorded at the same time by a slow counting module, during the full acquisition. A delay line (50 m of cable) introduces a constant delay ($\approx 250\,\mathrm{ns}$) on the *counter* channel to circumvent the deadtime of the fast-counting card, and also to artificially shift the zero-delay of the measurement. Once properly normalized, the $g^{(2)}(\tau)$ function can then be analyzed to demonstrate the single photon emission.

Demonstration of single photon emission

The recorded $g^{(2)}(\tau)$ function for a localized emitter is plotted in figure 2.8 and displays a strong antibunching at zero delay $g^{(2)}(0) \approx 0.3$. As this value goes under the threshold of 1/2, this antibunching effect is the signature of single photon emission that can only be produced by a single emitter. This measurement constitutes the first isolation of a single fluorescent defect in silicon.

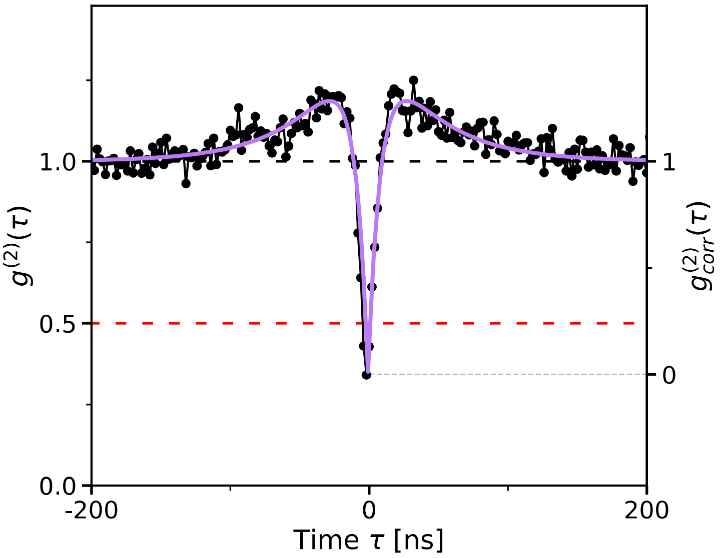

Figure 2.8: Second-order autocorrelation function $g^{(2)}(\tau)$ recorded from an isolated luminescence spot. The background-corrected $g^{(2)}_{\mathrm{corr}}(\tau)$ function is shown on the right axis. The solid line is a fit using the 3-level model described in §2.2.3.

The deviation from an ideal single-photon emission, *i.e.* $g^{(2)}(0) = 0$, can arise from residual background photons and detector dark counts, which both produce uncorrelated counts. To check that the single photon purity is limited by the background, the second-order autocorrelation function can be corrected using the formula [76]:

$$g^{(2)}_{corr}(\tau) = \frac{g^{(2)}(\tau) - (1-\rho^2)}{\rho^2}, \tag{2.4}$$

where $g^{(2)}_{corr}(\tau)$ is the background-corrected autocorrelation function and ρ is linked to the signal-to-noise ratio (SNR) by $\rho = 1/(1 + 1/\mathrm{SNR})$. For the measurement shown in figure 2.8, the SNR is around SNR $= 4.3$. This SNR was determined by recording the luminescence signal at the position of the defect and a few micrometers away. The background-corrected $g^{(2)}_{corr}(\tau)$ function is shown on the right axis in figure 2.8. It displays an antibunching effect going to zero, as expected for a pure single-photon emitter. It should be noted that the jitter of the single photon detectors have a negligible contribution in this experiment, because its characteristic time (150 ps) is much smaller than the characteristic time of the antibunching dip (≈ 10 ns). At intermediate delay, we also note that the $g^{(2)}(\tau)$ function rises above one, indicating a *bunching* of the photons. This effect, which is linked to the presence of a third level in the dynamics of the emission, will be discussed later in §2.2.3.

Photoluminescence spectrum

The photoluminescence spectrum of the single emitter is displayed in figure 2.9. It features a sharp optical line at ≈ 1.27 µm, that is associated with a zero-phonon line (ZPL), and a broad phonon-sideband which extend up to 1.4 µm. The proportion of the photons emitted inside the ZPL, referred to as the Debye-Waller factor (DW), reaches 15 % for this defect. In comparison, it is 5 times higher than the one of the NV center in diamond. A high DW factor is valuable for applications in quantum communications, as only the ZPL emission can be used to achieve photon indistinguishably, which is at the heart of many protocols in quantum information science [80]. Remarkably, the defect photoluminescence lies within the telecom O-band, used for standard communications via optical fibers.

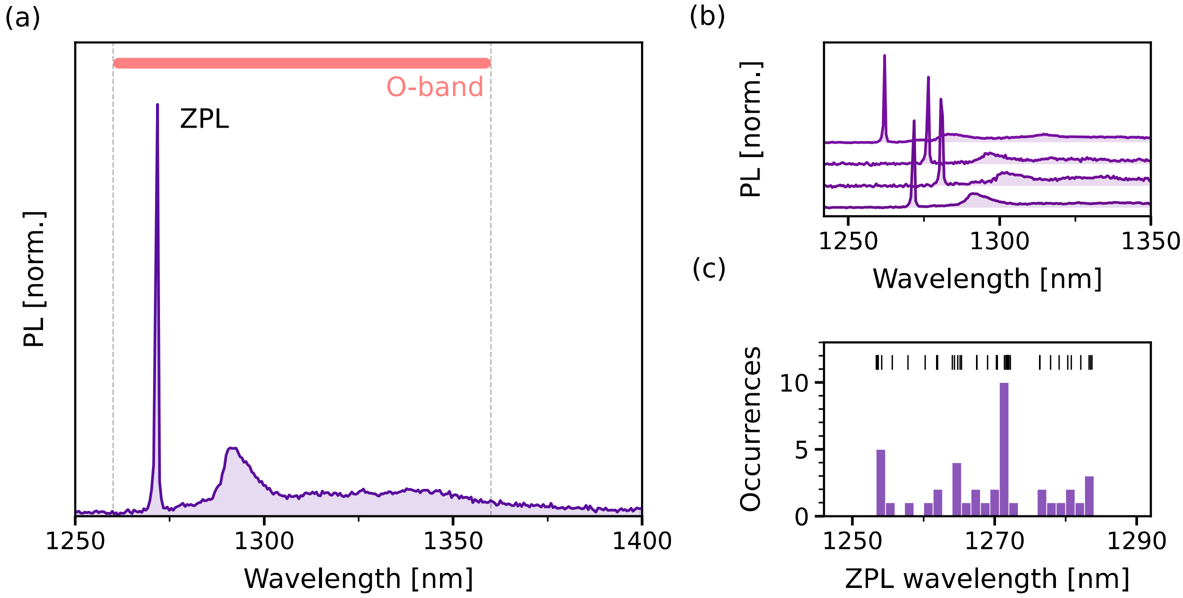

Figure 2.9: Spectral properties of the SD-0 defect. **(a)** Photoluminescence spectrum recorded on a single SD-0 emitter. The thick solid line shows the telecom O-band spanning from 1260 nm to 1360 nm. **(b)** Typical spectra taken on 4 single emitters. The spectra are normalized by their maximum of intensity. **(c)** Histogram of the zero-phonon line wavelength measured for a set of 41 single emitters. The wavelength is extracted by fitting the zero-phonon peak with a Gaussian function. Thin lines above the histogram represent the exact value of each data point.

This spectral signature does not enable a straightforward identification with known defects in silicon from the literature [35]. As discussed in more detail in chapter 3, this emission does not correspond to the G-center in silicon as initially believed [81]. In consequence, we will label it SD-0 (for single defect 0) in this manuscript.

A comparison of the photoluminescence spectra of several single photon emitters (figure 2.9(b)) reveals that their emission spectra are identical in the shape of their ZPL and their phonon-sideband. However, their ZPL emissions are shifted in wavelengths by tens of nanometers. Fluorescent defects in semiconductors commonly display such fluctuations in their emission wavelength because of different local environments [52, 82]. To quantify these fluctuations for SD-0 emitters, the photoluminescence spectra of 41 single emitters were recorded. The histogram of the ZPL wavelength is plotted in figure 2.9(c). The large dispersion likely results from local strain or electrostatic inhomogeneities in the carbon implanted sample [83, 84]. It should be noted, however, that the distribution is sharp at specific wavelengths, such as 1272 nm where more than 10 emitters have been found.

We have demonstrated that individual emitters can be isolated in silicon, leading to a single photon emission. Furthermore, these emitters have an emission at telecom wavelength, which is interesting for future applications in quantum communication. In the next section, we will investigate further the properties of the single photon emission.

2.2.2 Properties of single photon emission

Defect photostability

An important property of any individual solid-state defect acting as a single photon source is its photostability over time. Many photoluminescent objects are indeed known to exhibit blinking behavior [85–87], or permanent bleaching [88], which corresponds to the irreversible conversion of an optically active defect into a non-fluorescent entity. A typical photoluminescence time trace recorded over 30 minutes (figure 2.10(a)) demonstrates that the SD-0 emission is perfectly photostable. Furthermore, the defects are robust against repeated thermal cycles from 10 K to room temperature and are still present 2 years after their first observation.

Saturation curve

Another critical parameter of single photon emitters is their maximum luminescence rate under optical excitation. To perform this characterization, the photoluminescence level is recorded as a function of the laser power (figure 2.10(b)). The resulting luminescence first increases with the laser power, and then saturates to a maximum signal around ≈ 9 kc/s. Such behavior corresponds to the standard saturation of an optical transition. It should be noted that the plotted luminescence is corrected from the background luminescence, which was also recorded by moving the laser focus a few micrometers away from the defect. This background signal was used to compute the signal-to-noise ratio used in the correction of the second-order autocorrelation function (see §2.2.1). To extract precise values for the emitter maximum intensity and the laser

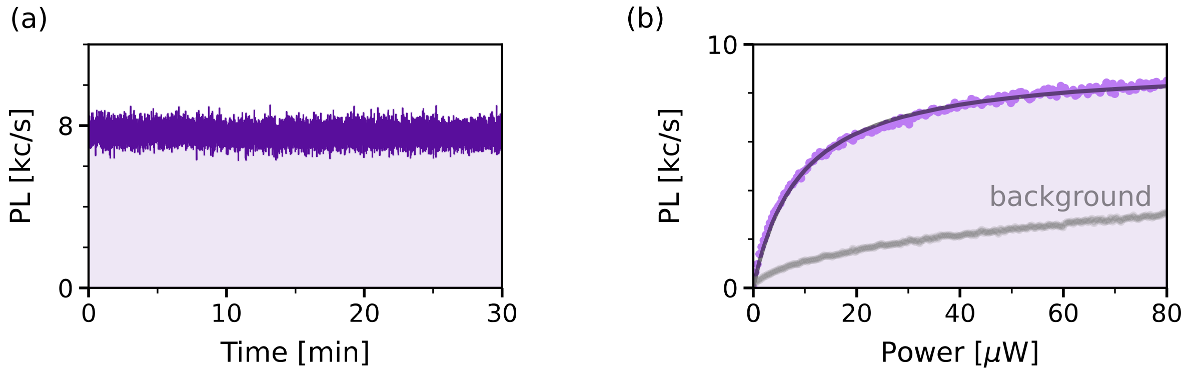

Figure 2.10: **(a)** Typical photoluminescence time trace recorded on a SD-0 emitter while saturating the optical transition. The bin time is 60 ms per point. **(b)** Photoluminescence saturation curve of a single SD-0 emitter. The data are acquired on the emitter and on the background a few micrometers away from the defect. The subtraction results in the photoluminescence stemming only from the emitter, which is plotted. The data points for the background are shown in gray. The photoluminescence from the emitter is fitted with equation 2.5, leading to a saturation power $P_{\text{sat}} = 9.1(1)\,\mu\text{W}$ and a maximum signal rate $S_{\text{sat}} = 9.2(1)$ kc/s.

power required to saturate the optical transition, the saturation curve is fitted with the standard saturation model given by the equation:

$$S(P) = S_{\text{sat}} \frac{P}{P + P_{\text{sat}}}, \tag{2.5}$$

where $S(P)$ is the photoluminescence rate, P is the laser power, P_{sat} is the saturation power and S_{sat} is the maximum photoluminescence rate. A fitting of the data leads to $S_{\text{sat}} = 9.2(1)$ kc/s and $P_{\text{sat}} = 9.1(1)\,\mu\text{W}$. It should be noted that this emission rate is typical for the SD-0 defect, but some single photon emitters of this family can reach a counting rates up to 16 kc/s.

Evolution of the photon count rate with temperature

Up to now all of the measurements on the single emitters have been performed at 10 K, the minimum temperature reachable with the experimental setup. To study the effect of a higher temperature on the single photon emission, saturation curves were recorded for temperature ranging between 10 K and 120 K (figure 2.11(a)). The measurement reveals that the maximum intensity does not vary with the temperature, but that only the laser power required to saturate the optical transition increases.

To extract a quantitative evolution, the saturation curves are fitted with the saturation model given by equation 2.5 to extract the evolution of the parameters P_{sat} and S_{sat} with the temperature. The results of the fit are displayed in figures 2.11(b) and (c). A first observation is that the saturation power P_{sat} rises exponentially with increasing temperatures. This effect stems from the thermal activation of non-radiative decay channels, as will be corroborated by the decrease of the excited level lifetime with temperature in §2.2.3. The most striking feature is related to the intensity at saturation: the maximum photon count rate S_{sat} stays roughly

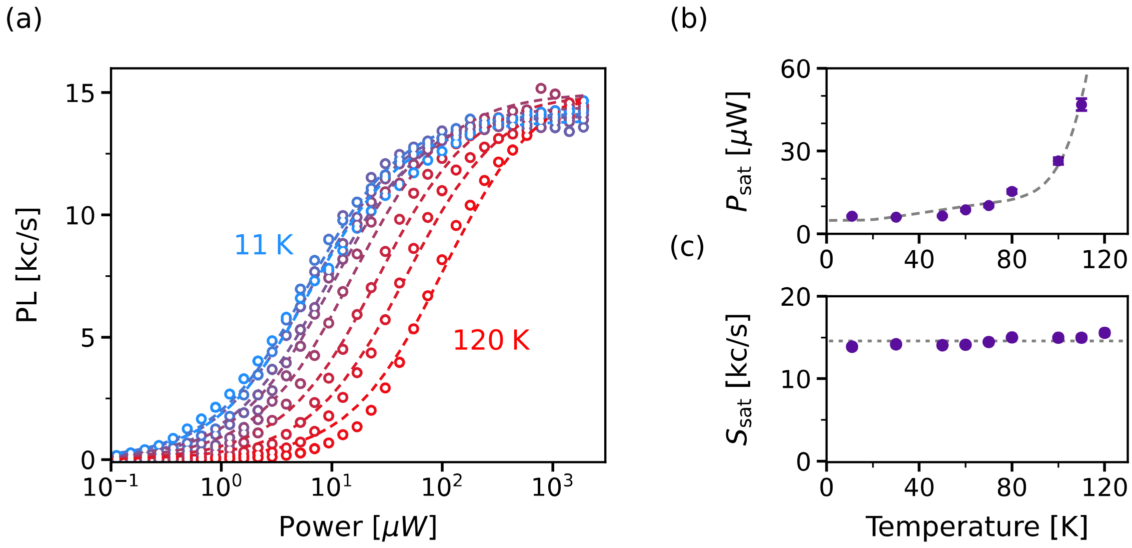

Figure 2.11: **(a)** Background-corrected photoluminescence saturation curves measured on a single SD-0 emitter for varying temperatures. The temperatures used are 11, 30, 50, 60, 70, 80, 100, 110, 120 K. The data are fitted with equation 2.5 to extract the saturation power P_{sat} and the maximum signal rate S_{sat}. The data is plotted in semi-log scale for visualization. **(b, c)** Evolution of P_{sat} and S_{sat} with temperature. The dashed lines are guides for the eye.

constant up to 120 K. This high luminescence is promising for future applications, as it is well above the 77 K liquid-nitrogen temperature, a regime accessible without the need for an expensive helium-based cooling system. Here the exploration of the luminescence above 120 K was limited by the background luminescence, which became prominent with the very high laser power needed to excite the defect.

Polarization of the single photons

We now characterize the polarization properties of the single photon emission. To this end, a half-wave plate and a polarizer were installed in front of the single-photon detectors. A polarization diagram was then recorded by monitoring the photoluminescence signal while rotating the half-wave plate (figure 2.12(a)). After subtraction from the unpolarized background counts, the recorded diagram features a modulation with a contrast close to unity, indicating that the defect has a linearly polarized emission. This feature is interesting as linearly polarized emission is preferable for applications in quantum technologies.

Furthermore the polarization of the light emitted by a defect is linked to its emission dipoles and can provide information on the defect orientation and symmetries. Here the observed linear polarization demonstrates that the defect behaves as a single emitting dipole [89]. As the angle of the polarized light can reveal information about this dipole orientation, the polarization of the emission was analyzed according to the sample orientation. Here the measured polarization of emission shown by an arrow in figure 2.12(a) indicates the projection of the emission dipole on the (0 0 1) sample surface. The orientation of the sample, which is illustrated in figure 2.12(b), enables us to compare the dipole orientation to the crystallographic axis of silicon. For the data plotted in figure 2.12(a), the projection of the emission dipole on the (0 0 1) top surface makes an angle $\phi \approx 10°$ with respect to the [1 1 0] direction. A systematic analysis over a set of 29 single SD-0 defects (figure 2.12(c)) reveals that the emission dipoles are pointing in specific directions distributed across four subgroups, which exclude the [1 1 0] and [$\bar{1}$ 1 0] axis. The variations of the dipole orientation suggest a low symmetry of the SD-0 defect, which might be intrinsic or linked to strain inhomogeneities in the sample. We will see in chapter 3 that defects with a trigonal C_{3V} symmetry along a ⟨1 1 1⟩ axis are always aligned along one of these two directions.

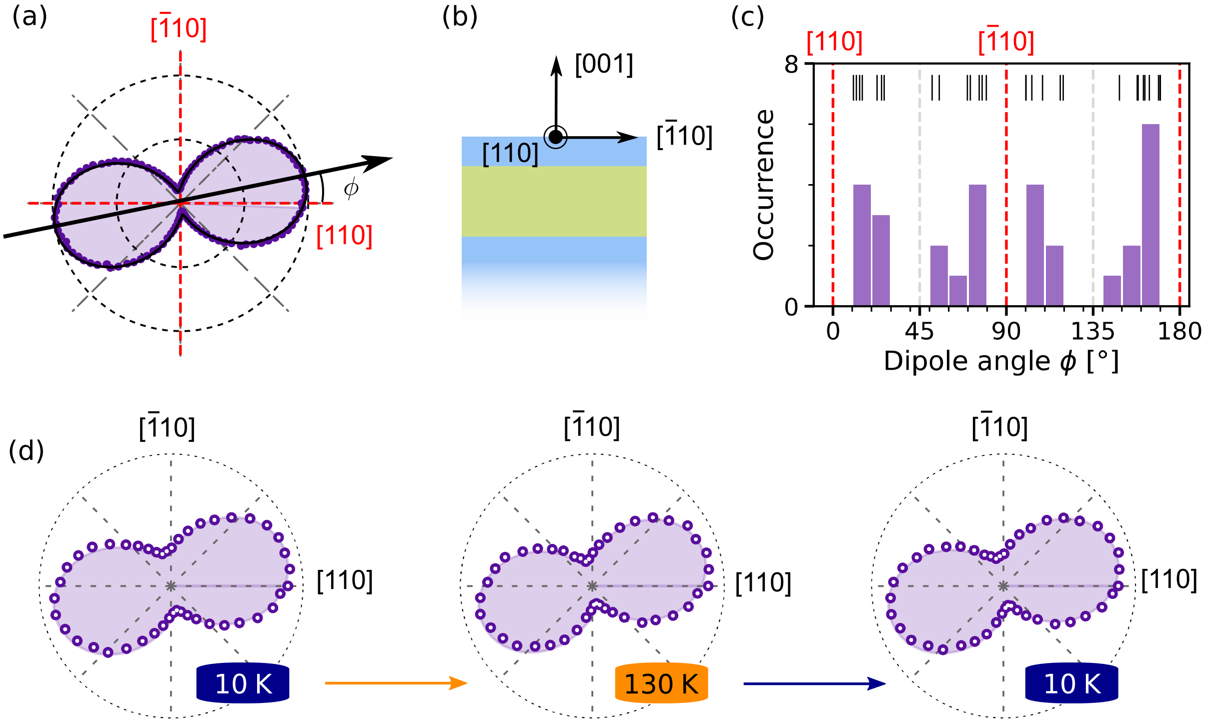

Figure 2.12: Photon polarization analysis of a single SD-0 defect. **(a)** Polarization diagram of the photoluminescence emission from a single emitter. The emission dipole has a projection (black arrow) on the (0 0 1)-oriented SOI sample pointing at $\phi \approx 10°$ from the [1 1 0] crystal axis. **(b)** Schematics of the silicon sample crystallographic orientations. **(c)** Histogram of the angle ϕ measured for a set of 29 individual centers. Thin lines above the histogram represent the exact value of each data point. **(d)** Polarization emission diagrams measured successively at different temperatures on a single SD-0 center. For (d) the recorded visibility is due to an imperfect correction of the background signal.

To investigate potential atomic displacement or reconfiguration of the defect at higher temperature that could impact the emission dipole [35, 41], we measured the emission polarization diagram of a single defect at different temperatures. Figure 2.12(d) shows the polarization diagram taken first at 10 K, then at 130 K and finally at 10 K again. No modification of the polarization emission diagrams are observed. We thus conclude that no reorientation of the defect occurs while increasing the temperature.

The analysis of the single photon emission has revealed some very appealing properties for a single photon source. The emission is at telecom wavelength, perfectly linearly polarized, stable and relatively bright. As a matter of fact, a typical count rate signal of $S_{\mathrm{sat}} \approx 10\,\mathrm{kc/s}$ is surprisingly high for a single defect in bulk silicon. Indeed, the high refractive index of silicon ($n \approx 3.5$) leads to total internal reflections at the silicon-air interface with a critical angle of about 17°. It will be shown in §2.2.4 that at most $\approx 2\,\%$ of the photons exit the silicon sample with an angle collected by the microscope objective. In addition, the photon detectors used in this measurement had a quantum efficiency around only $10\,\%$. We will see in §2.2.4 that a careful analysis of the efficiency of our setup indicates that the quantum efficiency of SD-0 defect is close to unity.

To increase the photoluminescence count rate signal S_{sat}, significant improvement can be achieved by simply using a superconducting single-photon detectors featuring a quantum efficiency up to $90\,\%$. These detectors were purchased near the end of my PhD and will be used for the study of single G-centers in the next chapter. Further improvement could also be attainable in the future by integrating the single photon emitters into silicon photonic structures, to guide the emitted light out of the silicon with an angle collected by the microscope objective [90, 91].

2.2.3 Analysis of the dynamics of optical cycles

We now investigate the dynamics of SD-0 optical cycles by performing time-resolved measurement and by analyzing the evolution of the $g^{(2)}(\tau)$ function while increasing the optical excitation power.

Excited level lifetime

The excited level lifetime τ_e defines the characteristic time at which the populations prepared in the excited level decay to another level. To measure the lifetime for the SD-0 defects, a pulsed laser excitation at 532 nm with a 50 ps pulse duration is used to excite the defect. The time-resolved luminescence signal is then recorded with a fast-counting card, measuring the decay of the photoluminescence. The result recorded on a single defect (figure 2.13(a)) shows a mono-exponential decay of the photon counts, corresponding to the decay from the excited level. To extract the lifetime of this excited level, the data are fitted with an exponential function, leading to $\tau_e = 32.8(6)$ ns for this defect.

To check the reproducibility of this value, a similar measurement is performed on 29 individual SD-0 defects (figure 2.13(b)). The resulting distribution is centered around $\langle \tau_e \rangle = 35.8(2)$ ns, but reveals a fluctuation of this excited level lifetime by a standard deviation $\sigma_{\tau_e} = 3.5(2)$ ns. It should be noted that such a fluctuation is unusual compared to the one commonly observed for point-defects in diamond crystals [54], but seems to be present for other defects in silicon (see chapter 3). Its origin is not yet fully understood and requires further investigations.

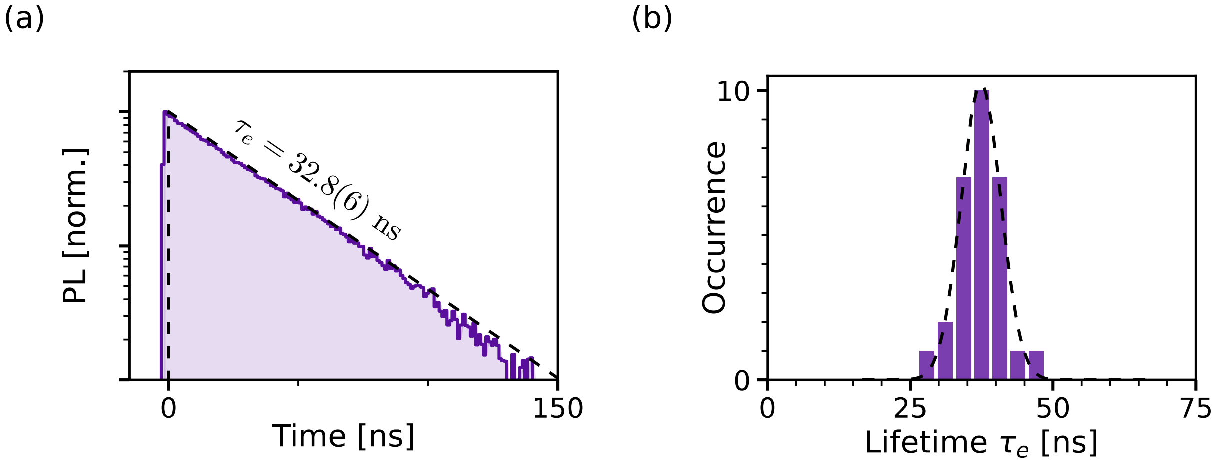

Figure 2.13: Excited level lifetime of single SD-0 defects. **(a)** Time-resolved photoluminescence decay in semi-log scale recorded under optical excitation with 50 ps (FWHM) laser pulses at 532 nm. The excited level lifetime τ_e is extracted through data fitting with a single exponential function. **(b)** Histogram of lifetimes τ_e measured on 29 individual SD-0 emitters. The dashed line is a fit with a Gaussian function leading to a standard deviation of $\sigma_{\tau_e} = 3.5(2)$ ns

The excited level lifetime of a defect fixes its maximum luminescence rate according to the formula:

$$R_{\text{max}} = 1/\tau_e \times \eta_{\text{QE}} \ ,$$

where R_{max} is the maximum number of emitted photons and η_{QE} the quantum efficiency. For a fixed quantum efficiency, having a short lifetime around 30 ns is therefore appealing as it sets the maximum photoluminescence signal that can be detected. As a comparison, the T-centers in silicon, a defect recently investigated for its spin properties, has an excited level lifetime of 940(1) ns [36]. Rate-earth ions like the Erbium dopants have an even longer lifetime of 1 ms [92].

Evolution of the excited level lifetime with temperature

To explore the effect of temperature on the SD-0 defect photodynamics, the measurement of the excited level lifetime is repeated for increasing temperatures (figure 2.14(a)). It appears that at higher temperatures, the decay of the excited level populations is still mono-exponential, but with a shorter characteristic lifetime. The curve for each temperature is fitted with an exponential model to extract the excited level lifetimes $\tau_e(T)$ (figure 2.14(b)). The resulting lifetime has a monotone decrease, indicating a drop of the SD-0 excited level lifetime with temperature. A general rule of any light emitter is that its excited level lifetime is set by the relation

$$\frac{1}{\tau_e} = k_{\text{r}} + k_{\text{nr}} \ ,$$

where k_{r} and k_{nr} denotes the radiative and non-radiative recombination rates, respectively. The decrease of the defect lifetime in silicon is generally induced by the activation of non-radiative decay processes with increasing temperatures [35,39], as illustrated in figure 2.14(c). The data on the single SD-0 defect do not appear to follow a simple exponential energy activation model [39], which likely indicates that more than one non-radiative recombination process is involved in the reduction of the excited lifetime with temperature. A more quantitative analysis of the evolution of the lifetime of the SD-0 defect would require additional experiments which are going beyond the scope of this thesis.

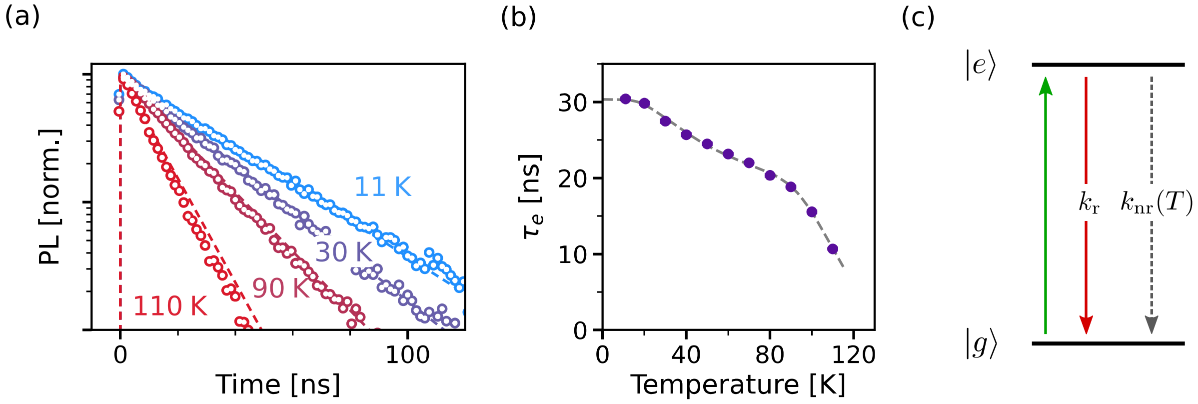

Figure 2.14: Evolution of the excited level lifetime with temperature. **(a)** Time-resolved photoluminescence decay in semi-log scale of a single SD-0 defect measured at different temperatures. The dashed lines represent data fitting with a single exponential function used to extract the excited level lifetime τ_e. **(b)** Evolution of τ_e with temperature. The error bars are smaller than the markers. The dashed line is a guide for the eye. **(c)** Schematics of the optical cycle. When the system is excited, it can decay radiatively at a rate k_r or non-radiatively at the rate $k_\mathrm{nr}(T)$.

Evolution of the second-order autocorrelation $g^{(2)}(\tau)$ with the excitation power

Another method to probe the SD-0 photodynamics is to analyze further its second-order autocorrelation function $g^{(2)}(\tau)$. Indeed the measurement of the $g^{(2)}(\tau)$ function while varying the optical excitation power can be exploited to study the dynamics of the level populations on the nanosecond timescale. Figure 2.15(a) displays the background-corrected $g^{(2)}_{corr}(\tau)$ functions recorded on a single SD-0 defect for different laser powers. To guarantee that only photons from the single defects are considered, the corrected functions are computed via equation 2.4. This set of measurements reveals that the antibunching dip narrows with the laser power and that, in addition, a *photon bunching* effect (*i.e.* $g^{(2)}(\tau) > 1$) is observed at low power. This observation suggests that the optical cycle involves a non-radiative relaxation process through a metastable level [76], as depicted in figure 2.15(b). Interestingly, the bunching effect gradually disappears while increasing the laser power, until the $g^{(2)}(\tau)$ mimics the dynamics of a pure 2-level system (top curve). This peculiar behavior can be explained by considering a photo-induced detrapping transition from the metastable level to the excited level (see figure 2.15(b)). This process likely contributes to the high brightness of single emitters under green laser illumination.

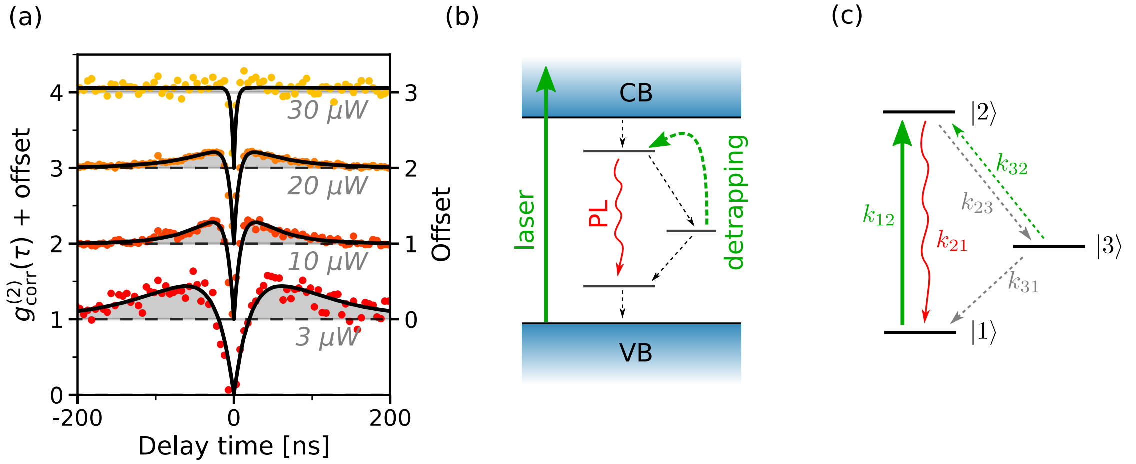

Figure 2.15: Analysis of the autocorrelation function $g^{(2)}(\tau)$ dynamics with different excitation powers. **(a)** $g^{(2)}_{\mathrm{corr}}(\tau)$ function with increasing laser excitation power. Data are corrected from background counts with equation 2.4 and fitted with the formula of equation 2.7 (solid lines). **(b)** Schematics of the SD-0 optical cycles under laser excitation. **(b)** Three-level model used to describe the dynamics of optical cycles.

Modeling of the $g^{(2)}(\tau)$ function

To get more insights into the photodynamics, the emitter can be modeled by the 3-level system (3LS) [93] shown in figure 2.15(c). Once optically excited from the ground level $|1\rangle$ to the excited level $|2\rangle$, the defect can relax into its fundamental level following two paths: either through a direct radiative transition or via a non-radiative transition involving a metastable level $|3\rangle$. For this 3-level system, the $g^{(2)}_{3\mathrm{LS}}(\tau)$ function can be expressed in terms of the population of the excited level p_2 following the formula

$$g^{(2)}_{3\mathrm{LS}}(\tau) = p_2(\tau)/p_2(\infty) \ ,$$

where $p_2(\infty)$ represents the steady-state population of level $|2\rangle$. The time evolution of the population $p_i(t)_{\{i\in[1,2,3]\}}$ can be then computed by solving the following rate equations :

$$d\vec{p}/dt = \mathbf{A}\vec{p} \ ,$$

where $\vec{p}(t) = \{p_i(t)\}_{i\in[1,2,3]}$ and

$$\mathbf{A} = \begin{pmatrix} -k_{12} & k_{21} & k_{31} \\ k_{12} & -k_{21}-k_{23} & k_{32} \\ 0 & k_{23} & -k_{31}-k_{32} \end{pmatrix} . \tag{2.6}$$

Here the parameter k_{ij} denotes the rate from level $|i\rangle$ to level $|j\rangle$, as depicted in figure 2.15(c). The two boundary conditions are $g^{(2)}_{3\mathrm{LS}}(0) = 0$ considering an ideal single-photon source and $g^{(2)}_{3\mathrm{LS}}(\infty) = 1$, since all correlations are lost at long timescale. Using those conditions and given that the matrix $\mathbf{A}$ has two non-zero eigenvalues, the general formula for the autocorrelation function can be written as follows [94]:

$$g^{(2)}_{3\mathrm{LS}}(\tau) = 1 - (1-a)e^{-\Lambda_0\tau} + ae^{-\Lambda_1\tau} \tag{2.7}$$

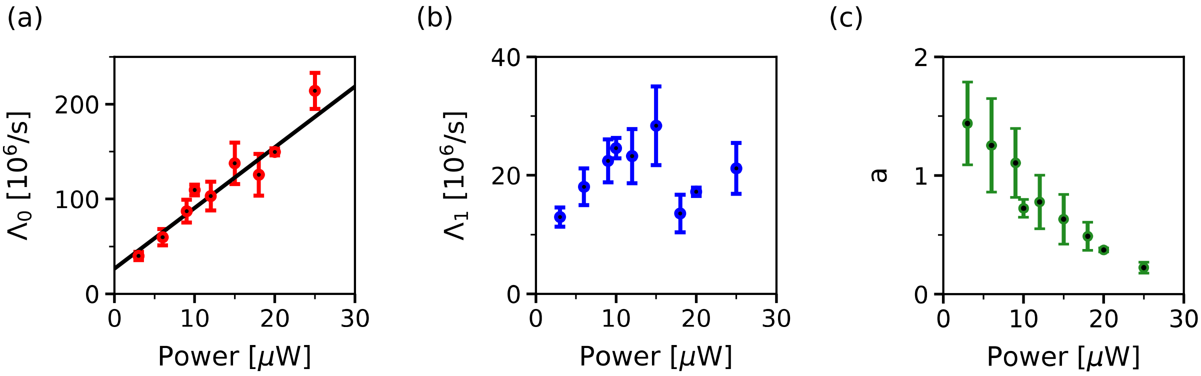

Figure 2.16: Evolution of the $g^{(2)}(\tau)$ parameters fitted with equation 2.7 as a function of the excitation power. **(a, b)** Evolution of the rates Λ_0 and Λ_1 with increasing optical power, respectively. The solid line corresponds to a linear fit. The rates for 30 µW excitation power are not shown as the fit did not properly converge. **(c)** Evolution of the parameter a versus the optical power.

with the three parameters a, Λ_0 and Λ_1 being non-trivial functions of the rates k_{ij} of the model. In first approximation, the second term $-(1-a)e^{-\Lambda_0 \tau}$ describes the antibunching effect at short timescale, while the last term $ae^{-\Lambda_1 \tau}$ dominates the bunching behavior at long timescales.

Using equation 2.7, the $g^{(2)}_{\text{corr}}(\tau)$ function of figure 2.15 are fitted to extract the parameters Λ_0, Λ_1 and a at each laser power (figure 2.16). The rate Λ_0, which is associated with the antibunching effect, increases linearly with the optical power, reflecting the narrowing of the antibunching dip, a well-known effect resulting from the shortening of the average time between two consecutive photon detections, due to the predominance of the pumping rate over the emission rate at high powers [95]. When the optical power tends to zero, the rate Λ_0 should lead to the inverse of the excited level lifetime τ_e [95]. From a linear fit of the data, the value at the origin gives a lifetime of $1/\Lambda_0 = 37(9)$ ns, in good agreement with the value measured on the same center by time-resolved photoluminescence: $\tau_e = 32.8(6)$ ns. The rate Λ_1, linked to the bunching effect, seems to have a linear increase below 15 µW, which would suggest an optically-induced recovery from the metastable level. However, as the values above 15 µW do not follow the same behavior, no simple interpretation can be given of this evolution. In a 3-level model where $k_{32} = 0$, the bunching amplitude a increases with optical power [95]. Here on the contrary, this parameter decreases towards zero at high optical power in our experiment. This behavior can be qualitatively understood by considering the presence of an effective transition rate k_{32} increasing with optical power, which transfers the population from the metastable level $|3\rangle$ to the excited level $|2\rangle$, likely through the conduction band. Unfortunately, quantitative estimates of the physical rates k_{ij} cannot be obtained here as the resulting uncertainties are too large.

Building a proper level-model of the single photon emission could enable a better understanding of its photodynamics. This has been demonstrated in chapter 1 where the NV center photodynamics was better understood by building a 7-level model. To further study the SD-0 fluorescence, time-resolved luminescence with μs-long laser pulses could enable the measurement of the metastable level lifetime in the dark. Another option would be simply to use more efficient single photon detectors and a longer acquisition time to reduce the error bars. As the measurement time of the $g^{(2)}(\tau)$ function increases with the square of the photoluminescence signal, this study has been postponed to a later time when new superconducting nanowire single-photon detectors (SNSPD) would be operational.

As a last characterization on the single photon emitter, we try to give a lower bound to its quantum efficiency in the next section.

2.2.4 Quantum efficiency estimation

The quantum efficiency η_{QE} of a single emitter quantifies its probability to emit a photon once it has been prepared in its excited level. This figure is important as, together with the lifetime, it determines the maximum emission rate $R_{\max} = 1/\tau_e \times \eta_{\mathrm{QE}}$. To estimate the quantum efficiency of this single photon emitter, the number of detected photons was recorded under a pulsed optical excitation. Laser pulses of duration $\delta t = 50\,\mathrm{ps}$ were used, far shorter than the excited level lifetime $\tau_e = 28.5(5)\,\mathrm{ns}$. As a result, the probability of emitting two photons per pulse, which is given by $1 - exp(-\delta t/\tau_e) \approx 2 \times 10^{-3}$, can be safely neglected. In addition a repetition period of 270 ns was used, which is much longer than the emitter's lifetime. From the histogram of counts (figure 2.17), the probability of detecting a photon per single optical excitation pulse was determined to be $P_{\mathrm{photon}} \approx 4.1 \times 10^{-4}$.

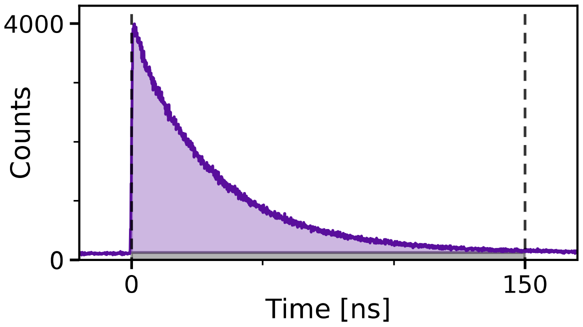

Figure 2.17: Histogram of the photoluminescence counts measured on a single defect under a 50 ps pulsed laser excitation at 532 nm. The measurement sequence was repeated 2.8 billion times. A binwidth of 100 ps was used. Counts are integrated in the window $[0, 150\,\mathrm{ns}]$ (shaded area), subtracted from noise counts (gray shaded area), and finally divided by the number of sweeps to get the probability to detect a photon per optical excitation $P_{\mathrm{photon}} \simeq 4.1 \times 10^{-4}$.

The average photon number per excitation P_{photon} can be linked to the emitter's quantum efficiency η_{QE} following the formula:

$$P_{\mathrm{photon}} = \eta_{\mathrm{QE}} \cdot \eta_{\mathrm{coll}} \cdot T_{\mathrm{setup}} \cdot \eta_{\mathrm{det}} \tag{2.8}$$

where η_{coll} is the photon collection efficiency from the sample, T_{setup} the setup transmission and η_{det} the detector efficiency. By using the maximal collection efficiency η_{coll}^{Max} corresponding to a dipole optimally placed in the top layer and parallel to the sample surface, a lower bound of the quantum efficiency can be estimated according to the equation:

$$\eta_{\mathrm{QE}} \geqslant \frac{P_{\mathrm{photon}}}{\eta_{\mathrm{coll}}^{\mathrm{max}} \times T_{\mathrm{setup}} \times \eta_{\mathrm{det}}} \tag{2.9}$$

In order to compute this lower bound for η_{QE}, we next estimate T_{setup} and $\eta_{\mathrm{coll}}^{\mathrm{max}}$.

Optical transmission of the setup (T_{setup})

The main elements limiting the transmission of photons from the microscope objective to the detector are:

- the microscope objective transmission (≈ 70%),
- the transmission through the cryostat window (≈ 87%),
- the imperfect mirror reflection (≈ 98% per mirror, 7 mirrors in total),
- the fiber coupling efficiency (≈ 85%),
- the loss from connecting fibers (≈ 90%).

The total transmission of the setup T_{setup} from the microscope objective to the detector is therefore of ≈ 40%.

Maximal collection efficiency through the microscope objective ($\eta_{\mathrm{coll}}^{\mathrm{max}}$)

The emitter is located inside a silicon top layer with a high refractive index (n=3.5) (figure 2.18(a)), which acts as an optical waveguide through total internal reflection with a critical angle of about 17°. Only a small fraction of the luminescence can therefore escape towards free space and be collected by the microscope objective within its numerical aperture [96]. It should also be taken into account that the photon collection efficiency η_{coll} depends on the position of the emitter and on the orientation of its optical dipole. These effects have been analysed by our collaborator Jean-Michel Gérard through numerical simulations of the emission properties of emitters embedded in the SOI layer, using Finite-Difference Time-Domain methods (FDTD).

As we want to get a lower bound estimate of the quantum efficiency, we consider the most pessimistic case corresponding to the most favorable configuration for the photon collection, *i.e.* where the optical dipole is parallel to the plane of the interfaces. Figure 2.18(b) shows how the photon collection η_{coll} evolves as a function of the depth d of the emitting dipole. It reaches a minimum value of 0.5% when the dipole lies in the middle of the silicon layer. At this depth, the emitter is located at the antinode of the fundamental guided mode, which maximizes preferential photon funneling into this mode, at the expense of the leaky modes [96]. By contrast, a better extraction of the emitted photons out of the SOI slab is obtained when the emitter is close to the top or the bottom of the SOI layer, with η_{coll} reaching a maximum value around $\eta_{\mathrm{coll}}^{\mathrm{max}} = 2\,\%$.

From equation 2.9 and using this highest possible value $\eta_{\mathrm{coll}}^{\mathrm{max}}$, a lower bound for the quantum efficiency of the SD-0 emitters, $\eta_{\mathrm{QE}} \gtrsim 50\%$ is obtained. This relatively high quantum efficiency is part of the reason why this single emitter has a high luminescence level, and is promising for

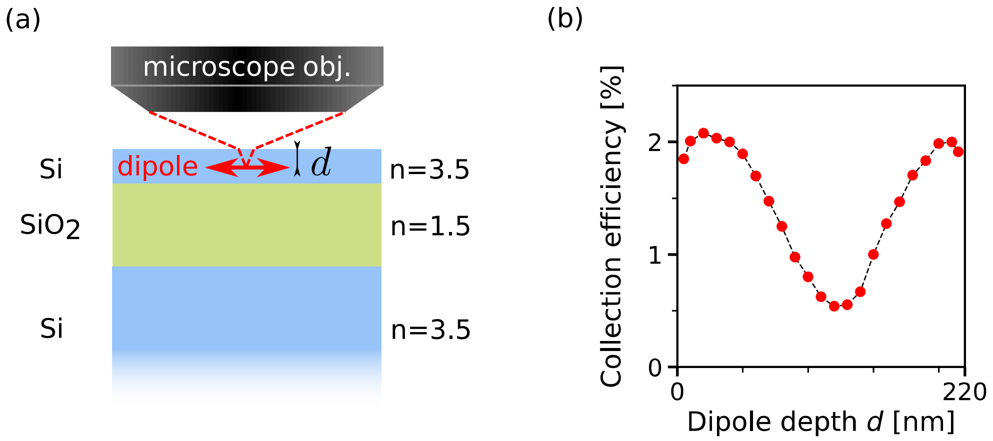

Figure 2.18: Estimation of the quantum efficiency. **(a)** Schematics of the simulated structure. The emitter dipole is assumed to be lying in the plane perpendicular to the surface, as this configuration maximizes the photon collection. **(b)** Evolution of the collection efficiency η_{coll} as a function of the depth d of the embedded emitter.

future applications.

In this section, we have presented the first optical isolation of a single emitter in silicon. This emitter, labeled SD-0, is found in a carbon implanted sample and exhibits a stable, linearly polarized, single-photon emission in the telecom O-band. In addition to the SD-0 emitter which was prominent in the investigated sample, 6 other families of defect have been identified, as discussed in the next section.

2.3 Six families of unidentified single defects in silicon

Carbon impurities in silicon are known to produce a large variety of defects, with at least 14 photoluminescence lines attributed to complexes based on this contaminant in the literature [35]. Their study has up to now been done at the ensemble level, where only the most frequent defects can be detected. The detection of individual defects in carbon-implanted silicon opens a new pathway to study these defects, especially those with rare occurrences.

To investigate the defects present in the carbon implanted sample, photoluminescence scans were first acquired to mark the position of isolated bright spots. Figure 2.19 displays a typical scan where 25 isolated spots can be examined. A systematic analysis of the photoluminescence spectra revealed a broad diversity of emission spectra, likely corresponding to different defects. For practical reasons, emitters with a zero-phonon line or an intense emission were mainly explored. An analysis of the photoluminescence spectra over 633 hotspots in total enabled the identification of 6 additional families of optically active defects. These defects are labelled SD-1 to SD-6 in the following.

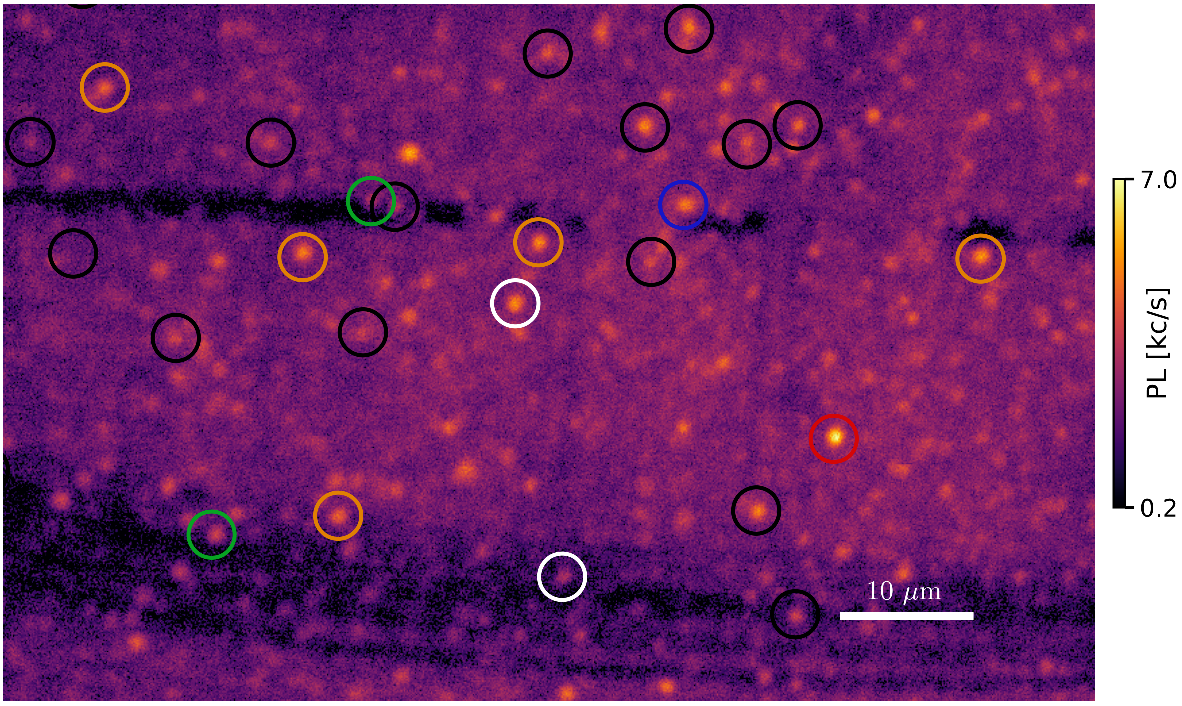

Figure 2.19: Photoluminescence scan of the carbon-implanted silicon sample. Circles mark the positions of defects studied via luminescence spectra. Black circles correspond to defects which did not display a zero-phonon line or a clearly identifiable luminescence. White circles correspond to SD-0 single defects. Colored circles mark the defects belonging to the 6 newly identified families with a color code matching the figure 2.20.

2.3.1 Spectral properties

Isolation of 6 new families of single defects

A typical photoluminescence spectrum for each of the 6 family is displayed in figure 2.20(a). To demonstrate that they correspond to single defects, the autocorrelation function $g^{(2)}(\tau)$ was acquired for each family and are displayed in figure 2.20(b). All defects show a clear antibunching effect that fulfill the single-emitter condition $g^{(2)}(0) < 0.5$. Furthermore, they all emit in the near-infrared region, but their photoluminescence spectrum strongly differ from one defect to another. While the zero-phonon line (ZPL) dominates over the phonon-sideband for families SD-0 to SD-2, it becomes less and less intense for families SD-3 and SD-4, until not being detectable at all for families SD-5 and SD-6. The Debye-Waller factor, which quantifies the portion of photons emitted in the ZPL, varies from 35 % for SD-1 to below the detectable levels for SD-5 and SD-6. The value of the Debye-Waller factor for each family is given in table 2.1, which summarizes the defect's spectral properties. The number of defects per family in our statistics is shown in figure 2.20(c). These numbers demonstrate that while some families are relatively frequent (SD-2 & SD-4), others, such as SD-1, are very rare and represent less than 0.4 % of the defects probed during our study. It should be noted that no correlation was found between the defects types and their location in the sample.

The SD-2 defects might be related to an interstitial carbon defects C_i associated to an emission line at 1448 nm [35, 97]. This hypothesis will be discussed further in this section. The other emitters, however, do not appear to be assigned to common luminescent defects in silicon previously identified in the literature through optical spectroscopy on large ensembles [35, 98].

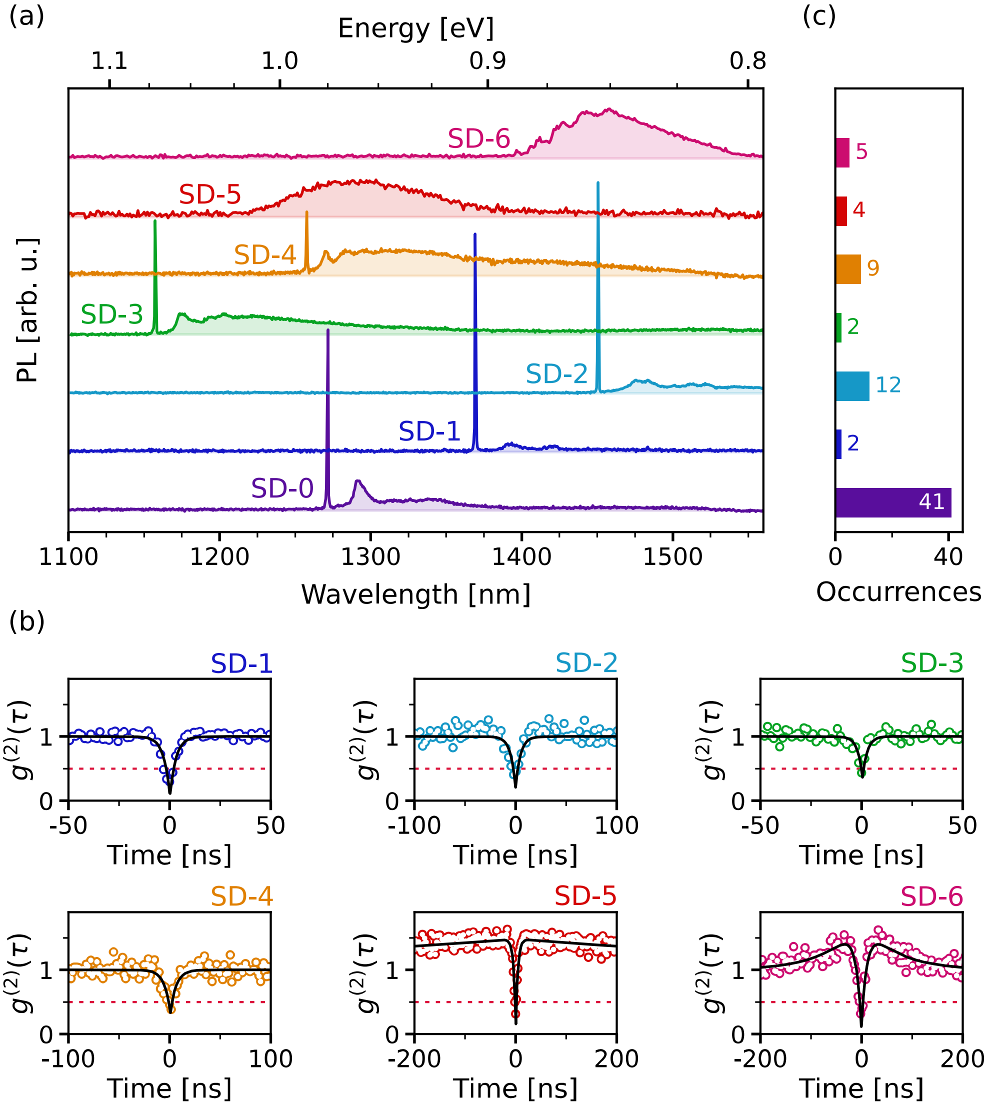

Figure 2.20: Families of single defects isolated in a carbon implanted SOI sample. **(a)** Photoluminescence spectra recorded on six additional single-photon emitters. **(b)** Second-order autocorrelation function $g^{(2)}(\tau)$ corresponding to the individual defects from families SD-1 to SD-6. No background correction is applied. Data are fitted with the model of equation 2.7 with an additional constant offset. The optical powers used are respectively 2, 4, 3, 3, 2 and 4 times the saturation power of the corresponding defects. **(c)** Histogram of the number of defects per family.

Family	SD-0	SD-1	SD-2	SD-3	SD-4	SD-5	SD-6
Spectrum with ZPL	Yes	Yes	Yes	Yes	Yes	No	No
ZPL wavelength [nm]	1269(9)	≈ 1369	1448(5)	≈ 1157	1253(7)	-	-
ZPL energy [meV]	977(7)	≈ 905	856(3)	≈ 1071	989(6)	-	-
Debye-Waller factor [%]	15	35	25	3	2	-	-
1^{st} phonon replica energy [meV]	14.5	14.5	14.5	14.5	9.5	-	-

Table 2.1: Summary of the spectral properties for the different families of single defects. ZPL uncertainties for families SD-0, SD-2 and SD-4 correspond to the standard deviation calculated over the full family set.

Spread of the zero-phonon lines between defects

Optically active defects are generally identified by their zero-phonon line wavelength. To characterize the new isolated defects, a histogram of the zero-phonon line wavelengths is plotted in figure 2.21(a). Each family set is well separated in wavelength from the others, except for the distributions of the SD-0 and SD-4 emitters that are partially overlapping. These last centers are, however, clearly distinguishable by the strong difference of their Debye-Waller factor and phonon-sideband structure.

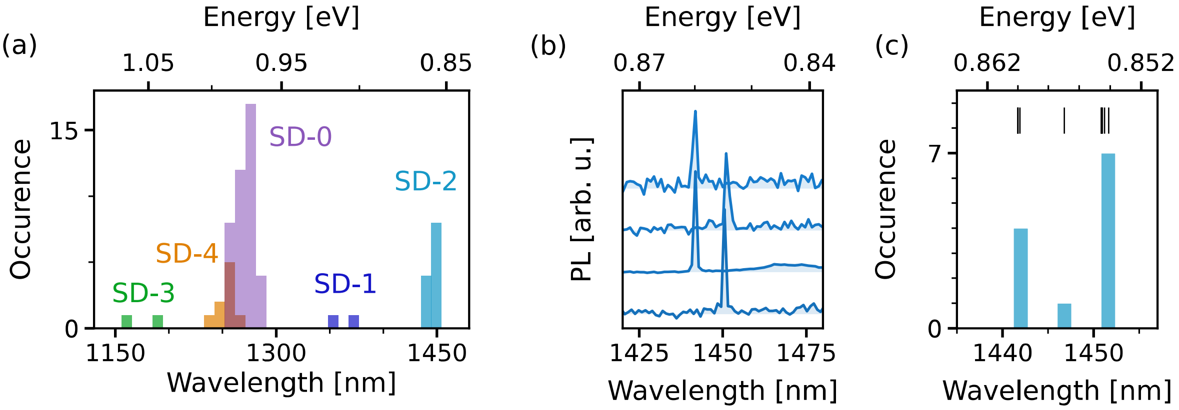

Figure 2.21: Zero-phonon line spread between individual defect families. **(a)** Histogram of the zero-phonon line wavelength measured on the defects of all families featuring a zero-phonon line. **(b)** Typical photoluminescence spectra measured on 4 individual defects of family SD-2. **(c)** Histogram of the SD-2 family zero-phonon lines wavelengths. Thin lines above the histogram represent the exact value of each data point.

The large set of SD-2 defects observed during our measurements allow to perform a more precise study of the dispersion of the ZPL wavelength. Figure 2.21(b) shows the spectra of 4 single emitters, with a zero-phonon line seemingly at reproducible positions. A histogram computed from the set of 12 defects (figure 2.21(c)), reveals that the wavelengths for all SD-2 emitters are found at roughly 3 positions equally split around 1448 nm. Such a behavior suggests the presence of three defect configurations for the SD-2 defect. The small dispersion inside each configuration is very appealing for future applications requiring indistinguishable photons, as it demonstrates that the emission of this defect is weakly sensitive to the local environment.

Comparison of the phonon-sideband spectra

To extract further information from the defect luminescence spectra, the phonon-sidebands are analyzed. Figure 2.22 plots the photoluminescence spectra of each family in energy scale and with respect to the zero-phonon line. The first phonon replica, visible as a peak relative to the ZPL position, is either at 9.5 meV (SD-4) or at 14.5 meV (SD-0 to SD-3), reflecting the energy of the phonons involved in the optical transitions. It should be noted that the phonon-sideband of family SD-6 exhibits a similar periodicity of 9.5 meV. Since these energies do not correspond to any of the maxima of the silicon phonon density of states (shown in gray in figure 2.22), the vibronic spectrum likely results from phonons combining localized and Bloch vibrational states [99].

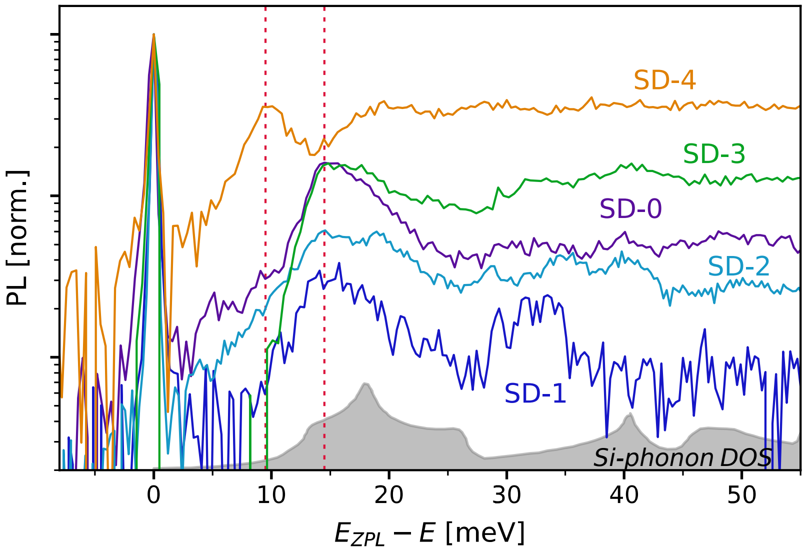

Figure 2.22: Comparison of the phonon-sideband for the defects with a zero-phonon line. Spectra are normalized to the zero-phonon line maximum and plotted in semi-log scale with respect to their zero-phonon-line energy E_{ZPL}. The vertical lines show the positions of the first phonon replica at 9.5 and 14.5 meV. The gray-shaded area indicates the silicon phonon density of states [100].

In addition to the detailed study of the spectral properties of these new defects, their isolation at the single defect scale allows an in-depth characterization of the defects stability and count rates per emitter, as discussed in the next section.

2.3.2 Photostability and count rates

A first important observation is that all defects are photostable with neither blinking nor bleaching observed while recording their luminescence over time. Furthermore, most defects do not fade away after room temperature warming up followed by cooling down to 10 K. Only defects of the SD-5 family either disappear or appear in optical scans after warming-up cycles of the cryostat. This phenomenon is illustrated in figures 2.23(a, b, c) where a first scan measured at 10 K contains an isolated emitter which corresponds to the SD-5 family, as demonstrated by its photoluminescence spectrum. After a cryostat warming-up to 300 K, a second scan recorded at 10 K on the same area reveals that the emitter is no longer visible. The opposite effect can be seen in scans where new SD-5 emitters appears, as shown in figures 2.23(d, e, f).

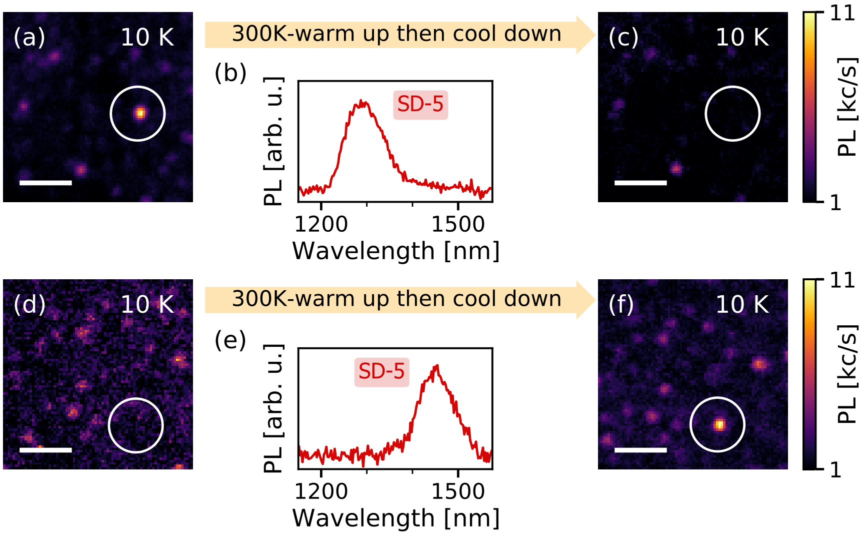

Figure 2.23: Vanishing and appearance of SD-5 defects with thermal cycles. **(a, d, c, f)** Photoluminescence scans acquired at 10 K on 2 sample areas before (a,d) and after (c,f) a warming-up of the cryostat to 300 K. Horizontal bars correspond to 5 µm. **(b, e)** Photoluminescence spectra associated with the SD-5 family and recorded on the bright spots circled in (a) and (f), respectively.

Maximal photon count rates

The maximal photoluminescence intensities for each defect is on the order of 10 to 20 kc/s, similarly to the SD-0 defect (see table 2.2 for values). The SD-5 emitters - unstable at room temperature - exhibit a particularly bright emission which stands out in the photoluminescence scans. It should be noted that this study preselected the emitters with a high luminescence signal. As a result, emitters with an intensity below ≈ 5 kc/s have not been investigated.

Evolution of the saturation curves with temperature for the SD-2 defects

The stability of the SD-2 defects with temperature casts doubt on its link with the interstitial carbon C_i. Indeed this defect is known to be mobile at room temperature [97]. To further study the effect of temperature on the SD-2 defect, the evolution of its photoluminescence signal with optical power was recorded at several temperatures (figure 2.24(a)). The saturation curves display a strong decrease in intensity with increasing temperatures. The parameters P_{sat} and S_{sat} for each temperature are extracted via a fit with equation 2.5 and their values are displayed in figures 2.24(b) and (c). This analysis reveals that the saturation power P_{sat} increases exponentially with temperature, while the maximum intensity decays above 30 K. The evolution of P_{sat} and S_{sat} are well described by a thermal activation model given by the equations [39]:

$$P_{\text{sat}}(t) = a + be^{-\frac{E_a}{k_b T}} \tag{2.10}$$

$$S_{\text{sat}}(t) = \frac{a'}{1 + b'e^{-\frac{E'_a}{k_b T}}} \tag{2.11}$$

where a, a', b, b' are free constants, k_b the Boltzmann constant and E_a, E'_a activation energies. The data recorded on the SD-2 defect indicate two activation energies $E_a = 25(1)$ meV and $E'_a = 24(3)$ meV with similar values, suggesting that a common energy activated process induces both evolution. The fast decrease of S_{sat} with temperature is in stark contrast with the behavior of the SD-0 defect, for which S_{sat} remained constant up to 120 K (see figure 2.11). These two phenomena indicate that there can be multiple processes at the origin of the photoluminescence decline at higher temperatures.

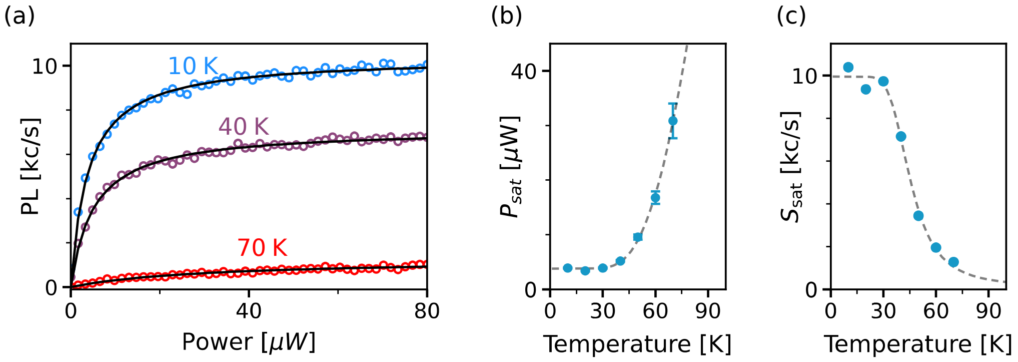

Figure 2.24: Evolution of the saturation curves with temperature for the SD-2 defects. **(a)** Saturation curves measured on a single defect for different temperatures. Data are fitted with equation 2.5 to extract the saturation power P_{sat} and saturation signal S_{sat}. **(b, c)** Evolution of P_{sat} and S_{sat} with temperature. The data are fitted with the functions of equation 2.10 and 2.11 respectively to extract energies $E_a = 25(1)$ meV and $E'_a = 24(3)$ meV.

Excited-level lifetimes

To characterize the dynamics of relaxation of the individual single-photon emitters, we performed time-resolved photoluminescence measurements under a 532 nm pulsed excitation. The luminescence decay recorded on single defects belonging to each family are shown in figure 2.25. For the four families SD-1 to SD-4, we observe a mono-exponential decay providing a single excited-level lifetime ranging between 14 ns to 30 ns. On the contrary, families SD-5 and SD-6 feature a bi-exponential decay, with a short lifetime roughly at 5 ns and a long one around 19 ns

Family	SD-0	SD-1	SD-2	SD-3	SD-4	SD-5	SD-6
PL intensity at saturation [kc/s]	16	13	9	8	14	22	10
Resistant to thermal cycles	Yes	Yes	Yes	Yes	Yes	No	Yes
Number of emission dipoles	1	1	1	1	1	1	1
ES lifetime(s) [ns]	36(4)	14.4(4)	30.6(5)	30(1)	26(1)	4.4(7) 19(5)	6.7(8) 35(4)

Table 2.2: Summary of the luminescence properties for the different families of single defects.

and 35 ns respectively. The exact values for each family are given in table 2.2. The observation of a bi-exponential decay indicates a more complex dynamics of emission, which could be caused by multiple excited levels. Unfortunately at this point it is not possible to conclude on the exact origin of this behavior. Still, all these lifetimes are orders of magnitude shorter than the ones measured on other defects in silicon, such as erbium dopants [92] or T-centers [36]. Consequently, these defects are already advantageous to develop bright silicon-based single-photon sources even without relying on photoluminescence enhancement by the Purcell-effect in silicon microstructures [101].

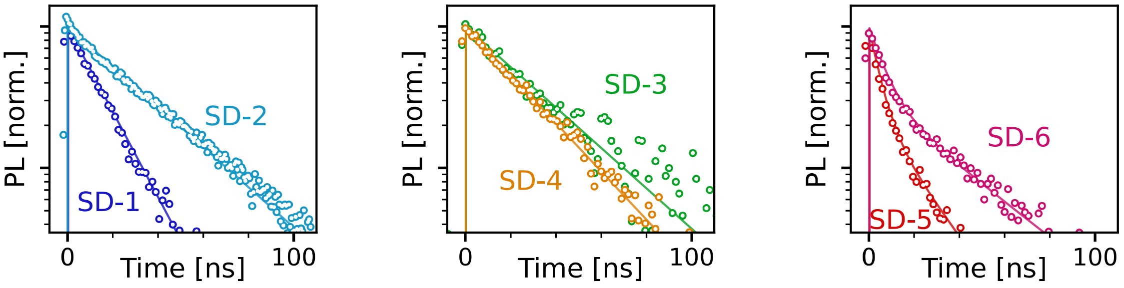

Figure 2.25: Time-resolved photoluminescence decay recorded on each family under 50 ps pulse excitation at 532 nm. The excited level lifetimes are extracted by fitting the data with a single exponential function (solid line) for families SD-1 to SD-4 and a bi-exponential for families SD-5 and SD-6 to extract two lifetimes.

2.3.3 Emission polarization diagrams

To characterize the emission dipoles of each defect, the polarization of their emitted photons were analysed. The resulting emission polarization diagram for one defect of each family is plotted in figure 2.26(a), showing that all the defects exhibit a linearly polarized emission, corresponding to a single emission dipole. The orientation of the projected dipole for defects SD-1 and SD-4 with respect to the crystal axis [1 1 0] indicates that these emitters cannot possess a dipole along a ⟨1 1 1⟩ direction. For the SD-2 defect, the dipole orientation angle can vary from one defect to another, but the data set is insufficient to provide statistically relevant distributions over the dipole angles. These observations prompt the need for further investigation on the single defects, which could help to identify their microscopic structure thanks to the dipole orientations.

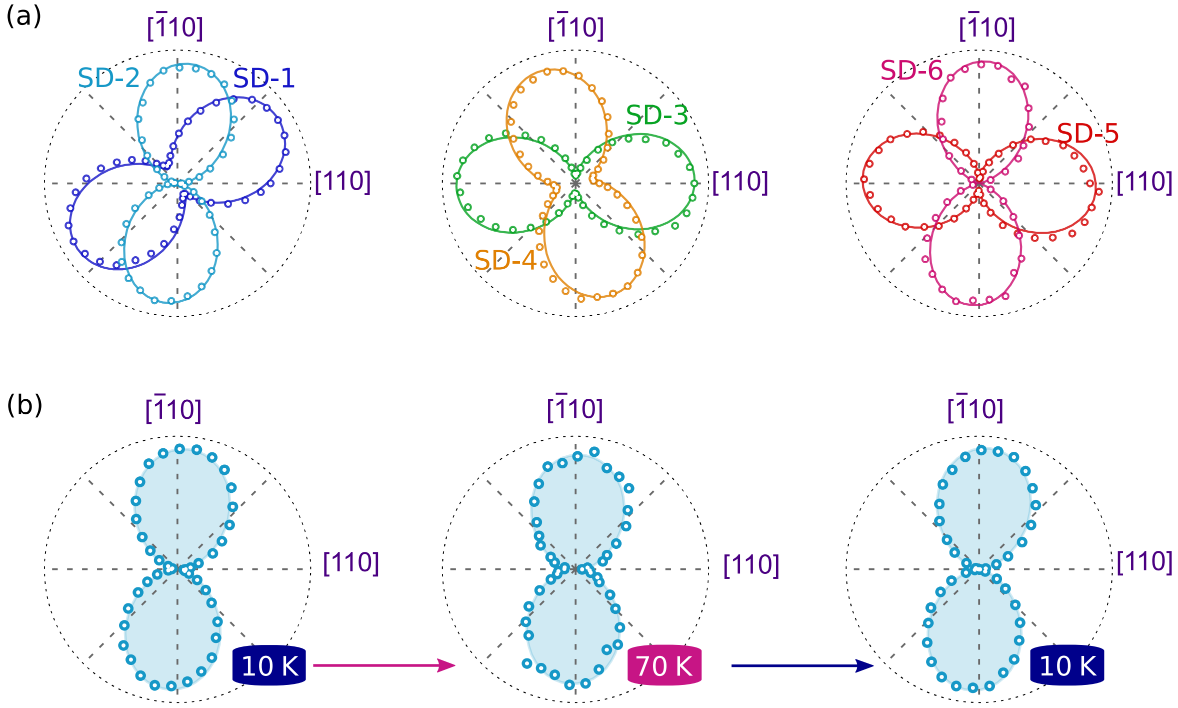

Figure 2.26: **(a)** Emission polarization diagram measured on single defects from all families. The photoluminescence signal is corrected from background counts. **(b)** Emission diagram measured at different temperatures on a single SD-2 center.

If the SD-2 defects would correspond to interstitial carbons, which are mobile at room temperature, their displacement over a few nanometers would not necessarily be detected in the photoluminescence scans. An alternative way to probe such displacements is to look for change in the emission dipole orientation with temperature. Figure 2.26(b) displays the emission polarization diagram of a single SD-2 defect taken at 10 K, then 70 K and finally 10 K again. The change in temperature do not lead to any visible change in the polarization diagram. A study of several SD-2 defects after heating to 300 K then cooling again displayed no change in dipole orientation either. These observations suggest that SD-2 is either not related to the interstitial carbon defect, or that local strain might help to stabilize its orientation.

2.4 Conclusion

In this chapter, we have demonstrated the first isolation of single fluorescent defects in silicon. This result was achieved by the development of a low temperature confocal microscope optimized for the detection of single emitters in the near infrared domain. In addition to this first emitter labeled SD-0, further investigations have lead to the isolation at the single defect scale of 7 families of optically active point defects in total. These individual emitters provide a wide diversity of bright, linearly polarized single-photon emission in the near-infrared range, some even matching the telecom O-band. We have further demonstrated that some single defects exhibit additional appealing properties such as a small spread of the ZPL wavelength, or a strong photoluminescence intensity well above the liquid-nitrogen temperature. It should be noted that this isolation of single defects in silicon has been replicated later by another group [102], thus confirming the reproducibility of our observations.

A current limitation to the use of these defects for quantum technologies is that their microscopic nature is currently unknown, and that no efficient process is established to selectively create these defects. No theoretical support is possible as long as the microscopic structure is not identified, evidencing the need for further work, both experimental and theoretical. In the next chapter, we will focus our study on two defects with a well established microscopic structure: the G-center and the W-center of silicon.

Chapter

3

Isolation of single G- an W-centers in silicon

Contents

Introduction

In this last chapter, we focus our study on two well-known defects in silicon: the G-center and the W-center, which both exhibit appealing properties for future applications in quantum technologies. The G-center is a two-carbon complex interacting with a silicon interstitial atom. It is characterized by a sharp emission line at 1280 nm matching the optical telecommunications O-band. In addition, the G-center has a spin-triplet metastable level, which was detected through optical detection of the magnetic resonance in the early 80s [40, 41], and could be used as an additional quantum resource. The W-center of silicon, which is formed by three self-interstitial silicon atoms, features an emission line at 1218 nm, and can be created without the incorporation of extrinsic impurities in the silicon matrix. Ensemble measurements have shown that these two defects exhibit an excited level lifetime below 40 ns [39, 103], which suggests that they can be bright enough to be observed at the single scale with our experimental setup.

In order to study these defects at the single scale, a first challenge is to create them deterministically by applying a controlled ion implantation process. Since our long-term objective is to use these defects for quantum technologies, we have chosen to perform this study in a silicon sample isotopically purified with ^{28}Si (99.992%). Such an isotopic purification is known to improve drastically the optical properties of luminescent defects, by reducing the inhomogeneous broadening of the emission lines [104]. In addition, the spin coherence properties of point defects can be greatly improved through isotopic purification by decreasing the fluctuations of the nuclear spin bath [15, 105]. All the experiments presented in this chapter have thus been realized with a SOI wafer, whose top silicon layer has been purified with ^{28}Si, as sketched in figure 3.1(a). This wafer has been grown at CEA Leti and is provided by our collaborator Jean-Michel Gérard. Here the top layer of a commercial SOI wafer was first reduced to 4 nm by thermal oxidation, followed by wet hydrofluoric acid chemical etching. A layer of ^{28}Si was then grown by chemical vapor deposition (CVD) leading to a top silicon layer of 60 nm thickness. The SOI top layer is separated from the rest of the silicon substrate by a 145 nm-thick silicon dioxide (SiO_2) layer. Starting from this quantum grade material, an ion implantation protocol was optimized during my PhD to produce single G- and W-centers in the top silicon layer.

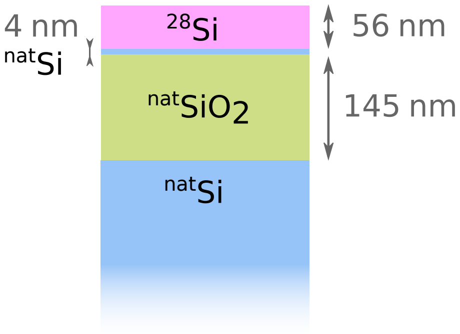

Figure 3.1: Silicon-on-insulator (SOI) whose top layer is isotopically purified with ^{28}Si.

In the first section of this chapter, we will focus on the G-center of silicon (**§3.1**). After an overview of its main properties, we will first describe an implantation procedure allowing for its detection at the single scale. We will then study its intrinsic photophysical properties. In particular, we will show that the analysis of the polarization of the single photon emission and of the fine structure observed in photoluminescence spectra reveal a rotational reorientation of the G-center around its crystalline axis, whose dynamics vary from one defect to another. The second section will be devoted to the detection of single W-centers (**§3.2**) created through the implantation of Si ions. The spectroscopy and photon emission study of these individual defects will reveal new physical properties of this common radiation damage center in silicon, such as its dipolar emission and coupling to its environment.

3.1 Detection of single G-centers in silicon

Carbon has historically been a major contaminant in manufactured silicon. As a result, carbon-based fluorescent centers in silicon have been extensively studied during the twentieth century [35]. Out of the 14 known fluorescent defects linked to this impurity, the G-center is one of the most frequent and by far the most studied defect (see annex A for the detailed history of the experimental studies on the G-center in silicon). As sketched in figure 3.2(a), it consists of an interstitial silicon atom bridging two adjacent substitutional carbon atoms. The G-center is mainly identified by its spectral properties featuring a strong emission/absorption line at $\approx 1280\,\text{nm}$ (0.97 eV). Importantly, the G-center can be created in silicon by using several methods, including electron irradiation [104] and carbon implantation followed by proton irradiation [39]. This latter method was used for the study of large ensembles of G-centers during the PhD of Walid Redjem and Clément Beaufils in our research group. This work enabled the first measurement of the G-center excited level lifetime $\tau_e = 5.9\,\text{ns}$ [39]. Up to now, this defect has been mostly investigated for its use in optoelectronics applications, for example as a source of emission in a LED via electrical injection [106, 107]. Optical gain and stimulated emission have also been reported, opening prospects for the development of lasers based on G-centers in silicon [108].

The G-center also exhibits some appealing features for quantum technologies. First its optical emission at 1280 nm lies within the telecom O-band, which is suitable for long-distance communication via optical fibers. Secondly, the defect possesses a spin triplet metastable level, which has been detected through optically detected magnetic resonance in the 80s [40, 41]. This property suggests that the electron spin of the G-center could be used as a solid-state spin qubit using similar tools as the one commonly implemented nowadays to detect electron spins in solid-state systems by optical means. Toward this challenging objective, a first step is to demonstrate the optical isolation of an individual G-center. This is the purpose of this section.

We will start by presenting the microscopic structure and the spectral signature of the G-center in silicon. We will then demonstrate its detection at the single defect scale, which enables us to investigate its intrinsic photophysical properties. In particular, we will investigate the impact of the rotational reorientation of the G-center on (i) the polarization properties of its emission and on (ii) the fine structure of its photoluminescence spectra.

3.1.1 Overview of the G-center in silicon

Microscopic structure

Despite many studies, the G-center microscopic structure has long been debated. Since the first model proposed in 1983 [41], theoretical works have struggled to identify the exact atomic structure of the defect [109–111]. Very recently, the microscopic structure of the optically active form of the G-center has been definitively confirmed by studying the fine structure of the optical emission in isotopically purified silicon samples [104, 112]. As sketched in figure 3.2(a), the G-center consists of two substitutional carbon atoms bridging one interstitial silicon atom which

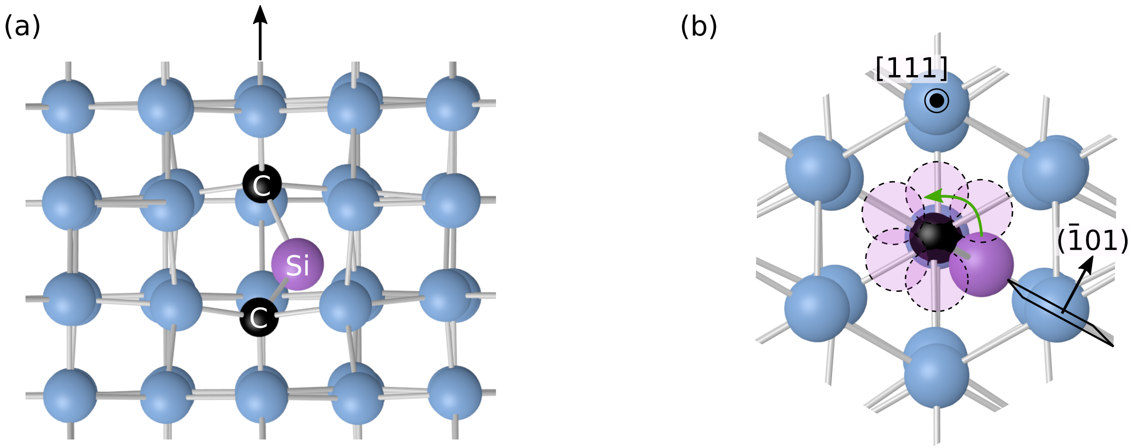

Figure 3.2: The G-center in silicon **(a)** Atomic structure of the G-center consisting of an interstitial silicon atom (purple) bridging two adjacent carbon atoms (black). **(b)** Same atomic structure seen from the [1 1 1] direction. The two carbon atoms lie in the middle along the [1 1 1] axis. The three carbon and silicon atoms form a $(\bar{1}\,0\,1)$ plane. The interstitial silicon atom (purple) is moving between 6 equivalent sites (dashed purple circles).

is pushed off-center. The two carbon atoms are lying along a [1 1 1] direction, and form a plane $(\bar{1}\,0\,1)$ with the third silicon interstitial atom (figure 3.2(b)). In this configuration, the defect is characterized by a monoclinic C_{1h} symmetry.

A remarkable feature of the G-center is that the interstitial silicon atom can rotate around the [1 1 1] axis. As depicted in figure 3.2(b), it can move between six positions separated by a low energy barrier [112]. These six positions are almost equivalent from the point of view of the silicon atom, and are each separated by an angle of $\pi/3$ in the (1 1 1) plane. When the temperature is increased, a motional averaging over these six possible positions of the silicon atom leads to a defect with C_{3v} symmetry around the [1 1 1] axis. Such a trigonal symmetry was confirmed both in optically detected magnetic resonance studies [41] and in electron paramagnetic resonance measurements [113]. Considering a perfect silicon lattice under zero strain, the six positions become perfectly equivalent, which then leads to modifications of the luminescence spectrum, as will be discussed in the next section.

Photoluminescence spectrum

The G-center in silicon is identified by a well-defined photoluminescence spectrum. A typical emission spectrum recorded from an ensemble of G-centers created by carbon implantation and proton irradiation is shown in figure 3.3. This sample is very similar to the one that has been previously used in our research group to analyze the optical properties of dense ensembles of G-centers [39]. The two signatures of the G-center emission are (i) a sharp zero-phonon line (ZPL) at 1279.9 nm (969.4 meV) [104] and (ii) a weak emission peak at 1381 nm, which is called the E-line, and is associated with a local vibration mode at 72 meV [114]. Most of the spectrum including the ZPL and a large part of the phonon sideband lies within the telecom O-band,

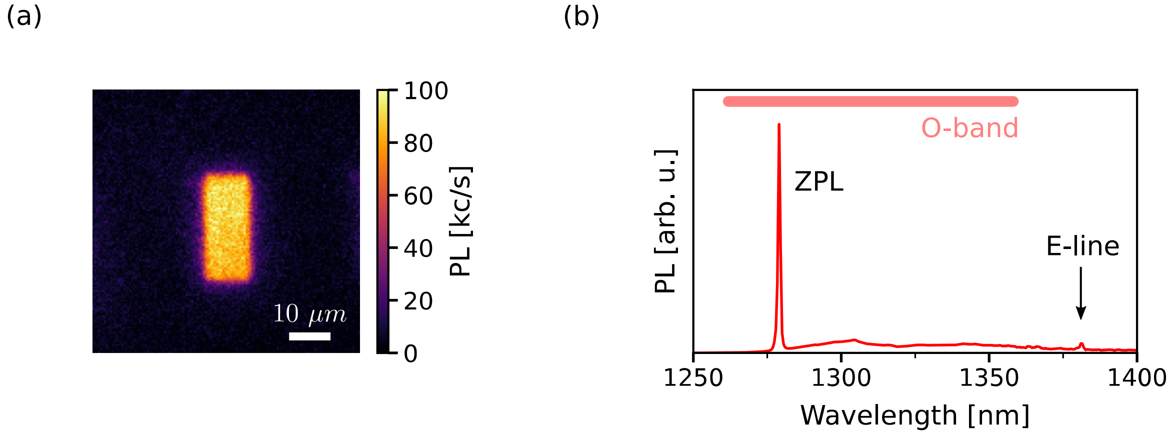

Figure 3.3: The G-center luminescence spectrum. **(a)** Optical scan recorded on a silicon sample implanted through a rectangular aperture with carbon ions ($5 \times 10^{13}\,\mathrm{cm}^{-2}$ - 36 keV) and irradiated with protons ($3 \times 10^{14}\,\mathrm{cm}^{-2}$ - 2.25 MeV) to create dense ensembles of G-centers. **(b)** Photoluminescence spectrum recorded from an ensemble of G-center, showing a strong zero-phonon line at 1280 nm and a weak emission peak at 1381 nm, which is commonly referred to as the E-line and corresponds to a local vibration mode [114].

spanning from 1260 to 1360 nm.

Fine-structure of the G-centers zero-phonon line

The G-center photoluminescence is induced by a transition between two spin singlet levels ($S = 0$), as revealed by the absence of ZPL splitting under a large magnetic field [114]. Furthermore, when the G-center is not rotating, the optical transition occurs between two orbital singlets [112]. From this simple spin singlet - orbital singlet configuration, one could expect a single line in the luminescence spectrum. Nevertheless, a fine structure was recently observed in very high resolution spectra of G-ensembles created by electron irradiation in an ultrapure silicon sample from the Avogadro project [104,115]. To circumvent spectral broadening induced by the mixture of silicon isotopes in the natural material (92.23 % ^{28}Si, 4.67 % ^{29}Si, 3.10 % ^{30}Si [116]), the sample used in this study was isotopically purified with ^{28}Si (99.995 %). In addition the sample was fixed in a strain-free manner. The observed fine structure of the optical emission, which is reproduced in figure 3.4(a), is a direct consequence of the G-center rotation near zero temperature [112]. As the energy barrier between the six positions of the interstitial silicon atom is small, the defect can tunnel between the six sites faster than the excited level lifetime, leading to a motional averaging of the defect emission. In fact, the rotational reorientation of the defect can be described with the Schrödinger equation applied to an effective particle confined in a one-dimensional periodic potential. In the limit of low temperature, Péter Udvarhekyi and colleagues have recently shown that the sixfold degeneracy is partially lifted into a quartet structure with $1:2:2:1$ degeneracy and with an energy splitting $\delta : 2\delta : \delta$, where δ corresponds to the tunneling rate through a single barrier [112]. This model is in perfect agreement with

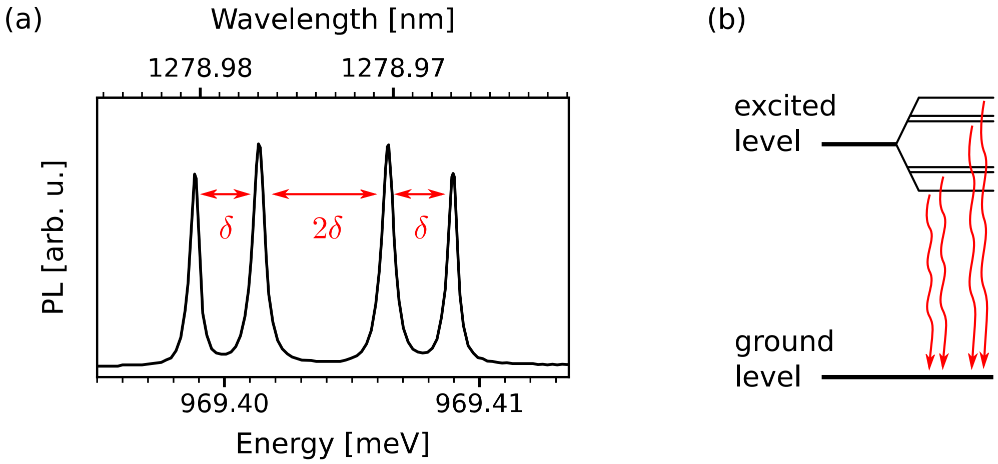

Figure 3.4: Fine structure of the G-centers zero-phonon line. **(a)** Photoluminescence spectrum taken from [104] of an ensemble of G-centers in ^{28}Si at 1.7 K, showing a fine structure in the zero-phonon line. **(b)** Schematics of the ground and excited level structure of the G-center. The rotation of the interstitial silicon atom leads to 6 energy levels, resulting in a quartet structure in the absorption and emission spectra.

the observed fine structure of the ZPL emission. As illustrated in figure 3.4(b), the splitting is only due to the excited level, as the ground level splitting is negligible owing to a much larger energy barrier [112]. It should be noted that the two central lines are not twice as high in the photoluminescence spectrum because of a stronger reabsorption of the G-center photons for these two peaks. The absorption spectrum, however, was observed to have the 1 : 2 : 2 : 1 ratios in amplitudes [104].

Up to now all the study on the G-center have been performed at the ensemble level. We will now show that this defect can be isolated at the single level. We will then study the impact of the rotational reorientation of the defect on (i) the polarization properties of its emission and on (ii) the fine structure of photoluminescence spectra at the single defect scale.

3.1.2 Creation of single G-centers by ion implantation

The creation of dense ensembles of G-centers can be done by implantation with carbon ions followed by irradiation with protons [39]. To obtain single isolated defects, a natural method is to apply the same process while simply reducing gradually the implantation doses. In this section, we will show that individual G-centers can be obtained by following this simple method.

It should be noted that all the measurements presented in this section were recorded with two superconducting nanowire single-photon detectors (Single Quantum Eos) that were purchased during the last year of my PhD. These detectors feature a quantum efficiency up to 80 % at 1.3 µm, whereas the previous detectors were limited to 10 % at the same wavelength.

As mentioned in the introduction of this chapter, we rely on a SOI wafer with a 60-nm-thick top silicon layer purified with silicon-28 (see figure 2.1(a)). All experiments are performed on silicon samples cut from the same wafer.

Preliminary control experiments

Before performing any ion implantation, the optical properties of the virgin sample were analyzed in order to check that no native G-centers were present in the sample. An optical scan recorded on the virgin sample is displayed in figure 3.5(a). It reveals a uniform background luminescence signal, without defects. Still, a careful analysis shows the presence of a few localized spots of emission. A systematic study of their emission spectra reveals that they are mostly structure-less, as illustrated by a typical photoluminescence spectrum shown in figure 3.5(c). We thus conclude that no native G-centers are present in our silicon sample before implantation.

We also analyzed another sample, which only underwent a flash annealing at 1000 °C during 20 s. A luminescence scan recorded on this sample is shown in figure 3.5(b). This control experiment indicates that flash annealing results in an overall reduction of the luminescence background. Isolated emission spots can then be observed more easily. Their emission spectra are similar to the one shown in figure 3.5(c), which do not correspond to the G-center. We can therefore conclude that flash annealing alone cannot create G-centers by stabilizing residual carbon impurities hosted in the silicon sample.

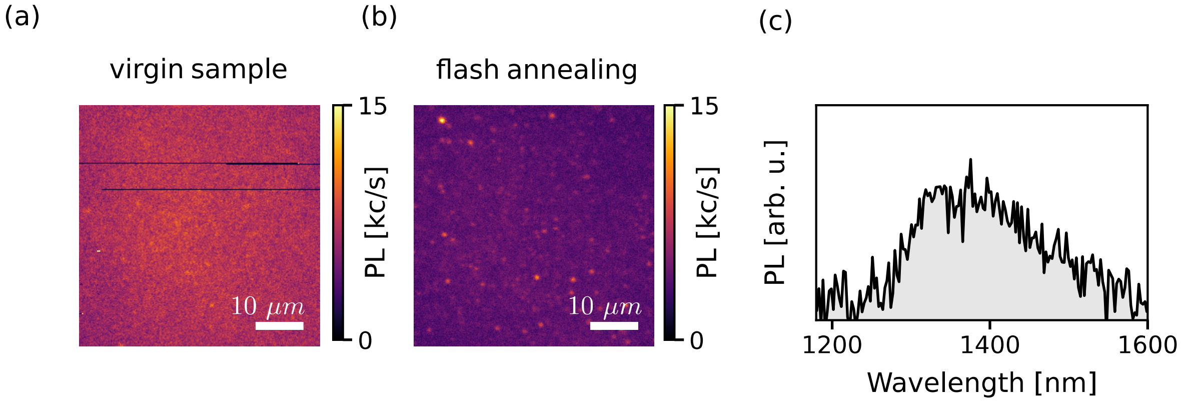

Figure 3.5: (a,b) Optical scan recorded (a) on a virgin silicon sample and (b) after a flash annealing at 1000 °C during 20 s. **(c)** Typical photoluminescence spectrum recorded from a localized spot of emission.

Cross-implantation with carbon and protons

Once these verifications done, a sample cut from the same SOI wafer was cross-implanted through a rectangular aperture with carbon ions and protons, by our collaborators Tobias Herzig and Sebastien Pezzagna from the University of Leipzig (Germany). The geometry of the cross-implantation is sketched in figure 3.6(a). It consists of well-defined rectangular patterns of carbon implantation with 7 fluences from $3 \times 10^{13}\,\mathrm{cm}^{-2}$ down to $3 \times 10^{10}\,\mathrm{cm}^{-2}$ and an energy of 8 keV. This energy was chosen so that the carbon atoms stay mostly within the 60 nm-thick top silicon layer. After carbon implantation, a flash annealing at 1000 °C during 20 s was performed to repair the silicon lattice from damage resulting from the carbon implantation. As a third step, a proton irradiation with 7 fluences, from $3 \times 10^{13}\,\mathrm{cm}^{-2}$ down to $3 \times 10^{10}\,\mathrm{cm}^{-2}$ was performed with the rectangularly shaped implantation mask rotated by 90°. This proton irradiation is used to activate the creation of G-centers.

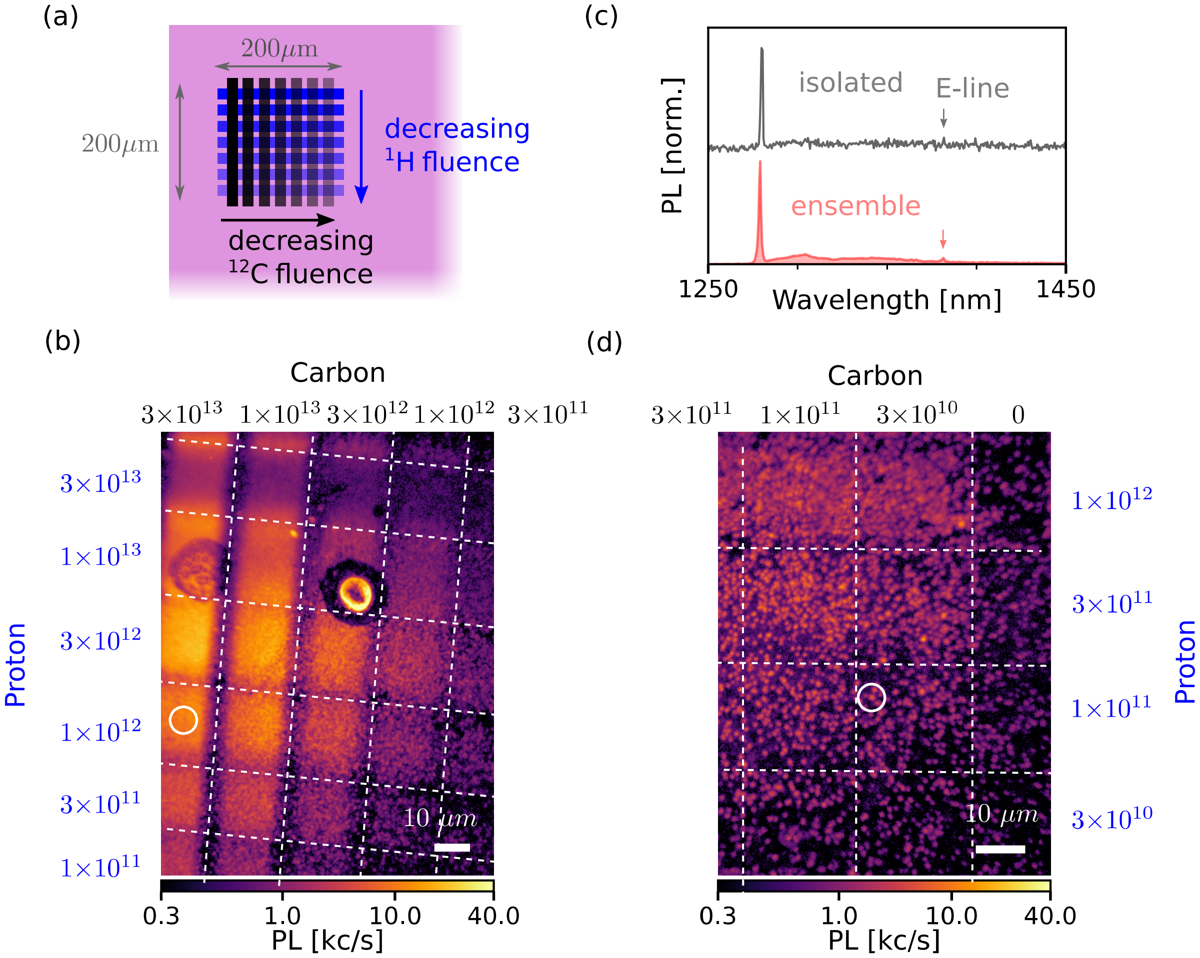

Figure 3.6: Creation of G-centers via cross-implantation with carbon and hydrogen **(a)** Sketch of the implantation map of the silicon sample. The rectangular bands are 20 µm by 200 µm large and separated by 10 µm. Carbon implantation at 8 keV and a proton irradiation at 6 keV are done with seven decreasing fluences ranging from $3 \times 10^{13}\,\mathrm{cm}^{-2}$ down to $3 \times 10^{10}\,\mathrm{cm}^{-2}$. **(b, d)** Photoluminescence scan of the cross-implanted region. The implanted squared are separated by dashed lines and the value of the implantation doses are expressed in cm^{-2}. A non-linear color scale is used for the luminescence signal to better visualize the regions implanted with high and low doses. **(c)** Photoluminescence spectra recorded at the positions marked with the circles in (b) and (d), corresponding to a dense ensemble of G-centers and to a well-isolated G-center, respectively.

An optical scan recorded on the cross-implanted regions (figure 3.6(b)) shows the presence of a high luminescence signal produced by dense ensembles of defects. The acquisition of photoluminescence spectra unambiguously indicates that these dense ensembles correspond to G-centers, with a characteristic zero-phonon line at 1280 nm and the E-line at 1381 nm (see figure 3.6(c)). Both the carbon and the proton doses affect the creation of G-centers. The effect of the carbon dose can be visualized through the variation of the luminescence signal along the horizontal direction in figure 3.6(b). We observe a monotone increase of the G-center density with the carbon implantation dose. The variation of the signal along the vertical axis, which is linked to the proton irradiation dose, displays a more complex behavior. While the luminescence increases up to a proton dose of $3 \times 10^{12}\,\mathrm{cm}^{-2}$, larger doses then lead to a decrease of the G-center luminescence. This observation might be explained by considering that the G-center is converted into a non-fluorescent form through high irradiation doses. An in-depth study of this effect is going beyond the scope of this thesis.

As the objective is to isolate single G-centers, the weakly implanted regions with a sparse level of emitters are then investigated (figure 3.6(d)). For low implantation doses, isolated emitters are indeed present in the sample. These emitters correspond to G-centers, as revealed by their photoluminescence spectra (figure 3.6(c)). By adjusting the dose of carbon implantation and proton irradiation, it is thus possible to create individual G-centers in silicon.

Detection of single G-centers far from the implanted areas

Surprisingly, an important density of emitter is also present far away from the implanted areas, as illustrated by the optical scan shown in figure 3.7(a). This scan, recorded 200 μm away from the implanted zone, exhibits 121 isolated emitters, which corresponds to a density of $\approx 0.3\,\mu\mathrm{m}^{-2}$. An analysis of their photoluminescence spectra reveals that all emitters correspond to G-centers, as confirmed by the presence of the E-line in their emission spectra (figure 3.7(b)).

To demonstrate that the emission originates from single defects, a measurement of the second-order autocorrelation function $g^{(2)}(\tau)$ is performed (figure 3.7(c)). The recorded data show a clear antibunching effect at zero-delay $g^{(2)}(0) \approx 0.2$, thus confirming the isolation of a single G-center. To verify the single-photon purity, the background-corrected $g^{(2)}_{\mathrm{corr}}(\tau)$ function is computed by following the procedure described in § 2.2.1 and considering a signal-to-noise ratio SNR ≈ 10. Once corrected, the antibunching dip goes to zero.

The observation of single G-centers far from the implanted area is unexpected, as the virgin sample did not exhibit any G-centers (see figure 3.5), and as only a local implantation through a rectangular microaperture was performed. Our first hypothesis was that the carbon could have diffused during the flash annealing step, as the interstitial carbons in silicon are known to be highly mobile at elevated temperatures [35]. To check this hypothesis, we investigate a reference sample for which only a cross implantation was performed, without flash annealing. An optical scan recorded on this sample far away from the implantation area is shown in figure 3.8(a). It reveals that without the flash annealing process, a large number of unresolved emitters are present in the sample far from the implanted areas. The average luminescence of this scan $S_{\mathrm{avg}} \approx 12\,\mathrm{kc/s}$ is even above the maximum luminescence measured after the flash annealing in

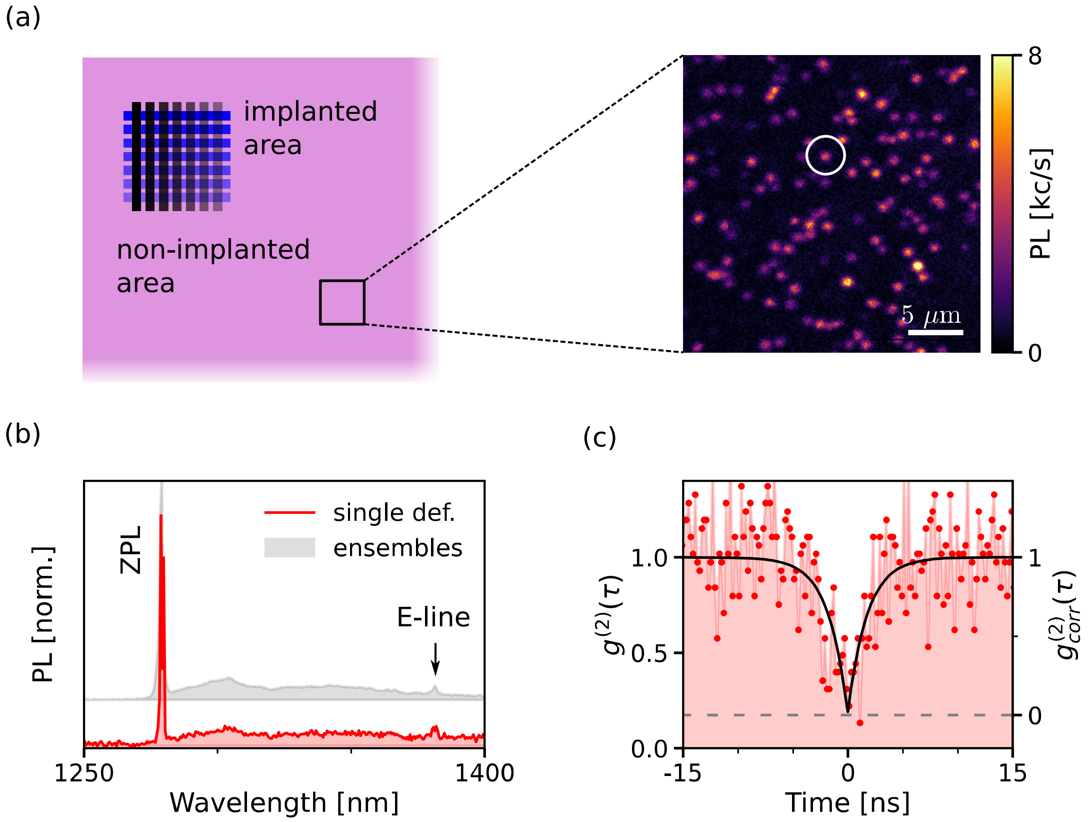

Figure 3.7: Detection of single G-centers in silicon. **(a)** Photoluminescence scan recorded 200 μm away from the implanted area. All luminescence spots correspond to the emission of single G-centers. **(b)** Photoluminescence spectrum of the single G-center circled in (a). The spectrum recorded on a dense ensemble is reproduced in grey. The spectra are normalized by their maximum intensity. **(c)** Measurement of the second-order correlation function $g^{(2)}(\tau)$ for the same G-centre. The left axis shows the raw data, while the right axis indicates the background-corrected $g^{(2)}_{corr}(\tau)$ function obtained with equation 2.4 for a signal-to-noise ratio SNR = 10.

figure 3.7(a). A spectral analysis (figure 3.8(b)) indicates mostly the presence of G-centers, as well as a weak emission line corresponding to the W-centers of silicon, which is characterized by a ZPL at 1218 nm (cf. § 3.2). This measurement demonstrates that the creation of these G-centers solely results from the implantation procedure. In fact, the high temperature flash annealing only reduces the luminescence background by destroying most of the unstable defects, in agreement with the previously reported annealing kinetics of the G-center [117].

The origin of the single G-centers observed far from the implantation areas is still not understood. One hypothesis is that the interstitial carbons, which are still mobile at room temperature, have diffused over large distances. However, the diffusion coefficient of the interstitial carbons at room temperature $D = 0.28\,\mu\mathrm{m}^2/\mathrm{month}$ [118] seems much too low to explain their presence far from the implanted area. Another possibility is that a small fraction of the implantation ions are going through the implantation mask, a 9-μm-thick piece of mica. Such an effect

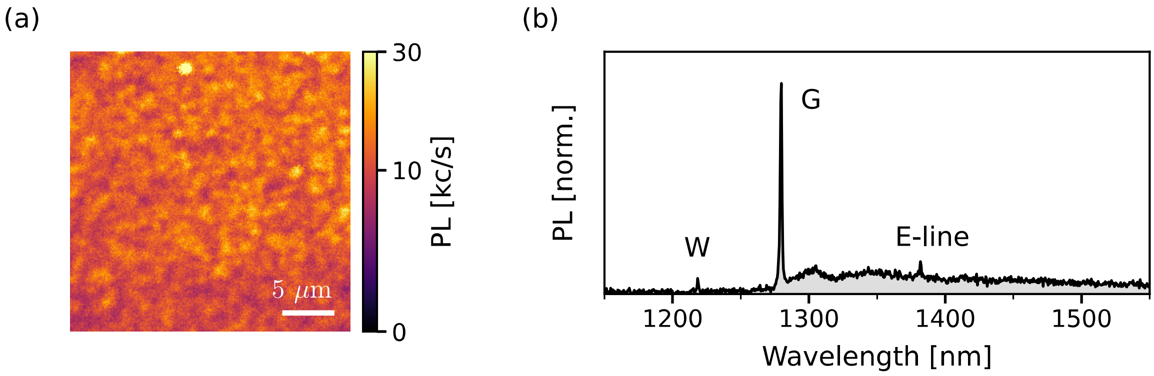

Figure 3.8: (a) Optical scan recorded on a sample for which only a cross implantation was performed without flash annealing. The scan is recorded far away from the implanted areas. **(b)** Typical photoluminescence spectrum recorded on this sample.

is very unlikely given the low implantation energy used in this work. A third hypothesis is that the sample gets electrically charged during the implantation, leading to a strong deviation of the ion beam. Further work will be required to better understand the creation process of these defects.

Despite several remaining questions, the measurements shown in figure 3.7 demonstrate the first isolation of a single G-center in silicon. This isolation enables us to study the G-center photophysics at the single defect scale.

Single G-center photophysics

Single G-centers are perfectly photostable, as demonstrated by the photoluminescence time trace shown in figure 3.9(a). To quantify the single-photon emission efficiency, a saturation curve was recorded by sweeping the excitation laser power (figure 3.9(b)). The G-center exhibits a standard saturating behavior. Data fitting with equation 2.5 (cf. § 2.2.2) leads to a saturation power $P_{sat} = 2.63(2)\,\mu\mathrm{W}$ and a saturated detection rate $S_{\mathrm{sat}} = 6.28(2)\,\mathrm{kc/s}$. Surprisingly, this maximum counting rate is much lower than the one obtained for single SD-0 defects in the previous chapter. When considering the increase by a factor of ≈ 8 of the detector's quantum efficiency, this experiment reveals that the G-center emission is about one order of magnitude dimmer than the SD-0 defect.

To investigate this strong difference in emission intensity, the exited level lifetime τ_e of the single defect is recorded using a pulsed laser excitation with a 50-ps pulse duration. The recorded decay, displayed in figure 3.9(c), is well fitted by a monoexponential function, resulting in a lifetime τ_e =4.12(1) ns. This value is not far from the reported value of 5.9 ns for ensembles of G-centers [39]. The reduction of the lifetime could be linked to the local environment of the defect, as was observed for NV centers in diamond [55], and seems to be common for defects in silicon. We will see in §3.2.4 that the W-center of silicon displays an even larger variation of its excited level lifetime, with fluctuations around one order of magnitude.

The low luminescence signal of the G-center compared to the SD-0 defect, as well as its shorter lifetime ($\approx 35\,\text{ns}$ for SD-0), indicate that the quantum efficiency of the G-center is much smaller, likely around $\approx 1\,\%$. Further study will be necessary to understand which processes limit the G-defect quantum efficiency.

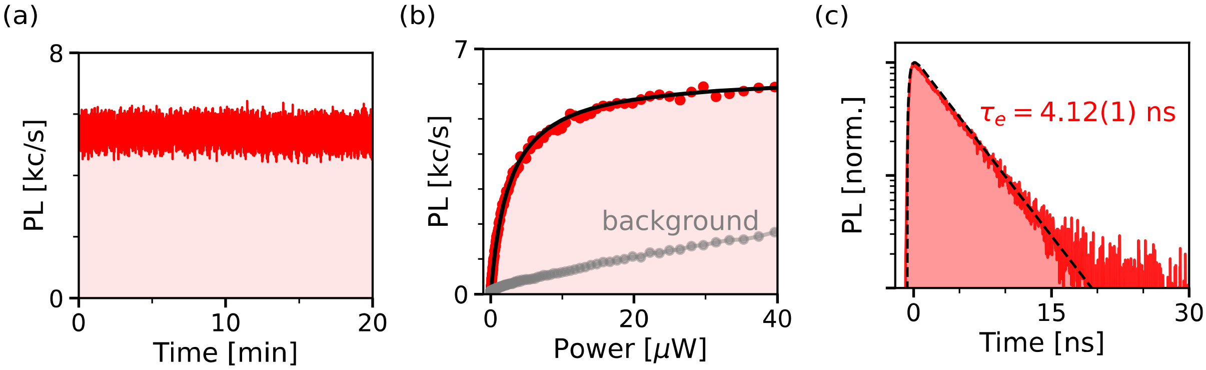

Figure 3.9: Photostability of single G-centers. **(a)** Typical photoluminescence time-trace measured at $10\,\mu\text{W}$ on a single defect. **(b)** Standard photoluminescence saturation curve recorded on an individual G-defect. **(c)** Time resolved photoluminescence decay (in semi-log scale) of a single G-center recorded under optical excitation with 50 ps laser pulses at 532 nm. The data are fitted with a single exponential function to extract the excited level lifetime τ_e.

3.1.3 Evidence of the rotation of single defects

Measurements on ensembles of G-centers have shown that the defect can rotate around its $\langle 1\,1\,1 \rangle$ axis, with the interstitial silicon atom jumping between 6 equivalent positions. By analysing the emission polarization diagram of single G-centers, as well as the fine structure of their zero-phonon line, we will now show that this rotational reorientation is also observed at the single defect scale.

Emission dipoles

To characterize the polarization of the photons emitted by the single G-centers, a half-wave plate and a polarizer were installed in front of the single-photon detectors. A polarization diagram was then recorded by monitoring the photoluminescence signal while rotating the half-wave plate. The polarization diagrams recorded on two typical G-centers are shown in figures 3.10(a) and (b). The analysis of these diagrams reveals two remarkable properties. First, the single defect emission is not perfectly modulated. This observation indicates that the single photon emission is not linearly polarized, which suggests the presence of multiple emission dipoles. Secondly, the principal polarization direction of the emission, shown by an arrow in figures 3.10(a) and (b), is oriented, either along the $[1\,1\,0]$ or $[\bar{1}\,1\,0]$ silicon crystal axis. A statistical analysis over 14 G-centers is performed by fitting the luminescence rate $S(\theta)$ recorded while rotating the polarization angle θ with the equation:

$$S(\theta) = S_{\max}[V cos^2(\theta - \phi) + (1 - V)]. \tag{3.1}$$

In this equation, $S_{\max}$ denotes the maximum luminescence rate, ϕ the angle of the main polarization direction of the emission with respect to the $[1\,1\,0]$ crystal axis, and V is the visibility of the modulation . This visibility is defined as $V = (S_{\max} - S_{\min})/S_{\max}$ where $S_{\min}$ is the minimum luminescence signal. The histograms of ϕ and V obtained from the analysis of the polarization diagrams of a set of 14 single emitters are plotted in figures 3.10(c) and (d). This analysis clearly shows that the main polarization direction is always found either along the $[1\,1\,0]$ or $[\bar{1}\,1\,0]$ axis, with a roughly equal distribution between these two directions. The visibility V on the other hand vary from center to center, but is never found above $\approx 70\,\%$.

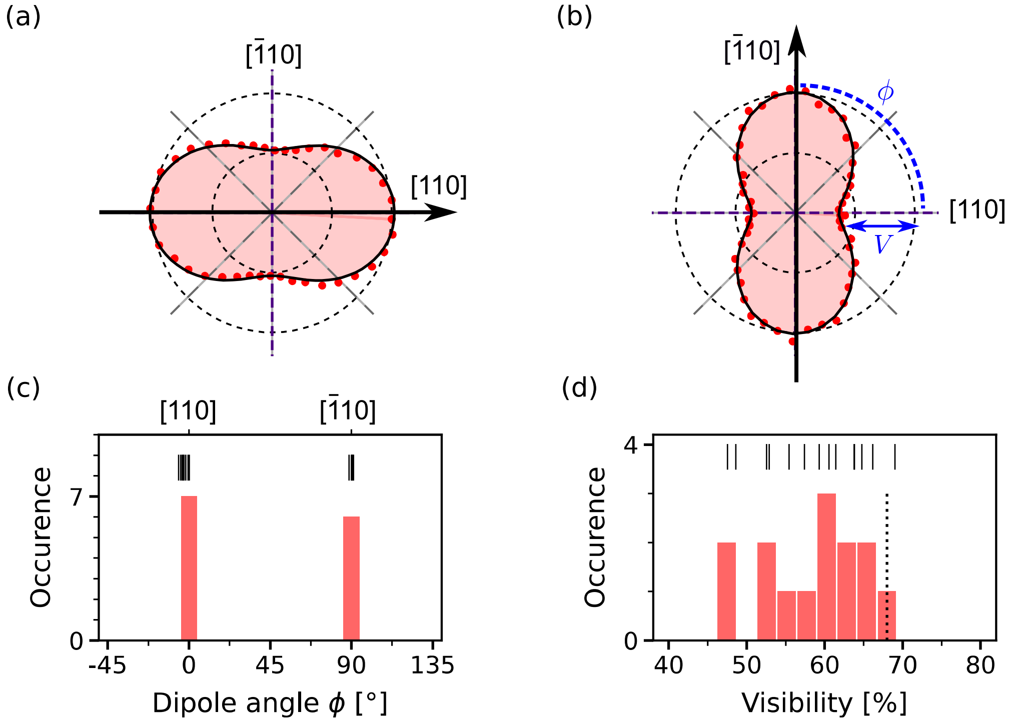

Figure 3.10: Polarization of the light emitted by single G-centers. **(a, b)** Polarization emission diagram recorded on two single G-centers. The signal is corrected from the background emission. Data are fitted with equation 3.1 to extract the angle ϕ between the principal polarization axis of the emission (arrow) and the $[1\,1\,0]$ direction as well as the visibility V. **(c, d)** Histogram of the angles ϕ and the visibility V recorded on a set of 14 individual G-center. Thin lines above the histogram represent the exact value of each data point. The prediction of the model including three dipoles is shown as a dotted line in (d).

The signature of multiple emission dipoles in the polarization diagram of individual G-centers is surprising because the emission of the defect corresponds to a singlet-to-singlet transition, when considering that the defect does not rotate [112]. Here the presence of multiple dipoles can be explained, however, by the fact the single G-center reorients itself continuously during the measurement. To confirm that a rotational reorientation of the defect through jumps between the 6 positions of the interstitial silicon atom can account for our observations, we build a simple model based on six independent emission dipoles.

Modeling of the G-center emission diagram

To explain the single G-center emission diagrams, a model of a single G-center oriented along the axis $[1\,1\,1]$ is considered. For each of the six positions of the interstitial silicon atom, a single emission dipole is considered, leading to six independent dipoles. A theory work from our collaborators Péter Udvarhelyi and Adam Gali from Budapest predicted that the G-center optical dipole is perpendicular to the plane formed by the two carbons and the silicon atoms. The six dipoles therefore form three pairs of equivalent dipoles, which correspond to the directions $[\bar{1}\,0\,1]$, $[\bar{1}\,1\,0]$ and $[0\,1\,\bar{1}]$ of the crystal (see figure 3.2). These three directions, when projected on the top $(0\,0\,1)$ surface, correspond to angles ϕ of $-45°$, $90°$ and $45°$ with the $[1\,1\,0]$ axis. The emission diagrams of each pair of dipoles are shown in figure 3.11(a).

To add the polarization diagrams corresponding to each orientation with the right contributions, the emission and collection of each dipole need to be considered. To this end, our collaborator Jean-Michel Gérard simulated the exaltation factor F (figure 3.11(b)) and the collection efficiency C_{eff} (figure 3.11(c)), for a dipole at a depth d in the top 60 nm silicon layer, and for a microscope objective with a numerical aperture of 0.85 It should be noted that the $[\bar{1}\,0\,1]$ and $[0\,1\,\bar{1}]$ dipoles are equivalent in this computation. The exaltation factor F is linked to the Purcell effect, and indicates whether the emission of the dipole is inhibited ($F < 1$) or exalted ($F > 1$) by its environment. The simulation reveals that the two pairs of dipoles with a contribution along the z axis ($[\bar{1}\,0\,1]$ and $[0\,1\,\bar{1}]$) are inhibited by a factor of ≈ 2 by the SOI structure, whereas the pair along $[\bar{1}\,1\,0]$ is mostly unaffected. The simulation of the collection efficiency (figure 3.11(c)), which considers the photons that exit the silicon layer with an angle collected by the microscope objective, reveals that the photon collection varies between $\approx 2.5\,\%$ and $\approx 4.5\,\%$, depending on the depth d. This collection efficiency is larger than the computed value for the SD-0 defect (see §2.2.4), as the 60 nm top layer is more adapted to extraction of the defect luminescence. Here the depth of the defect is an unknown parameter, but the collection efficiency is mostly the same for all the dipoles. To get the total collected photoluminescence of each dipole, the effective collection efficiency $F * C_{\text{eff}}$ is computed (figure 3.11(d)). The parameter which then determines the final contributions of each dipole is the ratio $r = (F * C_{\text{eff}}^{[-110]})/(F * C_{\text{eff}}^{[-101]})$ plotted in figure 3.11(e). Remarkably, this value does not depend strongly on the depth d, resulting in a final value $r = 2.1(1)$, where the error bar originates from the unknown value of d. The contributions from each of the 3 pairs of dipoles are then added, taking into account this factor of $r = 2.1(1)$. The resulting polarization emission diagram, shown in figure 3.11(f), matches very well with the experimental data, both in orientation and in shape. Furthermore, the visibility of the model $V = 68(1)\,\%$ corresponds to the maximum visibility observed in our experiments (see figure 3.10(d)). Here a single orientation of the G-center has been considered, along the $[1\,1\,1]$ axis. When considering the four main diagonals $[1\,1\,1]$, $[\bar{1}\,1\,1]$, $[1\,\bar{1}\,1]$ and $[\bar{1}\,\bar{1}\,1]$, the model predicts a 50:50 distribution between dipoles oriented mostly along $[\bar{1}\,1\,0]$ and $[1\,1\,0]$,

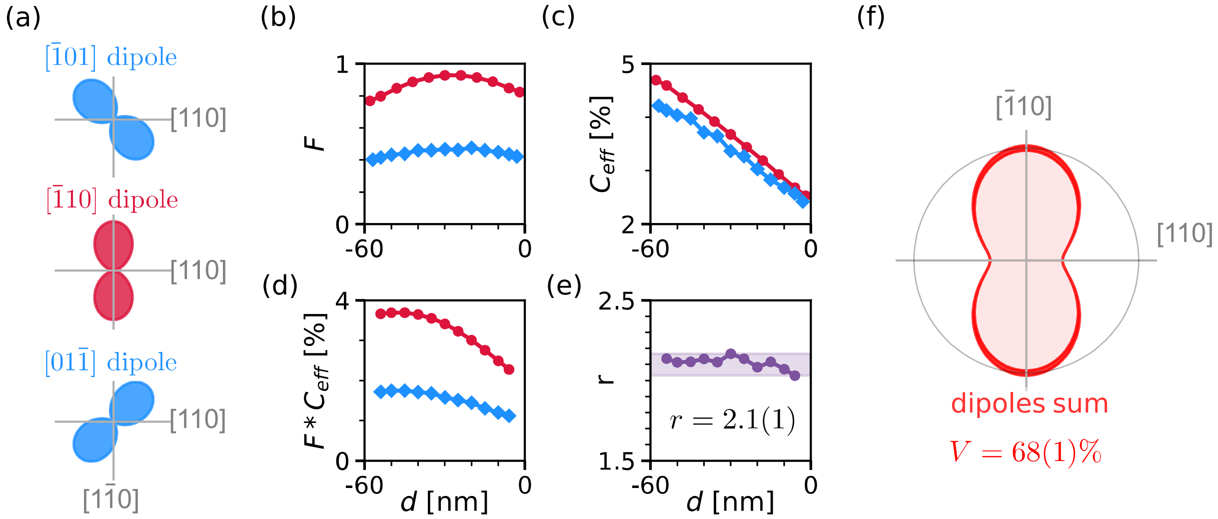

Figure 3.11: Model of the G-center emission polarization diagram. **(a)** Polarization diagram of three dipoles along $[\bar{1}\,0\,1]$, $[\bar{1}\,1\,0]$, and $[0\,1\,\bar{1}]$ when projected on the $(0\,0\,1)$ top surface. **(b, c, d)** Exaltation factor F, collection efficiency C_{eff} and their product $F * C_{\text{eff}}$ computed for dipoles along $[\bar{1}\,1\,0]$ (red circles) and $[\bar{1}\,0\,1]$ (blue diamonds) at a depth d in the top silicon layer and for a numerical aperture of 0.85. **(e)** Ratio r of the effective collection efficiencies $r = (F * C_{\text{eff}}^{[-110]})/(F * C_{\text{eff}}^{[-101]})$. The result is similar for every depth d, giving a final value of $r = 2.1(1)$. **(f)** Polarization diagram of the model computed by summing each contribution. The width of the line corresponds to the uncertainty of r. The model has a visibility $V = 68(1)\,\%$.

which corresponds exactly to the distribution observed in figure 3.10(c). This model thus explains our experimental data and confirms that the multiple dipoles are caused by the single G-center rotation.

The variations in the observed visibility in figure 3.10(d) suggests that the characteristic time the G-defects spend in each orientation is not equal. This effect could partly be explained by a large lattice strain, breaking the symmetry of the defect such that some positions of the interstitial silicon become more energetically stable than others. The rotation of the single G-defect, as well as the presence of such a large strain, is also corroborated by optical spectroscopy, as we will show in the next section.

Fine structure in the zero-phonon line of single G-centers

To look for evidence of the silicon atom rotation in the defect spectral response, photoluminescence spectra zoomed on the zero-phonon line were recorded for several G-centers. The grating of the spectrometer with the largest number of line (600 lines/mm) is employed, giving a spectral resolution of 0.11(1) nm per pixel at the ZPL wavelength. The spectra acquired on 7 emitters are plotted in figure 3.12. Surprisingly, multiple peaks of emission are observed for each emitter. We note that this fine structure is observed for single emitters, as verified by measurements of the $g^{(2)}(\tau)$ function. It should be noted that the spectral width of this fine structure is about two orders of magnitude larger than the one observed in the spectra of G-centers ensembles

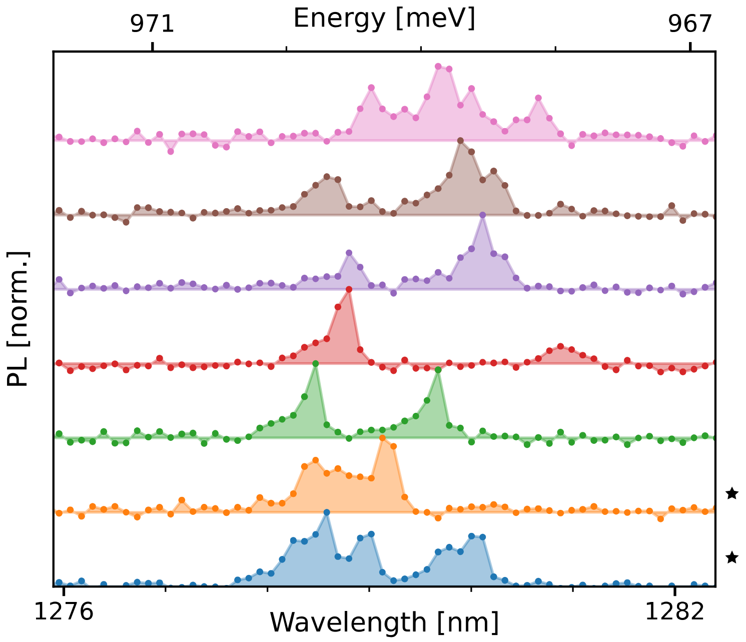

Figure 3.12: Photolumiescence spectra of isolated G-centers zoomed around their zero-phonon line. The stars indicate the spectra of the two single emitters that were verified by $g^{(2)}(\tau)$ measurements.

recorded in isotopically purified and strain-free ^{28}Si samples (see figure 3.4(a)). On ensembles of defects, the splitting of the zero-phonon line under strain is a well-known phenomenon called the piezospectroscopic effect. It has been widely studied for G-centers ensembles [83, 114, 119, 120] in order to determine the defect properties. The multiple lines seen on ensembles of defects and under compression are generally linked to the multiple orientations of many defects, which experience an orientation-dependent strain. Since we are here looking at a single defect, the presence of multiple lines can only be explained by the fact that the single defect reorient over time, thus experiencing the multiple orientation-dependent strain configurations over time. The maximum number of lines per single defect is not clearly resolved in figure 3.12, but is compatible with six positions of the interstitial silicon atom leading to up to 6 lines. For some defects, these six lines could fall roughly at the same wavelength, which we cannot resolve with our spectrometer.

In addition, as the splitting versus strain has been well studied on ensembles, we can use it to give an estimation of the local strain. The splitting of the G-center zero-phonon line depends on the exact direction of the stress, but is around of $\approx 1\,\mathrm{meV}$ for 100 MPa. As the observed splitting is of this order, we can conclude that a huge local strain is present in the sample, likely due to the nearby surface (<60 nm).

Spectral resolution of individual emission dipoles at the single defect scale

Since each of the emission lines in the photoluminescence spectrum should correspond to one emission dipole, an interesting measurement would be to record an emission polarization diagram with spectral filters at the position of each ZPL peak. This experiment could be performed with the appropriate spectral filters, but would be very challenging, as the photoluminescence signal would be very low. Fortunately, the inverse measurement, *i.e.* recording the spectrum for each polarization, can also give interesting results. This experiment has been performed on a single G-center, and is displayed in figure 3.13(a). The fine structure exhibits a dependency with the polarization, especially for the emission peak at the highest wavelength. To better visualize the polarization dependency of this peak, the luminescence signal is plotted in a polar diagram, thus displaying the spectrally-resolved emission polarization diagram (figure 3.13 (b)). Remarkably, this polarization diagram shows a visibility close to unity, corresponding to a single dipole of emission (or at least a pair of equivalent dipoles). The orientation of this dipole along the $[1\,1\,0]$ axis when projected on the top $(0\,0\,1)$ plane indicates, via our model, that this dipole is, in fact, along $[1\,1\,0]$ and is already in the $(0\,0\,1)$ plane. Here the single G-center is rotated by 90° compared to figure 3.11, which reveals that the single G-center is oriented along the $[\bar{1}\,1\,1]$ or $[\bar{1}\,1\,\bar{1}]$ axis.

The rest of the fine-structure is not well resolved, as multiple lines likely overlap. Still, a detailed analysis of the emission diagrams for each wavelength reveals that for two wavelengths, the emission is partly polarized near −45° and 45° (figures 3.13(c) and (d), respectively), corresponding to dipoles $[\bar{1}\,0\,1]$ and $[0\,1\,\bar{1}]$ in the model. However, the visibility of these two diagrams is below unity, as the others spectral lines partly overlap. This measurement could benefit from longer acquisition time in the future, but clearly demonstrates the possibility to isolate single dipoles via spectral filtering.

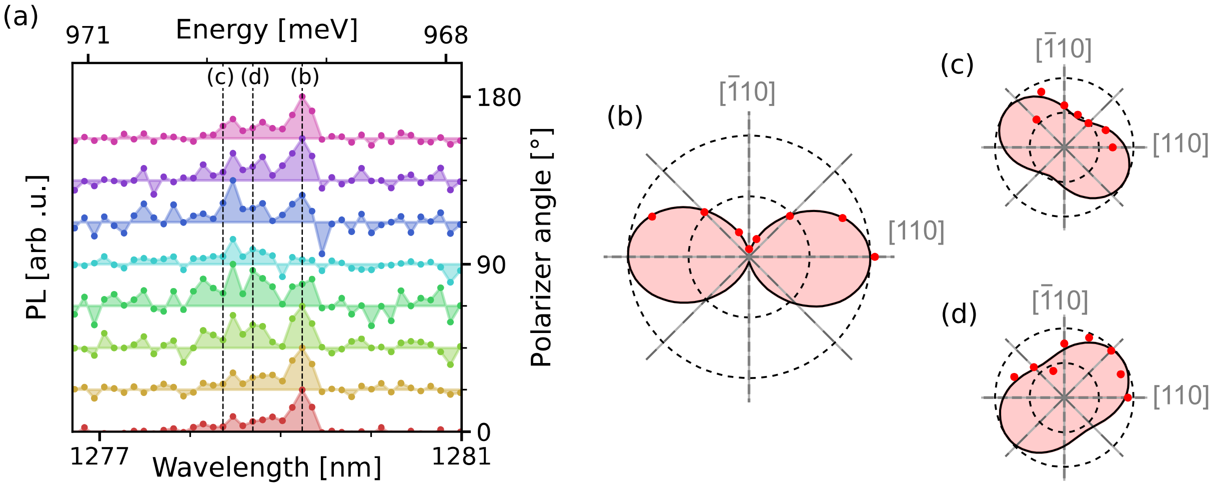

Figure 3.13: Polarization dependency of the photoluminescence spectra of a single G-center. **(a)** Photoluminescence spectra taken on a single G-center for varying angles of polarization (right axis). Each spectrum corresponds to 30 minutes of acquisition. **(b, c, d)** Polarization diagram of the emitted light at specific wavelength. The data are fitted with equation 3.1. For (b) a visibility of $V = 96(2)\,\%$ is extracted.

For now, the timescale of the G-center rotation is not known, but further analysis of the single defect luminescence correlations could elucidate this question. The effect of the temperature on this rotation has not been investigated yet, but this parameter is likely to have a major role on this phenomenon.

The isolation of the G-center at the single scale has enabled a detailed study of its photophysics at the single scale, as well as the observation of the rotational reorientation on single emitters. This unusual phenomenon is very interesting, but might create a challenge for future applications in quantum technologies. The presence of a fine-structure in the photoluminescence spectrum, either with or without strain, would limit the achievable photon-indistinguishability if no filtering is done. For quantum communication, a single dipole of emission is also preferred. In the next section of this chapter, we will demonstrate the isolation of single W-centers in silicon, which possess a single emission peak and a perfectly linearly polarized emission.

3.2 Isolation of single W-centers in silicon

Intrinsic defects in silicon, that are made of vacancies or/and interstitials, have been thoroughly investigated for classical applications to improve the quality of silicon-based components. Indeed, they are responsible for performance degradations of silicon devices when unintentionally produced, *e.g.* during device nanofabrication [121], or in environments subject to strong radiation like in particle physics experiments [122,123]. However, recent research on fluorescent centers in silicon for quantum applications has been mainly focused on extrinsic defects, which require the incorporation of impurities, such as carbon atoms [36,81,124] or rare-earth ions [92] inside the silicon lattice. In contrast, intrinsic defects have attracted little attention for quantum technologies, although some are optically active and could be of interest for these applications, like the W-center in silicon.

The W-center is a fluorescent defect in silicon commonly observed after radiation damage [35]. It can also be intentionally produced by silicon implantation [103], neutron irradiation [125,126] or following laser annealing [127]. It has been used as an active medium in LEDs and optical resonators for silicon-based classical photonics [128–130]. The attractive properties of the W-center in silicon for quantum technologies relate both to its optical emission and to its intrinsic nature. First this defect features an intense zero-phonon line at 1218 nm, close to the telecom O-band, and that includes 40 % of the total emission of photons. Such a high value is pursued as only zero-phonon line emission can lead to photon indistinguishability. Secondly, since the W-center does not require the incorporation of other external elements in the silicon lattice, the recently developed method of laser writing could be considered to create them conveniently on-demand [131,132].

We will start by introducing the photoluminescence spectral signature of the W-defect, as well as its microscopic structure. We will then demonstrate the isolation of single W-centers in an ultrapure silicon sample, and study the defect photophysics at the single scale. Last we will investigate the W-center photodynamic, revealing the presence of a trapping state in the defect optical cycle.

In this section, all the measurements have been performed with two ID230 detectors, featuring a quantum efficiency of 10 %.

3.2.1 Presentation of the W-center in silicon

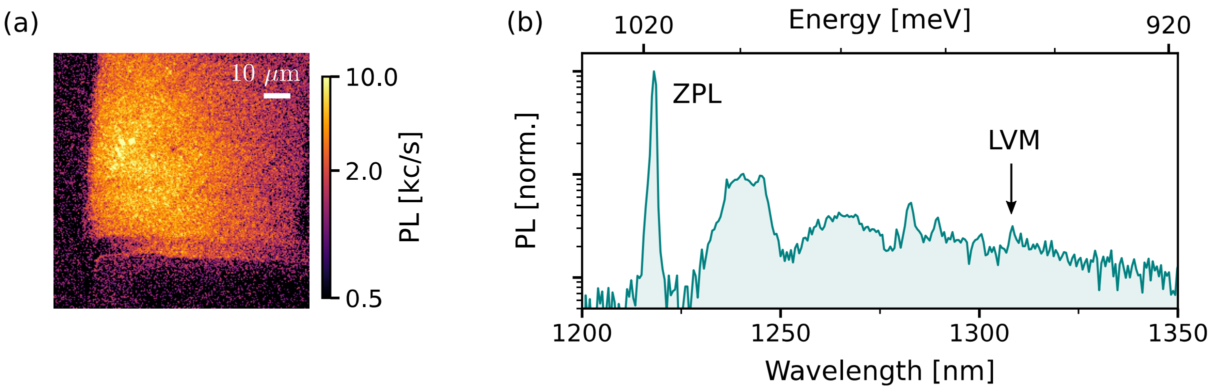

Figure 3.14: Ensemble of W centers created by silicon irradiation. **(a)** Photoluminescence scan of the implanted area. The implantation corresponds to a square of 100 µm × 100 µm with 65 keV ^{28}Si ions at a fluence of 3×10^{12} cm^{-2}. **(b)** Photoluminescence spectrum of the ensemble shown in (a). Data are plotted in semi-log scale. The spectrum matches the typical photoluminescence of the W-center. The spectra is dominated by a zero-phonon line at 1218 nm (1018 meV). A local vibrational mode (LVM) at 70 meV is shown by an arrow. All data are recorded at 10K.

Luminescence spectrum of ensembles of W-centers created by Si implantation

The photoluminescence spectrum associated with the emission of W-centers in silicon has been well known in the literature for more than 30 years [35]. To get such a spectrum as a reference, we have first created ensembles of W-centers in the same type of ^{28}SOI samples described in the introduction of the chapter (see figure 3.1), but this time by bombarding the lattice with ^{28}Si^{+} ions at 65 keV. At this energy, SRIM simulations [133] indicate that the ions stop partially in the upper ^{28}Si layer and mainly in the oxide layer below, but also that the number of collisions that produce the W-centers is maximized in the top silicon layer. To heal the silicon lattice from the damage done by the implantation, the sample underwent afterwards a flash annealing at 1000 °C, during 20 s and under N_2 atmosphere. Figure 3.14(a) shows a photoluminescence scan of a 100 µm × 100 µm square area of the sample that has been implanted with a fluence of 3×10^{12} cm^{-2}. The corresponding photoluminescence spectrum recorded in this zone displays the typical spectrum associated with the W-center in silicon [35] (figure 3.14(b)). In particular, it features a sharp zero-phonon line (ZPL) at 1218 nm (1.018 eV), along with a broad structured phonon-sideband that includes an emission line associated with a local vibrational mode (LVM) at 70.0 meV. Optical spectroscopy performed on ensembles of W-centers have brought insight into the microscopic structure of this defect by evidencing that it consists of a cluster of interstitial silicon atoms [35] with a trigonal symmetry along the $\langle 1\,1\,1 \rangle$ crystal direction [134].

Microscopic structure

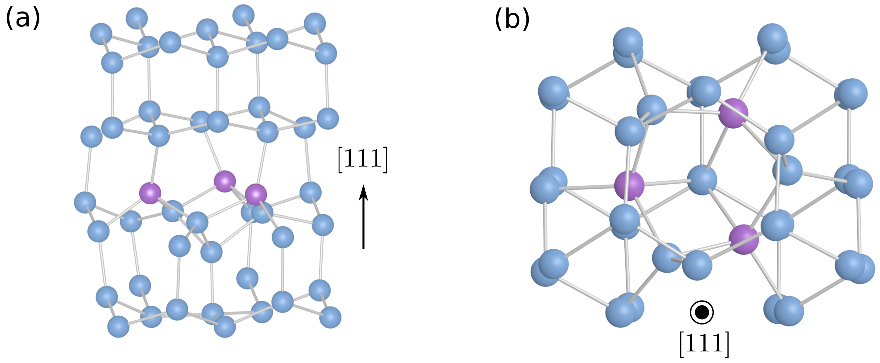

Figure 3.15: Microscopic structure identified as the W-center in silicon. **(a)** The defect, composed of three interstitial silicon atoms highlighted in purple color, displays a trigonal $C_{3\mathrm{v}}$ symmetry along the [111] crystal direction. **(b)** View from the [1 1 1] direction.

While it has been widely accepted that the W-center is linked to three interstitial silicon atoms [135], no clear consensus has still emerged on the exact microscopic structure of the defect [98, 135–140]. As part of a collaboration on the study of the W-center, its microscopic structure has been determined by our collaborators Péter Udvarhelyi and Adam Gali at the Wigner Research Centre for Physics in Budapest, Hungary. They showed via density functional theory (DFT) computations that, between the multiple forms proposed for the defect, only one could account for all its observed properties [141]. The structure of this configuration, shown in figure 3.15, resembles the corner of a cube whose large diagonal is along the ⟨1 1 1⟩ direction. Identifying the W-center emission to this structure is justified because it is has the lowest formation energy, it exhibits localized vibrations with the correct energy corresponding to the LVM at 70 meV, and it produces a below-bandgap optical emission with a zero-phonon line energy close to that of the W-line, in accordance to the observations. Our collaborators have also shown that this emission results from an unusual optical activity as this structure does not feature electronic energy levels within the silicon gap. Nevertheless, under photo-excitation, excitonic recombination between a hole localized at the defect and an electron trapped by Coulomb interaction leads to light emission, explaining the photoluminescence of the W-center in silicon [141].

After having briefly presented the spectral properties of ensembles of W-centers in silicon and their associated microscopic structure, we will now turn to the detection and study of single W-defects.

3.2.2 Isolation of single W-centers

The procedure which led to the detection of single W-centers is similar to the one presented previously for single G-centers in silicon. Starting with the ^{28}SOI sample introduced above, that has been locally Si-implanted to create ensembles of W-centers, we will now explore regions far away from the implantation areas.

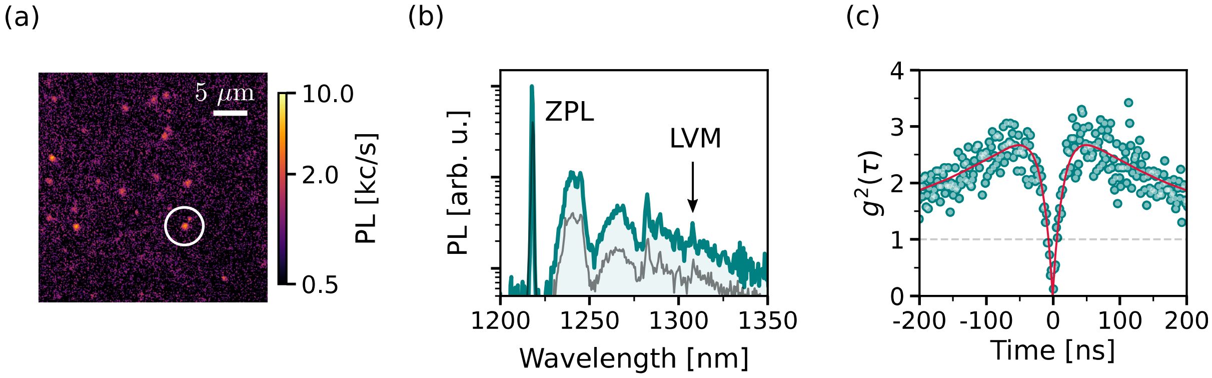

Figure 3.16: Observation of single W-centers in silicon. **(a)** Photoluminescence scan of the ^{28}SOI sample far away from the Si-implanted area. **(b)** Photoluminescence spectrum of the single W-center circled in (a). Data are plotted in semi-log scale. The photoluminescence spectrum taken on the ensembles of W-centers is shown as a thin gray line for comparison. **(c)** Second-order autocorrelation function $g^2(\tau)$ recorded on this single W-center. The antibunching effect at zero delay reaches the value: $g^{(2)}(0) \approx 0.12$, without any background or noise correction. All data are recorded at 10K.

Detection of isolated W-centers away from the implanted areas

To search for isolated defects, we move a few hundreds of micrometers away from the areas where ensembles of W-centers have been created by localized Si-implantation (see figure 3.14(a)). Optical scans of the sample reveal that it contains many isolated emitters, as shown on figure 3.16(a). To identify the defects at the origin of this luminescence, their photoluminescence spectra are recorded. As shown in figure 3.16(b), the photoluminescence spectrum of a localized spot reproduces exactly the one from the ensemble of W-centers. In particular, it presents a strong zero-phonon line precisely at 1218 nm. The Debye-Waller factor, that expresses the proportion of photons emitted into the ZPL, reaches ≈ 40 %. Moreover, these isolated defects exhibit the same phonon-side band structure as ensembles of W-centers, which includes specifically an emission line matching the local vibrational mode at 70 meV. We therefore conclude that these emitters correspond to W-centers in silicon.

The presence of isolated W-defects outside from the regions where the Si-implantation should have been localized is puzzling. Since they are not present in the reference samples that have not seen any implantation (see §3.1.2), these defects are neither native nor were created by the flash annealing. As the W-centers are only observed in the sample that has seen the local silicon implantation and not in the similar one that has seen carbon implantation instead, we are forced to conclude that these isolated W-defects were likely induced by the Si implantation process. Further investigations will be performed in the future to determine the exact creation process of these emitters and to optimize their creation at single-defect scale, for instance using focused ion beam [142] or laser writing [131, 132].

Demonstration of the single photon emission

To demonstrate that the isolated W-centers are single defects, we record their second-order autocorrelation function $g^{(2)}(\tau)$ (figure 3.16(c)). Remarkably, the measurement reveals a strong antibunching at zero delay with $g^{(2)}(0) = 0.12(5)$, without any background or noise correction. This value is below the single-photon emission threshold of 0.5 , thus confirming that the emission results from an individual W-center. In addition, the low value of $g^{(2)}(0) = 0.12(5)$ demonstrates that the emission features a good single-photon purity, which is here linked to a large signal-to-noise ratio (SNR ≈ 17). A bunching effect corresponding to $g^{(2)}(\tau) > 1$ is also revealed in the $g^{(2)}(\tau)$ plot. This effect will be further discussed in §3.2.4.

Now that single W-centers can be detected, it is possible to explore their photophysics and reveal new information impossible to access with measurements performed on ensembles of defects.

3.2.3 Study of the W-center photophysics at the single scale

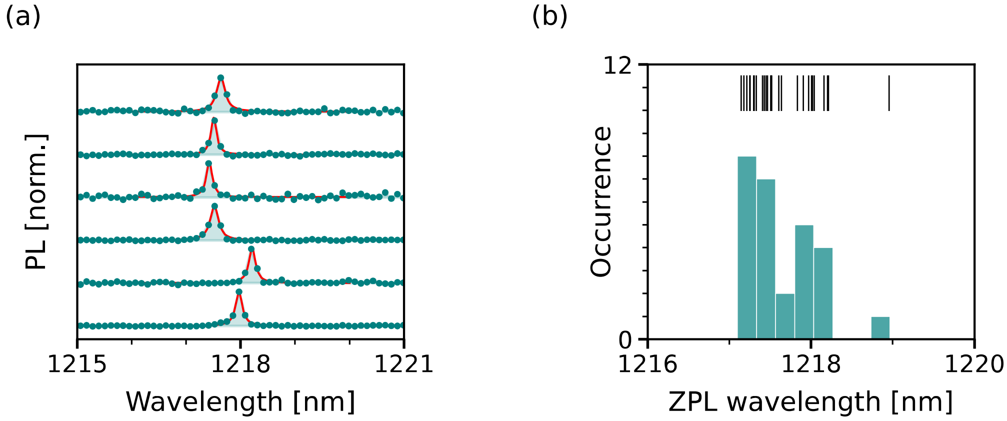

Figure 3.17: Zero-phonon line variations between single defects. **(a)** Typical spectra taken on 6 single W-centers. The spectra are normalized by the maximum and fitted with a Lorentzian function (solid red lines) to extract the central wavelength of the zero-phonon line. The full width at half-maximum is limited by the spectrometer resolution to ≈ 0.1 nm. **(b)** Histogram of the zero-phonon line wavelengths. Thin lines above the histogram represent the exact value of each data point.

Zero-phonon line low dispersion

To investigate the spectral dispersion of the single W-centers, photoluminescence spectra have been acquired on 27 defects, while using the maximum possible resolution on the spectrometer. The spectra recorded for six typical emitters in the sample are shown in figure 3.17(a). This analysis reveals that the single defects possess only one narrow zero-phonon line, whose linewidth is here limited by the resolution of the spectrometer. In addition, the zero-phonon line is slightly shifted from one defect to another. This variation is likely caused by the different strain and electrostatic environment experienced by each emitter [143, 144]. Still, this spread in ZPL wavelength is relatively small for the W-center, especially given that these emitters are embedded in a silicon layer that is only 60 nm thick. To illustrate this, the distribution of the wavelength over the full data set is plotted in a histogram in figure 3.17(b). It indicates that ZPL wavelength difference between two W-defects in mostly below 1 nm. We note that these fluctuations converted in energy are about 20 smaller than those observed on single SD-0 defects in a 220 nm thick silicon layer (see §2.2.1). This observation is consistent with the small sensitivity to stress variations previously reported for ensembles of W-centers in silicon [145]. Such low ZPL energy dispersion could ease achieving indistinguishability between the single photons emitted by two separated defects in future works.

Single emission dipole

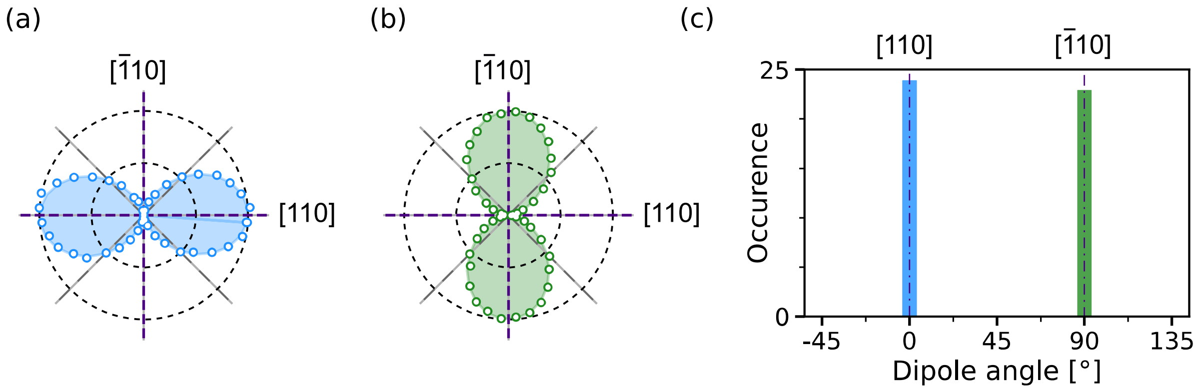

Figure 3.18: Orientation of the emission dipole of W-centers. **(a, b)** Emission polarization diagrams recorded on 2 individual W-defects. The data are fitted with equation 3.1 to extract the emission dipole angle that corresponds to the direction of maximal intensity. **(c)** Histogram of the emission dipole angle measured on a set of 47 individual W-centers.

The polarization analysis of the single photons emitted by these defects provides information about the orientation of their emission dipoles [146]. As shown on figures 3.18 (a) and (b), the emission polarization diagrams recorded on two typical W-centers display a visibility exceeding 96 %, indicating the emission of linearly polarized photons [147]. This result indicates that the W-center possesses a single emission dipole. In addition, a statistical analysis over a set of 47 individual emitters demonstrates that this dipole projected onto the (0 0 1) sample surface can take only two possible orientations with equal probability: either along $[1\,1\,0]$ or $[\bar{1}\,1\,0]$ (figure 3.18(c)). This observation is in perfect agreement with the W-center model that predicts a single emission dipole oriented along the $\langle 1\,1\,1 \rangle$ equivalent axis. Once projected on the sample top (0 0 1) surface, the four equivalent directions that the emission dipole could have, result in two possible orientations along these two crystal axes. The linearly polarized single-photon emission of single W-centers is another appealing feature regarding future quantum applications.

Photostability and count rates

The single-photon emission of individual W-defects can be photostable on hour timescale, as shown in the photoluminescence signal trace (figure 3.19(a)). However, at high optical power, typically above 500 µW of green laser, a photobleaching effect can happen for some emitters. This photobleaching is definitive, and is not reversed by warming up to 300 K and cooling again. This phenomenon, if not controlled, could be a limitation for future applications, and should therefore be investigated in future works. Fortunately, some emitters have been shown to be very robust and have survived after more than 50 hours of optical illumination.

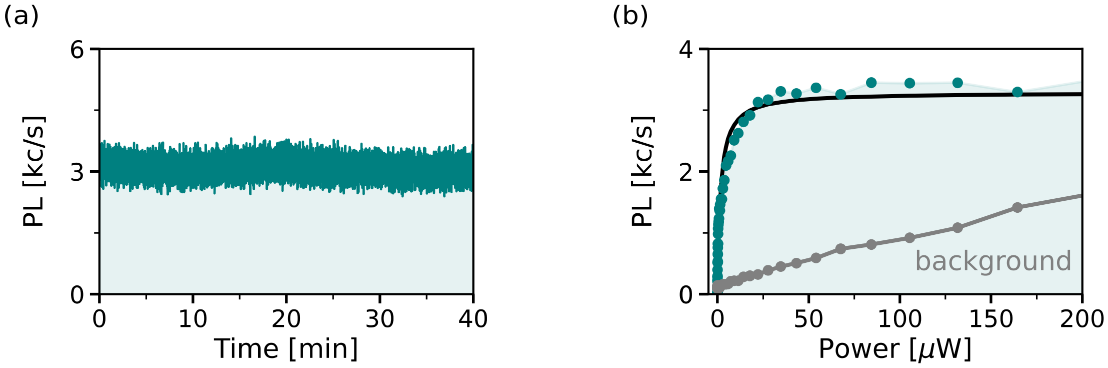

Figure 3.19: Photostability and photon count rates of single W-centers. **(a)** Typical photoluminescence time-trace measured at 30 µW on a single defect. **(b)** Background-corrected photoluminescence saturation curve recorded on an individual W-defect. The data are acquired on the emitter and on the background a few micrometers away from the defect.

To estimate the maximum count rate from individual W-centers, their photoluminescence evolution is recorded while changing the optical excitation power. The saturation curve recorded on one defect is plotted in figure 3.19(b), and features the standard saturation behavior expected for a two-level system. A fit with a saturation model given by equation 2.5 results in a saturation power $P_{\text{sat}} = 1.7(1)\,\mu\text{W}$ and a saturation signal rate $S_{\text{sat}} = 3.3(1)\,\text{kc/s}$. When correcting from the low quantum efficiency of the detectors used here (10 %), this saturation signal, which is typical for single W-centers in our sample, corresponds to an emission count rate ≈ 4× larger than the G-center emission. A statistical analysis over a set of 36 individual W-defects shows that this standard saturation behavior is only observed on 14 emitters. The rest of the W-centers displays anomalous saturation curves.

Anomalous saturation curves for single W-centers

For the W-defects, the optical power dependence of the photoluminescence intensity shows strong differences from one center to another. Figure 3.20(a) depicts the three typical photoluminescence evolution that have been noticed on individual W-centers. For 5 defects, the emission increases with optical power without saturating, such as defect W-6. For 13 defects, the signal intensity reaches a maximum and then decreases, similarly to defect W-3. At last, for the 4 remaining defects, the photon emission decreases after a first maximum and then rises

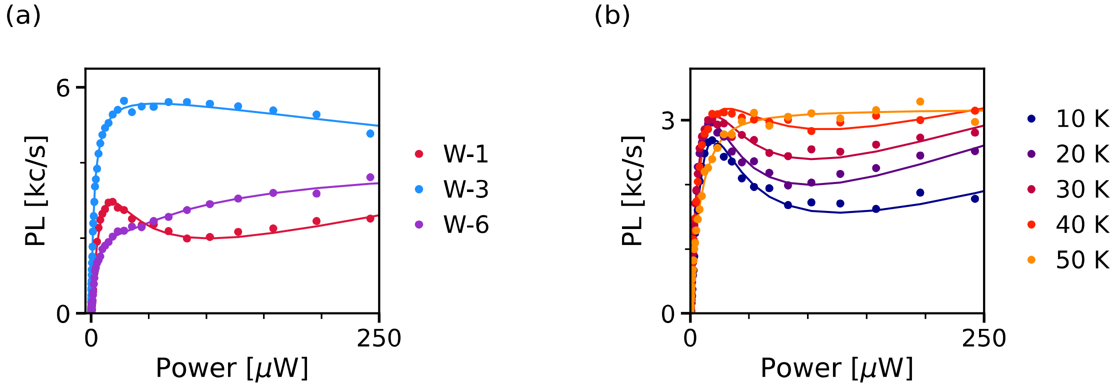

Figure 3.20: Anomalous saturation behavior observed on some single W-centers. **(a)** Typical photoluminescence saturation curves recorded on three W-defects at 20K. **(b)** Saturation curves measured on defect W-1 with increasing temperatures. Solid lines are a guides to the eye.

again, as for defect W-1.

These phenomena suggest that these W-centers are coupled, during the optical cycles, to a non-fluorescing state. This dark state is unlikely to be an intrinsic metastable level that would always produce the same behavior, from one W-center to another, but rather could be assigned to another charge or conformation state of the defect. The balance between the fluorescent form of the W-center and this dark state would be (i) specific to each center and dependent on its local environment and (ii) affected by the optical power exciting the defect. The dynamics of a 3-level system with transition rates to and from this dark state considered either constant or linearly dependent with power could not reproduce the data. A more complex structure is therefore required to account for these anomalous saturation curves. We note that no correlation between the excited level lifetime and the photoluminescence saturation evolution has been observed.

Most of the case, the coupling of the W-centers to the dark state disappears when increasing the sample temperature. As shown of 3.20(b) for defect W-1, the anomalous saturation effect is prominent at 10 K, but gradually fades away as the temperature rises, up to fully vanish at 50 K where, the saturation curve is back to the standard form. These results indicate that either the non-radiative state gets unstable or that the effective conversion rate becomes negligible with increasing temperature.

The observation of a complex saturation behavior which varies from defect to defect indicates that the photodynamics also varies between defects. We will see in the next section that this variation is even more pronounced in the measurement of the excited level lifetimes.

3.2.4 Photodynamics of single W-centers

Excited level lifetime

To investigate the photodynamics of the single W-centers, their excited level lifetime is measured under optical excitation with 50 ps laser pulses. The decay of the photoluminescence after the excitation pulse is plotted in figure 3.21(a) for 3 individual emitters. The photoluminescence signal decreases with a mono-exponential decay, but with a characteristic lifetime that strongly changes from one defect to another. The measurement performed on 13 defects indicates that the excited level lifetime can vary by one order of magnitude from roughly 3 ns up to 30 ns (figure 3.21(b)). It should be noted that all the measured values are shorter than the excited level lifetime recently reported on an ensemble of W-centers that reaches 34.5(5) ns [103]. The fluctuations in measured lifetimes are currently not understood but could be linked to an excitation transfer mechanism between the W-defects and non-radiative recombination centers at their vicinity [55]. This effect could also be linked to the unusual saturation behavior described above, but no clear correlation between the two phenomena has been established.

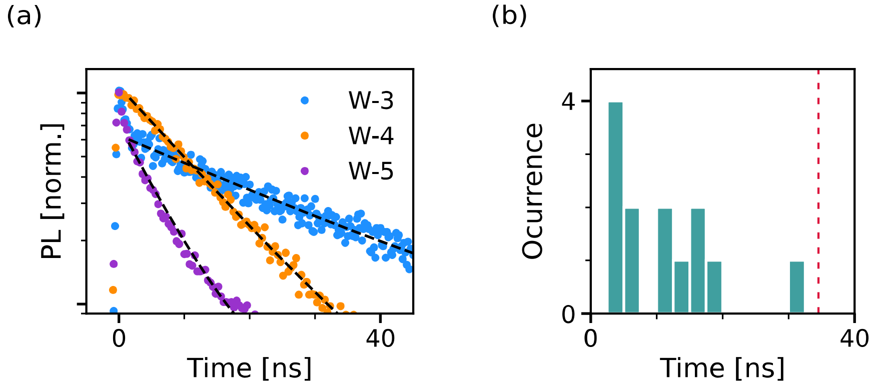

Figure 3.21: Excited level lifetime of single W-centers. **(a)** Time-resolved photoluminescence recorded for 3 W-centers under a 50 ps pulsed laser excitation at 532 nm. The excited level lifetime is extracted from data fitting with a single exponential function (dashed lines). The sharp peak at the beginning of the pulse for W-3 comes from background counts. **(b)** Histogram of the excited level lifetimes measured on a set of 13 W-centers. The red dashed line represents the 34.5 ns excited level lifetime value reported from an ensemble measurement [103].

It should be noted that the investigation of the excited lifetime of single W-centers is particularly challenging as the pulsed laser tends to photo-bleach parts of the defects rapidly. This observation is easily explained by the fact that during the 50 ps of the laser pulse, a very large laser power is applied on the defects. An alternative route to study the single W-centers photodynamics, which does not involve the use of a pulsed laser, is to look at their second-order auto-correlation function $g^{(2)}(\tau)$ under continuous laser excitation.

Evolution of the W-defects $g^{(2)}(\tau)$ with laser power

The second-order auto-correlation function $g^{(2)}(\tau)$ power dependency can be studied to gain access into the photodynamics of the W-defect. This measurement is, furthermore, motivated by the fact a large bunching (*i.e.* $g^{(2)}(\tau) > 1$) was observed in the first $g^{(2)}(\tau)$ function measurement (see figure 3.16(c)), which can only be explained by the coupling to a third level in the W-defect dynamics. As the W-center optical emission corresponds to a spin singlet-to-singlet transition [145], the presence of a bunching could be linked to the coupling to a metastable level which would be a spin-triplet, possibly useful for applications. To investigate the W-center dynamics and its coupling to the third level, we record the $g^{(2)}(\tau)$ function on a single defect while increasing the laser excitation power (figure 3.22(a)). The analysis, which is similar to the one introduced for the study of the SD-0 emitter (see §2.2.3), allows (i) to determine the excited level lifetime, which can be obtained by extrapolating the antibunching behavior at zero laser power, and (ii) to study the evolution of the bunching signal with the laser power, linked to the dynamics of the third level. The $g^{(2)}(\tau)$ function of the W-center displays a bunching at each laser power, but the amplitude and the timescale of this bunching decrease with the laser illumination power. Remarkably, this phenomenon is very similar to the case of the SD-0 defect in chapter 2. This phenomenon should be investigated to assess if it is a universal behavior resulting from above bandgap excitation.

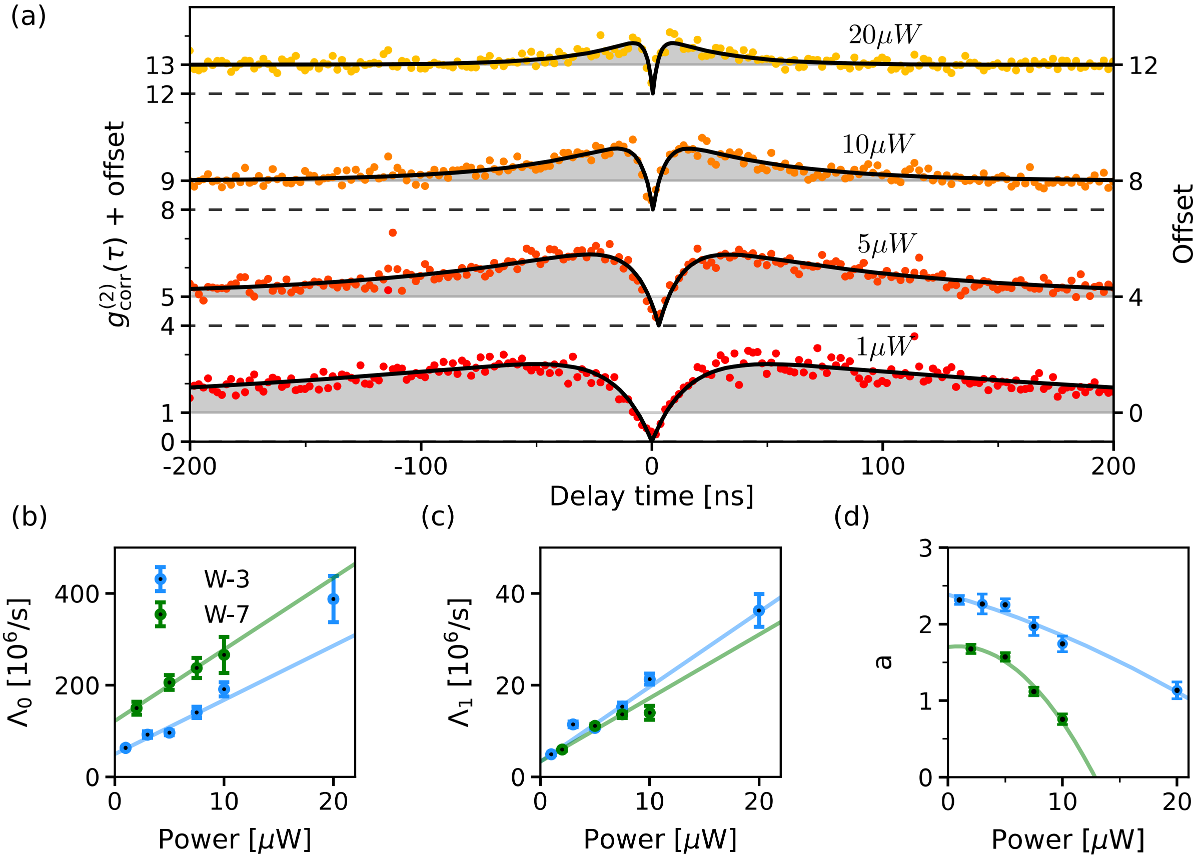

Figure 3.22: Evolution of the $g^{(2)}(\tau)$ with the laser excitation power. **(a)** $g^{(2)}(\tau)$ recorded on a single W-center at several laser powers. The data are fitted with equation 2.7 to extract the rates Λ_0, Λ_1 and the parameter a. **(a, b)** Evolution of the rates Λ_0 and Λ_1 with increasing optical power. The solid line corresponds to a linear fit. The rates for 30 μW are not shown as the fit did not properly converge. **(c)** Evolution of parameter a versus optical power. The solid line corresponds to a guide to the eye.

To analyze quantitatively the photodynamics of the single defect, the $g^{(2)}(\tau)$ data for each laser power are fitted with the equation 2.7, that results from solving the rate equations of a

3-level model (see §2.2.3). This fit allows the extraction of the two rates Λ_0, Λ_1 associated with the antibunching and bunching times, respectively. The parameter a which describes the bunching amplitude is also obtained. The evolution of these parameters with the laser power is shown in figures 3.22(b, c, d) for two defects.

The rate Λ_0, which is linked to the antibunching, evolves similarly for the two defects, but with a vertical offset. As the value of the rate $\Lambda_0(P = 0)$ corresponds to the excited level decay rate [95], this offset in linked to the difference of lifetime between the two defects. For defect W-3, the lifetime was recorded (see figure 3.21), while for W-7, the emitter photo-bleached during the lifetime measurement. Interestingly, the lifetime of this second defect can be estimated from the study of the antibunching rate. The rates Λ_0 for the two defects are fitted by the linear equation: $\Lambda_0 = a_{\Lambda_0} \times P + b_{\Lambda_0}$. For W-3, the inverse rate $1/b_{\Lambda_0} = 20(3)$ ns is close to the excited level lifetime measured previously on the defect $\tau_e = 16.8(2)$ ns, given the error bars. For W-7, the inverse rate $1/b_{\Lambda_0} = 8.2(5)$ ns allows a direct determination of the emitter lifetime τ_e which was unknown. All the values of the fit are given in table 3.1.

Center		W-3	W-7
Λ_0	a_{Λ_0} [MHz/μW]	11(2)	15.6(14)
	$1/b_{\Lambda_0}$ [ns]	20(3)	8.2(5)
Λ_1	a_{Λ_1} [MHz/μW]	1.6(2)	1.4(2)
	$1/b_{\Lambda_1}$ [ns]	300(50)	300(80)

Table 3.1: Fitting results for the W-center $g^{(2)}(\tau)$ evolution with laser power. The rates Λ_0 and Λ_1 are fitted with a linear equation $\Lambda_i = a_{\Lambda_i} \times P + b_{\Lambda_i}$. The inverse rates $1/b_{\Lambda_i}$ corresponding to characteristic times at zero powers are given.

The dynamics of the bunching, which is linked to a third level in the dynamics, can also be analyzed via the same method. At low power, the rate Λ_1 corresponds to the decay rate in the dark from this third level. Remarkably, this rate is non-zero for both defect and corresponds roughly to the same values. By fitting the rate Λ_1 with the linear model: $\Lambda_1 = a_{\Lambda_1} \times P + b_{\Lambda_1}$, a lifetime of $1/b_{\Lambda_1} \approx 300$ ns is extracted for both defects. This lifetime could correspond, if this third state is a spin triplet metastable level, to the lifetime of this metastable level.

Further investigation is required to get a clear picture of the photodynamics of single emitters in silicon. If the bunching signal observed for the single W-centers is linked to a metastable spin-triplet, this defect would be a very interesting candidate for applications in quantum technologies.

3.3 Conclusion

In this chapter we have demonstrated the first optical isolation at the single scale of two well-known fluorescent defects in silicon: the G-center and the W-center. After reviewing their optical properties and microscopic structures, we showed that these defects can be created by performing ion implantation in an isotopically purified ^{28}Si layer of a SOI structure. The G-center, which exhibits a stable single-photon emission in the telecom O-band, is a promising defect owing to a spin triplet metastable level which was detected through optically detected magnetic resonance in the 80s [40,41]. By studying the polarization of the single-photons emitted by the defect, we have shown evidence that the G-center possess multiple dipoles of emission, which are linked to the reorientation of the defect between 6 quasi-equivalent positions over time. The investigation of the fine structure in the single defect's emission has corroborated this hypothesis, allowing the spectral resolution of individual emission dipoles.

The study of the W-center in a similar isotopically purified ^{28}Si layer has demonstrated some remarkable properties for future applications. The W-center exhibits a perfectly linearly polarized emission, corresponding most likely to a $\langle 1\,1\,1 \rangle$ single dipole of emission. The spectral properties of the defect are also interesting, as the W-center display only one narrow peak of emission, which contains $\approx 40\,\%$ of the photons emitted by the defect. The analysis of the single W-center dynamics has revealed strong defect-to-defect variations, which remains to be clarified. In addition, the study of the W-center $g^{(2)}(\tau)$ has revealed the presence of a trapping state with a lifetime of $\approx 300\,\mathrm{ns}$, which could correspond to spin triplet metastable level.

The implantation process, which was used in this chapter to create the isolated G- and W-defects, was observed to affect the whole sample surface, thus raising questions on the exact origin of the defects far from the implanted areas. The use of other methods of defect creation, such as electron irradiation [104], focused ion beam [142], or laser writing [131,148], could enable alternative methods of creation, while reducing the damages done to the silicon lattice, which can degrade the optical performances of the defects. The understanding of the G- and W-centers creation is also of interest for large ensembles of defects, as the G-center is currently investigated as a gain medium for G-center-based lasers [108].

As all the measurements in silicon in this manuscript have been performed with a green laser above-bandgap excitation, an all-electrical excitation, relying on a current injection, should result in a similar emission. Such a result remains to be demonstrated at the single scale, but could open prospects for the development of a deterministic and electrically driven single-photon source in silicon, with many applications for quantum technologies.

Conclusion

My thesis has been focused on the study of optically active defects in semiconductors.

In chapter 1, we have first investigated the optical properties of the well-known NV center in diamond. More precisely, we analyzed its dynamics of charge state conversion and showed that the optical excitation cycles populate a long-lived dark state, which corresponds to the metastable level of the neutral charge state NV^0. By developing a new model which encompasses these dynamics, we explained several other phenomena of the NV center photophysics that were still misunderstood.

The heart of my thesis was then dedicated to the isolation of single fluorescent defects in silicon.

In chapter 2, we described the first optical isolation of a single defect in silicon. First we presented the design of the experimental setup built during my PhD, which is a low temperature confocal microscope optimized for the detection of single emitters in the near infrared. Then, using a carbon implanted sample, we demonstrated the isolation of seven families of single defects that are not referenced in the literature. These defects all emit single-photons in the near-infrared, some even at telecom wavelengths, and are all linearly polarized. Furthermore, some defects display remarkable properties, such as a bright emission up to 120 K, well above the 77 K liquid-nitrogen temperature, or a small spread of the emission wavelength.

In chapter 3, we focused on two well-studied defects of the literature: the G-center and the W-center. As the microscopic structure of these defects is now established, theoretical support is possible to guide the experimental work toward future applications. We showed that these two defects can be created and isolated at the single scale in an isotopically purified silicon layer. The study of the G-center revealed a rich physics caused by the reorientation of the defect over 6 equivalent positions. The investigation of individual W-centers exposed a bright linearly polarized emission with one narrow peak of emission, weakly disturbed by the local strain.

Outlook

The isolation of single point defects emitting at telecom wavelengths in silicon open multiple prospects for quantum technologies. These defects are highly promising to develop silicon-integrated deterministic sources of photonic qubits, and spin-qubits interfaced with light for long-distance quantum communications, in a platform adapted to large-scale integration. However,

in order to enable such breakthroughs, they must fulfill two *sine qua none* requirements.
(1) The emission of single indistinguishable photons. The objective being to implement two-photon quantum interference, that is the basis of remote entanglement generation [23,149].
(2) The control over the spin degree of freedom of the defects, the long-term objective being to create a multi-spin quantum register coupled to single photons in silicon.

Emission of indistinguishable photons

Photons are said to be indistinguishable when they share exactly the same properties, *i.e.* their polarization, emission wavelength, linewidth and spatial mode. The indistinguishability between two photons is measured through the so-called Hong-Ou-Mandel (HOM) experiment [150] (figure 3.23(a)). It consists in making them interfere on a 50:50 beam splitter and measuring the coincidence counts on the two detectors at the output. If two photons are perfectly indistinguishable from each other, quantum mechanics predict that they will always exit the beam splitter by the same output port, resulting in zero coincidence counts [78]. The HOM interference visibility is thus providing the degree of indistinguishability between the two input photons.

Achieving indistinguishable photon emission at the solid-state is a notoriously difficult task for two main reasons [151]. First, the defect's emission lines can undergo spectral diffusion [152]. This effect results from charges moving in the vicinity of the defects, producing randomly fluctuating Stark effects on the optical transition frequencies. Depending on the fluctuations timescale, this effect can produce either spectral broadening or/and spectral hopping of the optical lines of the emitters [152]. Secondly, because of different local strain environments, defect emission occurs in general at different wavelengths from one defect to another [153]. To overcome both issues, a promising route is to integrate the defects in p-i-n junction under reversed-bias. This method has been demonstrated to deplete the local environment of the electrical charges, leading to a narrowing of the optical transition, for single defects in silicon carbide [84]. Furthermore, this same reversed-bias can be used to tune the defect's emission wavelength via Stark effect, thus enabling the tuning of two defects to the same wavelength. The demonstration of indistinguishable single photon emission from individual defects in silicon is the next experimental challenge of our research group.

Spin-control at the single defect scale

A second challenge is to demonstrate that the G- and W- center can be used as optically active spin qubits in silicon [154]. A first step will be to demonstrate optically detected magnetic resonance (ODMR) on a single defect. The principle is to detect the photoluminescence of the emitter while sweeping the frequency of a microwave magnetic field. When the microwave reaches the spin transition frequency, it will flip the spin transition resulting in a photoluminescence change. Although an ODMR signal associated with a metastable spin triplet has been reported in the 1980's on a dense ensemble of G-centers [40,41], its physical origin is currently unknown. It should be noted that measuring ODMR signals in silicon is notoriously challenging, as they are often hidden by unrelated signal stemming from free carriers, whose behavior and recombination

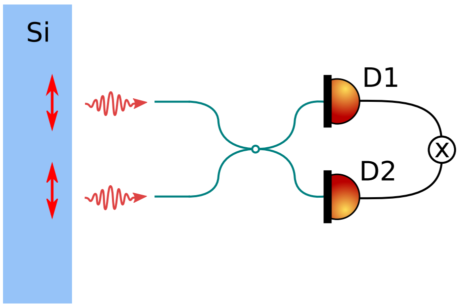

Figure 3.23: Principle of the Hang-Ou-Mandel experiment. The photons emitted by two defects are sent on a 50:50 beam splitter. The output correlations are recorded on two single-photon detectors.

are influenced by static and microwave magnetic fields [155, 156]. The installation near the end of my PhD of a vector magnet based on 3 superconducting coils inside the cryostat vacuum chamber will enable the investigation of these effects in the future, in order to determine the best experimental conditions to measure an ODMR signal on individual defects in silicon.

If the G- and W-center end up being not adapted to the control of a single electron spin, other defects could be investigated. A promising candidate is the T-center, which was shown to possess a spin-triplet ground level, controllable coherently at the ensemble scale [36]. This defect has, however, a long excited level lifetime of $\approx 1\,\mu s$, which renders the single scale isolation challenging. Very recently, these center have been nonetheless isolated via resonant excitation in photonic microstructures [37], but the low number of photon counts did not allow for a $g^{(2)}(\tau)$ measurement. Purcell enhancement could open a way to bright T-centers but remains to be demonstrated.

Beyond quantum technologies, the study at the single scale of defects in silicon opens prospects for a wide diversity of technological fields. Indeed, the methods used in this manuscript can be used as tools to characterize the impurities in silicon with an extreme sensitivity. This characterization tool is notably of interest for research in high-energy physics, since the silicon-based detectors commonly used in this field are subject to radiations which can create defects such as the W-center [122], which act as recombination centers degrading the detector performances over time. A deeper understanding of the defect properties could thus enable the engineering of radiation-tolerant silicon detectors. Characterization of defects in silicon could also have an impact on the production of solar cells for energy productions. Silicon solar cells performances are indeed known to degrade with the presence of defects [157], acting as recombination centers before the current can be extracted.

One last prospect is the application of silicon defects as sources of light for cryogenic optoelectronics in silicon. Optoelectronics uses both light and electronics to perform computational tasks.

Neuromorphic super-computing has for example shown interest in W-center based LED [129], to develop a cryogenic low consumption light source in silicon. The development of defect-based silicon light source could therefore open a new path toward solving hard problems [158], even without the need for a quantum advantage.

Appendix A

History of the experimental studies of the G-center in silicon

The G-center is one of the oldest studied defects in silicon. Its current name was introduced in 1971, but it was initially identified 15 years prior.

The first report of the G-center dates back from 1957 by G. K. Wertheim at the Bell Telephone Laboratories in New Jersey, USA. From fast capacitance measurements under pulsed electronic excitation [159], and by varying the temperature, a silicon acceptor level 0.16 eV below the conduction band was detected [160]. This observation generated one of the first physical models of deep-level defects in semiconductors.

One year later, G. Bemskin, also from the Bell Telephone Laboratories, reported an EPR study on a defect in an electron irradiated silicon sample [161] and proposed an oxygen-related origin, as oxygen was known to be present in the sample. Bemski noted at the end of the paper that the defect was destroyed by annealing in the same temperature ranges as the defect described by Wertheim.

In the same volume of the journal than [161], the following paper from G. D. Watkins et al. [162] at the General Electric Research Laboratory in New York, USA, studied multiple spin resonances in electron irradiated silicon. One of the resonances is the same as Bemski's which they named the "A-center", a name that will be used in some literature for the later called G-center.

Six years later in 1965, in Leningrad, USSR (now Saint Petersburg), A. V. Yukhnevich observed in a silicon sample containing "A-centers", a fine structure in the photoluminescence under carrier injection in a p-n junction [163]. He reported a sharp emission line at 0.967 eV associated with a broadband emission. The sharp line was attributed to a zero-phonon-line from a localized defect, and the broadband emission to phonon-assisted luminescence. Because of the presence of A-centers in the sample, Yukhnevich attributed the emission to this EPR defect.

In 1971, Jones and Compton in Illinois, USA, studied luminescence in electron irradiated silicon [119]. They labeled each of the 7 peaks in their photoluminescence spectrum from A to G. The name of the G-center comes from this paper, with a G-line at 0.97 eV (as well as the E-line). They showed by stress measurements that the G-line corresponds to a $\langle 1\,1\,1 \rangle$ trigonal center and suggested the center is a divacancy. In a discussion joint to the paper [119], Watkins casted doubt right away on their microscopic model, but the authors claimed their model fitted best with their current knowledge. In the following years conflicting experimental results regarding the defect symmetry [164] complicated its identification.

In 1976, Noonan et al. in Illinois, USA, proved the G-line could not be linked to a divacancy from annealing arguments [165]. They suggested instead that the G-line was carbon-related, and they made a connection with the well-known carbon-related EPR Si-G11 signal observed by Watkins in 1965 [68] and by Brower in 1974 [166].

In 1981, C. P. Foy et al. in London, UK, conducted another measurement of the G-line under uniaxial stress. They concluded that the defect had a monoclinic I symmetry, but also noticed that the intensity of the split lines varies with the temperature. They thus concluded that the G-center must reorient over time to explain this phenomenon.

The same year, Thonke et al. in Stuttgart, Germany, published an in-depth study of the G-line under stress [114]. They experimentally proved that the E-line was linked to the G-center as the two lines were always present together in their samples, and because the lines split similarly under stress. They also proved the involvement of carbon in the defect via isotopic shifts. Importantly, they measured the decay time of the optical transition to be less than their resolution of 10 ns, and estimated the quantum efficiency to be superior to 0.1 via intensity arguments. A short lifetime and a large quantum efficiency suggested that the G-center is very bright. Still they proposed an erroneous model involving one silicon and one carbon atom as they observed the signature of only one carbon in isotopically-controlled samples.

In 1982, G. D. Watkins (now in Pennsylvania, USA) used a new spin detection optical technique developed 15 years earlier for organic molecules [167]. They performed the first Optically Detected Magnetic Resonance (ODMR) in silicon and discovered the presence of a spin triplet associated to the G-line [40]. The G-line was known to be a spin singlet to spin singlet optical transition. They observed a signal only under illumination, so they concluded that they were probing a metastable spin triplet populated only under excitation. They also observed the indication of a symmetry change from a monoclinic to a trigonal symmetry depending on the applied stress and temperature. They concluded that the G-center must reorient over time to explain such behavior too.

One year later, the same team, in another paper [41], identified the exact structure of the G-center via ODMR measurement on ^{13}C enriched sample. From the signature of two equivalent carbon atoms, they concluded that the G-center involves two substitutional carbon atoms and one interstitial silicon atom, the structure that is accepted today. They also confirmed that the G-center luminescence was linked to the Si-G11 EPR signal but in a different charge state.

The newly identified microscopic structure generated the search for an optical signature of the second carbon. In the same year of 1983, G. Davies et al. [168] in London, UK, reexamined the G-line vibronic sideband and uncovered the presence of a second carbon atom via slight change (0.1 %) in the E-line replica energies. This result closed the debate of the microscopic structure.

One notable result is the photovoltaic detection of magnetic resonance (PDMR) by Yan et al. [169] in Hull, UK, in 1985. They performed ODMR and PDMR detection and linked their result to the previously identified G-center. This result suggests an alternative route to spin detection on single defects as was recently demonstrated for diamond [170].

The next big step in the G-center history was the publication by the group of G. D. Watkins in 1990 of a 19-page article on the bistability of the G-center [171]. They showed that there were two possible forms of the defect named A and B, with a stability depending on the charge state of the defect. The luminescent B-form, stable in the neutral charge state, stems from two symmetric carbon atoms. The A-form observed in EPR and initially detected as the $E_c - \sim 0.17\,\mathrm{eV}$ signal is stable in the negative and positive charge states. In this configuration, one carbon is substitutional while the other carbon and the silicon atom are interstitials. By combining all the spectroscopic techniques available, they determined the charge state energy diagram of the G-center and explained most of the reported results with their model. By answering many of the open questions around the G-center, the paper from G. D. Watkins also slowed down the experimental study of the defect for many years.

In 1997, Afanasjev et al. in St-Petersburg, Russia, showed the thermally activated change of symmetry between monoclinic and trigonal by electron paramagnetic resonance (EPR) [113]. This result corroborated the rotation of the G-center over time.

In 2005, Cloutier et al. in Providence, USA, observed optical gain and stimulated emission from periodic nanopatterned crystalline silicon [108]. They attributed the emission at 1278 nm to the A-center of silicon. Their result suggested the possibility of a G-center based laser in silicon, a subject currently investigated by our collaborators.

In 2018, Beaufils et al. from our group in Montpellier, France, revisited the G-center properties and measured the excited level lifetime to be 5.9 ns [39].

In 2018, Chartand et al. in Burnaby, Canada, measured a fine structure in the G-center zero-phonon-line in isotopically purified ^{28}Si [104]. The fine structure is present both in photoluminescence and absorption and is a direct proof of the G-center silicon atom tunneling between 6 equivalent sites, as was predicted independently by theory [112].

The story of the G-center is still being written and hopefully, will show other beautiful developments. To finish, I find it amusing to look back at the introduction of the first ever G-center focused paper by G. Bemski in 1959 [161] in which he wrote: *This paper represents a progress report on work which has started relatively recently. It is hoped that with time one will be able to describe completely the electronic structure of the radiation induced centers. At this time, however, we will review the experimental results with less emphasis on a definite model.*

Bibliography

[1] A. G. J. MacFarlane, J. P. Dowling, et G. J. Milburn. "Quantum technology: the second quantum revolution." *Philosophical Transactions of the Royal Society of London. Series A: Mathematical, Physical and Engineering Sciences*, **361**, 1655 (2003).

[2] C. Degen, F. Reinhard, et P. Cappellaro. "Quantum sensing." *Reviews of Modern Physics*, **89**, 035002 (2017).

[3] E. Diamanti, H.-K. Lo, B. Qi, et Z. Yuan. "Practical challenges in quantum key distribution." *npj Quantum Information*, **2**, 1 (2016).

[4] I. Georgescu, S. Ashhab, et F. Nori. "Quantum simulation." *Reviews of Modern Physics*, **86**, 153 (2014).

[5] T. D. Ladd, F. Jelezko, R. Laflamme, Y. Nakamura, C. Monroe, et J. L. O'Brien. "Quantum computers." *Nature*, **464**, 45 (2010).

[6] B. P. Lanyon, *et al.* "Universal Digital Quantum Simulation with Trapped Ions." *Science* (2011).

[7] H.-S. Zhong, *et al.* "Quantum computational advantage using photons." *Science* (2020).

[8] J. Clarke et F. K. Wilhelm. "Superconducting quantum bits." *Nature*, **453**, 1031 (2008).

[9] T. F. Watson, *et al.* "A programmable two-qubit quantum processor in silicon." *Nature*, **555**, 633 (2018).

[10] P. Lodahl. "Quantum-dot based photonic quantum networks." *Quantum Science and Technology*, **3**, 013001 (2018).

[11] A. Morello, *et al.* "Single-shot readout of an electron spin in silicon." *Nature*, **467**, 687 (2010).

[12] G. Zhang, Y. Cheng, J.-P. Chou, et A. Gali. "Material platforms for defect qubits and single-photon emitters." *Applied Physics Reviews*, **7**, 031308 (2020).

[13] A. Gruber, A. Dräbenstedt, C. Tietz, L. Fleury, J. Wrachtrup, et C. von Borczyskowski. "Scanning Confocal Optical Microscopy and Magnetic Resonance on Single Defect Centers." *Science*, **276**, 2012 (1997).

[14] A. Beveratos, R. Brouri, T. Gacoin, A. Villing, J.-P. Poizat, et P. Grangier. "Single Photon Quantum Cryptography." *Physical Review Letters*, **89**, 187901 (2002).

[15] G. Balasubramanian, *et al.* "Ultralong spin coherence time in isotopically engineered diamond." *Nature Materials*, **8**, 383 (2009).

[16] J. M. Taylor, *et al.* "High-sensitivity diamond magnetometer with nanoscale resolution." *Nature Physics*, **4**, 810 (2008).

[17] F. Dolde, *et al.* "Electric-field sensing using single diamond spins." *Nature Physics*, **7**, 459 (2011).

[18] D. M. Toyli, C. F. de las Casas, D. J. Christle, V. V. Dobrovitski, et D. D. Awschalom. "Fluorescence thermometry enhanced by the quantum coherence of single spins in diamond." *Proceedings of the National Academy of Sciences of the United States of America*, **110**, 8417 (2013).

[19] M. Lesik, *et al.* "Magnetic measurements on micrometer-sized samples under high pressure using designed NV centers." *Science*, **366**, 1359 (2019).

[20] M. Rollo, A. Finco, R. Tanos, F. Fabre, T. Devolder, I. Robert-Philip, et V. Jacques. "Quantitative study of the response of a single NV defect in diamond to magnetic noise." *Physical Review B*, **103**, 235418 (2021).

[21] M. Munsch. "NV magnetometry." Technical report, Qnami (2020). White paper.

[22] C. Bradley, *et al.* "A Ten-Qubit Solid-State Spin Register with Quantum Memory up to One Minute." *Physical Review X*, **9**, 031045 (2019).

[23] M. Pompili, *et al.* "Realization of a multinode quantum network of remote solid-state qubits." *Science*, **372**, 259 (2021).

[24] D. J. Christle, *et al.* "Isolated electron spins in silicon carbide with millisecond coherence times." *Nature Materials*, **14**, 160 (2015).

[25] W. F. Koehl, H. Seo, G. Galli, et D. D. Awschalom. "Designing defect spins for wafer-scale quantum technologies." *MRS Bulletin*, **40**, 1146 (2015).

[26] A. J. Morfa, B. C. Gibson, M. Karg, T. J. Karle, A. D. Greentree, P. Mulvaney, et S. Tomljenovic-Hanic. "Single-Photon Emission and Quantum Characterization of Zinc Oxide Defects." *Nano Letters*, **12**, 949 (2012).

[27] A. M. Berhane, *et al.* "Bright Room-Temperature Single-Photon Emission from Defects in Gallium Nitride." *Advanced Materials*, **29**, 1605092 (2017).

[28] M. Toth et I. Aharonovich. "Single Photon Sources in Atomically Thin Materials." *Annual Review of Physical Chemistry*, **70**, 123 (2019).

[29] Y. He, S. K. Gorman, D. Keith, L. Kranz, J. G. Keizer, et M. Y. Simmons. "A two-qubit gate between phosphorus donor electrons in silicon." *Nature*, **571**, 371 (2019).

[30] A. M. J. Zwerver, *et al.* "Qubits made by advanced semiconductor manufacturing." *arXiv:2101.12650 [cond-mat, physics:quant-ph]* (2021).

[31] M. Steger, *et al.* "Quantum Information Storage for over 180 s Using Donor Spins in a 28Si "Semiconductor Vacuum"." *Science*, **336**, 1280 (2012).

[32] K. J. Morse, *et al.* "A photonic platform for donor spin qubits in silicon." *Science Advances*, **3**, e1700930 (2017).

[33] J. W. Silverstone, D. Bonneau, J. L. O'Brien, et M. G. Thompson. "Silicon Quantum Photonics." *IEEE Journal of Selected Topics in Quantum Electronics*, **22**, 390 (2016).

[34] X. Qiang, *et al.* "Large-scale silicon quantum photonics implementing arbitrary two-qubit processing." *Nature Photonics*, **12**, 534 (2018).

[35] G. Davies. "The optical properties of luminescence centres in silicon." *Physics Reports*, **176**, 83 (1989).

[36] L. Bergeron, *et al.* "Silicon-Integrated Telecommunications Photon-Spin Interface." *PRX Quantum*, **1**, 020301 (2020).

[37] A. T. K. Kurkjian, *et al.* "Optical observation of single spins in silicon." *arXiv:2103.07580 [quant-ph]* (2021).

[38] M. A. Hughes, *et al.* "Coupling of Erbium-Implanted Silicon to a Superconducting Resonator." *Physical Review Applied*, **16**, 034006 (2021).

[39] C. Beaufils, *et al.* "Optical properties of an ensemble of G-centers in silicon." *Physical Review B*, **97**, 035303 (2018).

[40] K. M. Lee, K. P. O'Donnell, J. Weber, B. C. Cavenett, et G. D. Watkins. "Optical Detection of Magnetic Resonance for a Deep-Level Defect in Silicon." *Physical Review Letters*, **48**, 37 (1982).

[41] K. P. O'Donnell, K. M. Lee, et G. D. Watkins. "Origin of the 0.97 eV luminescence in irradiated silicon." *Physica B+C*, **116**, 258 (1983).

[42] G. Waldherr, *et al.* "Quantum error correction in a solid-state hybrid spin register." *Nature*, **506**, 204 (2014).

[43] B. Hensen, *et al.* "Loophole-free Bell inequality violation using electron spins separated by 1.3 kilometres." *Nature*, **526**, 682 (2015).

[44] A. Gali. "Theory of the neutral nitrogen-vacancy center in diamond and its application to the realization of a qubit." *Physical Review B*, **79**, 235210 (2009).

[45] A. Gali. “Ab initio theory of the nitrogen-vacancy center in diamond.” *Nanophotonics*, **8**, 1907 (2019).

[46] G. Waldherr, *et al.* “Dark States of Single Nitrogen-Vacancy Centers in Diamond Unraveled by Single Shot NMR.” *Physical Review Letters*, **106**, 157601 (2011).

[47] K. Y. Han, D. Wildanger, E. Rittweger, J. Meijer, S. Pezzagna, S. W. Hell, et C. Eggeling. “Dark state photophysics of nitrogen–vacancy centres in diamond.” *New Journal of Physics*, **14**, 123002 (2012).

[48] N. Aslam, G. Waldherr, P. Neumann, F. Jelezko, et J. Wrachtrup. “Photo-induced ionization dynamics of the nitrogen vacancy defect in diamond investigated by single-shot charge state detection.” *New Journal of Physics*, **15**, 013064 (2013).

[49] X.-D. Chen, L.-M. Zhou, C.-L. Zou, C.-C. Li, Y. Dong, F.-W. Sun, et G.-C. Guo. “Spin depolarization effect induced by charge state conversion of nitrogen vacancy center in diamond.” *Physical Review B*, **92**, 104301 (2015).

[50] L. Hacquebard et L. Childress. “Charge State Dynamics During Excitation and Depletion of the Nitrogen Vacancy Center in Diamond.” *Physical Review A*, **97** (2018).

[51] L. Razinkovas, M. Maciaszek, F. Reinhard, M. W. Doherty, et A. Alkauskas. “Photoionization of negatively charged NV centers in diamond: Theory and ab initio calculations.” *Physical Review B*, **104**, 235301 (2021).

[52] A. Batalov, *et al.* “Low Temperature Studies of the Excited-State Structure of Negatively Charged Nitrogen-Vacancy Color Centers in Diamond.” *Physical Review Letters*, **102**, 195506 (2009).

[53] L. Robledo, H. Bernien, T. v. d. Sar, et R. Hanson. “Spin dynamics in the optical cycle of single nitrogen-vacancy centres in diamond.” *New Journal of Physics*, **13**, 025013 (2011).

[54] A. Gupta, L. Hacquebard, et L. Childress. “Efficient signal processing for time-resolved fluorescence detection of nitrogen-vacancy spins in diamond.” *JOSA B*, **33**, B28 (2016).

[55] N. B. Manson, *et al.* “NV^-–N^+ pair centre in 1b diamond.” *New Journal of Physics*, **20**, 113037 (2018).

[56] L. Rondin, *et al.* “Surface-induced charge state conversion of nitrogen-vacancy defects in nanodiamonds.” *Physical Review B*, **82**, 115449 (2010).

[57] C. Schreyvogel, V. Polyakov, R. Wunderlich, J. Meijer, et C. E. Nebel. “Active charge state control of single NV centres in diamond by in-plane Al-Schottky junctions.” *Scientific Reports*, **5**, 12160 (2015).

[58] B. Shields, Q. Unterreithmeier, N. de Leon, H. Park, et M. Lukin. "Efficient Readout of a Single Spin State in Diamond via Spin-to-Charge Conversion." *Physical Review Letters*, **114**, 136402 (2015).

[59] K. Y. Han, S. K. Kim, C. Eggeling, et S. W. Hell. "Metastable Dark States Enable Ground State Depletion Microscopy of Nitrogen Vacancy Centers in Diamond with Diffraction-Unlimited Resolution." *Nano Letters*, **10**, 3199 (2010).

[60] S. Felton, A. M. Edmonds, M. E. Newton, P. M. Martineau, D. Fisher, et D. J. Twitchen. "Electron paramagnetic resonance studies of the neutral nitrogen vacancy in diamond." *Physical Review B*, **77**, 081201 (2008).

[61] A. Dréau. *Spins individuels dans le diamant pour l'information quantique.* thesis, Cachan, Ecole normale supérieure (2013).

[62] A. Jarmola, V. M. Acosta, K. Jensen, S. Chemerisov, et D. Budker. "Temperature- and Magnetic-Field-Dependent Longitudinal Spin Relaxation in Nitrogen-Vacancy Ensembles in Diamond." *Physical Review Letters*, **108**, 197601 (2012).

[63] D. Aude Craik, *et al.* "Microwave-Assisted Spectroscopy Technique for Studying Charge State in Nitrogen-Vacancy Ensembles in Diamond." *Physical Review Applied*, **14**, 014009 (2020).

[64] J. Happacher, *et al.* "Low temperature photo-physics of single NV centers in diamond." *arXiv:2105.08075 [cond-mat, physics:quant-ph]* (2021).

[65] R. S. Krishnan. "Raman Spectrum of Diamond." *Nature*, **155**, 171 (1945).

[66] M. L. Roberts, Reece P. an Juan et G. Molina-Terriza. "Spin-dependent charge state interconversion of nitrogen vacancy centers in nanodiamonds." *Physical Review B*, **99**, 174307 (2019).

[67] P. Neumann, *et al.* "Excited-state spectroscopy of single NV defects in diamond using optically detected magnetic resonance." *New Journal of Physics*, **11**, 013017 (2009).

[68] G. D. Watkins. "A review of EPR studies in irradiated silicon." In "Radiation Damage in Semiconductors," pages 97–113. International Conference on the Physics of Semiconductors, 7th, Paris, 1964, Dunod, Paris (1965).

[69] J. Krynicki et J. C. Bourgoin. "Defect annealing in phosphorus implanted silicon: A D.L.T.S. study." *Applied physics*, **18**, 275 (1979).

[70] A. J. Tavendale, A. A. Williams, et S. J. Pearton. "Hydrogen injection and neutralization of boron acceptors in silicon boiled in water." *Applied Physics Letters*, **48**, 590 (1986).

[71] R. H. Brown et R. Q. Twiss. "Correlation between Photons in two Coherent Beams of Light." *Nature*, **177**, 27 (1956).

[72] R. L. Price et W. G. J. Jerome, editors. *Basic Confocal Microscopy.* Springer New York, New York, NY (2011). ISBN 978-0-387-78174-7.

[73] J. M. Binder, *et al.* "Qudi: A modular python suite for experiment control and data processing." *SoftwareX*, **6**, 85 (2017).

[74] D.-X. Xu, *et al.* "Silicon Photonic Integration Platform—Have We Found the Sweet Spot?" *IEEE Journal of Selected Topics in Quantum Electronics*, **20**, 189 (2014).

[75] M. A. Green et M. J. Keevers. "Optical properties of intrinsic silicon at 300 K." *Progress in Photovoltaics: Research and Applications*, **3**, 189 (1995).

[76] A. Beveratos, S. Kühn, R. Brouri, T. Gacoin, J.-P. Poizat, et P. Grangier. "Room temperature stable single-photon source." *The European Physical Journal D - Atomic, Molecular, Optical and Plasma Physics*, **18**, 191 (2002).

[77] A. Beveratos, R. Brouri, T. Gacoin, J.-P. Poizat, et P. Grangier. "Nonclassical radiation from diamond nanocrystals." *Physical Review A*, **64**, 061802 (2001).

[78] C. C. Gerry et P. Knight. *Introductory quantum optics.* Cambridge University Press, Cambridge (2006). ISBN 978-0-521-52735-4.

[79] L. J. Martínez, T. Pelini, V. Waselowski, J. R. Maze, B. Gil, G. Cassabois, et V. Jacques. "Efficient single photon emission from a high-purity hexagonal boron nitride crystal." *Physical Review B*, **94**, 121405 (2016).

[80] E. Knill, R. Laflamme, et G. J. Milburn. "A scheme for efficient quantum computation with linear optics." *Nature*, **409**, 46 (2001).

[81] W. Redjem, *et al.* "Single artificial atoms in silicon emitting at telecom wavelengths." *Nature Electronics*, **3**, 738 (2020).

[82] R. John, J. Lehnert, M. Mensing, D. Spemann, S. Pezzagna, et J. Meijer. "Bright optical centre in diamond with narrow, highly polarised and nearly phonon-free fluorescence at room temperature." *New Journal of Physics*, **19**, 053008 (2017).

[83] V. D. Tkachev et A. V. Mudryi. "Piezospectroscopic effect on zero-phonon luminescence lines of silicon." *Journal of Applied Spectroscopy*, **29**, 1485 (1978).

[84] C. P. Anderson, *et al.* "Electrical and optical control of single spins integrated in scalable semiconductor devices." *Science*, **366**, 1225 (2019).

[85] M. Nirmal, B. O. Dabbousi, M. G. Bawendi, J. J. Macklin, J. K. Trautman, T. D. Harris, et L. E. Brus. "Fluorescence intermittency in single cadmium selenide nanocrystals." *Nature*, **383**, 802 (1996).

[86] J. P. Hoogenboom, J. Hernando, E. M. H. P. van Dijk, N. F. van Hulst, et M. F. García-Parajó. “Power-Law Blinking in the Fluorescence of Single Organic Molecules.” *ChemPhysChem*, **8**, 823 (2007).

[87] F. D. Stefani, J. P. Hoogenboom, et E. Barkai. “Beyond quantum jumps: Blinking nanoscale light emitters.” *Physics Today*, **62**, 34 (2009).

[88] C. Eggeling, J. Widengren, R. Rigler, et C. A. M. Seidel. “Photobleaching of Fluorescent Dyes under Conditions Used for Single-Molecule Detection: Evidence of Two-Step Photolysis.” *Analytical Chemistry*, **70**, 2651 (1998).

[89] R. J. Elliott, I. G. Matthew, et E. W. J. Mitchell. “The polarization of luminescence in diamond.” *Philosophical Magazine*, **3**, 360 (1958).

[90] S. Schmitt, G. Sarau, et S. Christiansen. “Observation of strongly enhanced photoluminescence from inverted cone-shaped silicon nanostructures.” *Scientific Reports*, **5**, 17089 (2015).

[91] S. Cueff, *et al.* “Tailoring the Local Density of Optical States and Directionality of Light Emission by Symmetry Breaking.” *IEEE Journal of Selected Topics in Quantum Electronics*, **25**, 1 (2019).

[92] L. Weiss, A. Gritsch, B. Merkel, et A. Reiserer. “Erbium dopants in nanophotonic silicon waveguides.” *Optica*, **8**, 40 (2021).

[93] A. Beveratos. “Réalisation expérimentale d’une source de photons uniques par fluorescence de centres colorés individuels dans le diamant ; application à la cryptographie quantique.” (2002).

[94] S. C. Kitson, P. Jonsson, J. Rarity, et P. Tapster. “Intensity fluctuation spectroscopy of small numbers of dye molecules in a microcavity.” *Physical Review A*, **58**, 620 (1998).

[95] A. Beveratos, R. Brouri, J.-P. Poizat, et P. Grangier. “Bunching and Antibunching from Single NV Color Centers in Diamond.” In P. Tombesi et O. Hirota, editors, “Quantum Communication, Computing, and Measurement 3,” pages 261–267. Springer US, Boston, MA (2002). ISBN 978-0-306-47114-8.

[96] H. Benisty, R. Stanley, et M. Mayer. “Method of source terms for dipole emission modification in modes of arbitrary planar structures.” *JOSA A*, **15**, 1192 (1998).

[97] K. Thonke, A. Teschner, et R. Sauer. “New photoluminescence defect spectra in silicon irradiated at 100 K: Observation of interstitial carbon?” *Solid State Communications*, **61**, 241 (1987).

[98] P. Pichler. *Intrinsic Point Defects, Impurities, and Their Diffusion in Silicon.* Computational Microelectronics. Springer-Verlag, Wien (2004). ISBN 978-3-211-20687-4.

[99] S. K. Estreicher, D. West, J. Goss, S. Knack, et J. Weber. "First-Principles Calculations of Pseudolocal Vibrational Modes: The Case of Cu and Cu Pairs in Si." *Physical Review Letters*, **90**, 035504 (2003).

[100] A. Gulans, *et al.* "exciting: a full-potential all-electron package implementing density-functional theory and many-body perturbation theory." *Journal of Physics: Condensed Matter*, **26**, 363202 (2014).

[101] E. M. Purcell, H. C. Torrey, et R. V. Pound. "Resonance Absorption by Nuclear Magnetic Moments in a Solid." *Physical Review*, **69**, 37 (1946).

[102] M. Hollenbach, *et al.* "Engineering telecom single-photon emitters in silicon for scalable quantum photonics." *Optics Express*, **28**, 26111 (2020).

[103] S. M. Buckley, *et al.* "Optimization of photoluminescence from W centers in silicon-on-insulator." *Optics Express*, **28**, 16057 (2020).

[104] C. Chartrand, *et al.* "Highly enriched $^{28}\mathrm{Si}$ reveals remarkable optical linewidths and fine structure for well-known damage centers." *Physical Review B*, **98**, 195201 (2018).

[105] A. Bourassa, *et al.* "Entanglement and control of single nuclear spins in isotopically engineered silicon carbide." *Nature Materials*, **19**, 1319 (2020).

[106] L. T. Canham, K. G. Barraclough, et D. J. Robbins. "1.3-um light-emitting diode from silicon electron irradiated at its damage threshold." *Applied Physics Letters*, **51**, 1509 (1987).

[107] E. Rotem, J. M. Shainline, et J. M. Xu. "Enhanced photoluminescence from nanopatterned carbon-rich silicon grown by solid-phase epitaxy." *Applied Physics Letters*, **91**, 051127 (2007).

[108] S. G. Cloutier, P. A. Kossyrev, et J. Xu. "Optical gain and stimulated emission in periodic nanopatterned crystalline silicon." *Nature Materials*, **4**, 887 (2005).

[109] A. Docaj et S. K. Estreicher. "Three carbon pairs in Si." *Physica B: Condensed Matter*, **407**, 2981 (2012).

[110] H. Wang, A. Chroneos, C. A. Londos, E. N. Sgourou, et U. Schwingenschlögl. "G-centers in irradiated silicon revisited: A screened hybrid density functional theory approach." *Journal of Applied Physics*, **115**, 183509 (2014).

[111] D. Timerkaeva, C. Attaccalite, G. Brenet, D. Caliste, et P. Pochet. "Structural, electronic, and optical properties of the C-C complex in bulk silicon from first principles." *Journal of Applied Physics*, **123**, 161421 (2018).

[112] P. Udvarhelyi, B. Somogyi, G. Thiering, et A. Gali. “Identification of a Telecom Wavelength Single Photon Emitter in Silicon.” *Physical Review Letters*, **127**, 196402 (2021).

[113] M. Afanasjev, R. Laiho, L. Vlasenko, et M. Vlasenko. “Thermally activated change of symmetry of carbon related center in irradiated silicon.” *Solid State Communications*, **102**, 595 (1997).

[114] K. Thonke, H. Klemisch, J. Weber, et R. Sauer. “New model of the irradiat(aion-induced 0.97-eV (G) line in silicon: A ${\mathrm{C}}_{S}\ensuremath{-}{\mathrm{Si}}^{*}$ complex.” *Physical Review B*, **24**, 5874 (1981).

[115] P. Becker, H.-J. Pohl, H. Riemann, et N. Abrosimov. “Enrichment of silicon for a better kilogram.” *physica status solidi (a)*, **207**, 49 (2010).

[116] “Chapter 7 - Silicium.” In P. A. de Groot, editor, “Handbook of Stable Isotope Analytical Techniques,” page 619. Elsevier, Amsterdam (2009). ISBN 978-0-444-51115-7.

[117] G. Davies, Kwok Tat Kun, et T. Reade. “Annealing kinetics of the dicarbon radiation-damage center in crystalline silicon.” *Physical Review B*, **44**, 12146 (1991).

[118] A. K. Tipping et R. C. Newman. “The diffusion coefficient of interstitial carbon in silicon.” *Semiconductor Science and Technology*, **2**, 315 (1987).

[119] C. E. Jones et W. D. Compton. “Recombination luminescence in irradiated silicon-effects of uniaxial stress and temperature variations †.” *Radiation Effects*, **9**, 83 (1971).

[120] C. P. Foy, M. C. d. Carmo, G. Davies, et E. C. Lightowlers. “Uniaxial stress measurements on the 0.97 eV line in irradiated silicon.” *Journal of Physics C: Solid State Physics*, **14**, L7 (1981).

[121] P. A. Stolk, *et al.* “Physical mechanisms of transient enhanced dopant diffusion in ion-implanted silicon.” *Journal of Applied Physics*, **81**, 6031 (1997).

[122] B. C. MacEvoy et S. J. Watts. “Defect Engineering Radiation Tolerant Silicon Detectors.” *Solid State Phenomena*, **57-58**, 221 (1997).

[123] M. Moll. “Displacement Damage in Silicon Detectors for High Energy Physics.” *IEEE Transactions on Nuclear Science*, **65**, 1561 (2018).

[124] A. Durand, *et al.* “Broad Diversity of Near-Infrared Single-Photon Emitters in Silicon.” *Physical Review Letters*, **126**, 083602 (2021).

[125] D. Pierreux et A. Stesmans. “Electron spin resonance study of paramagnetic centers in neutron-irradiated heat-treated silicon.” *Physical Review B*, **71**, 115204 (2005).

[126] B. Surma, P. Kaminski, A. Wnuk, et R. Kozlowski. “Some new photoluminescence features of W line for neutron-irradiated MCz-Si and FZ-Si.” In “2008 IEEE Nuclear Science Symposium Conference Record,” pages 2561–2564 (2008).

[127] M. Skolnick, A. Cullis, et H. Webber. "Defect photoluminescence from Si laser annealed over a wide temperature range." *Journal of Luminescence*, **24-25**, 39 (1981).

[128] J. Bao, M. Tabbal, T. Kim, S. Charnvanichborikarn, J. S. Williams, M. J. Aziz, et F. Capasso. "Point defect engineered Si sub-bandgap light-emitting diode." *Optics Express*, **15**, 6727 (2007).

[129] S. Buckley, *et al.* "All-silicon light-emitting diodes waveguide-integrated with superconducting single-photon detectors." *Applied Physics Letters*, **111**, 141101 (2017).

[130] A. N. Tait, *et al.* "Microring resonator-coupled photoluminescence from silicon W centers." *Journal of Physics: Photonics*, **2**, 045001 (2020).

[131] Y.-C. Chen, *et al.* "Laser writing of coherent colour centres in diamond." *Nature Photonics*, **11**, 77 (2017).

[132] Y.-C. Chen, *et al.* "Laser writing of individual nitrogen-vacancy defects in diamond with near-unity yield." *Optica*, **6**, 662 (2019).

[133] J. F. Ziegler, M. D. Ziegler, et J. P. Biersack. "SRIM - The stopping and range of ions in matter (2010)." *Nuclear Instruments and Methods in Physics Research B*, **268**, 1818 (2010).

[134] N. S. Minaev, A. V. Mudrii, et V. D. Tkachev. "Symmetry and Nature of the 1.0186 eV Luminescence Centre in Neutron - Irradiated Silicon." *physica status solidi (b)*, **108**, K89 (1981).

[135] B. J. Coomer, J. P. Goss, R. Jones, S. Öberg, et P. R. Briddon. "Interstitial aggregates and a new model for the I1/W optical centre in silicon." *Physica B: Condensed Matter*, **273-274**, 505 (1999).

[136] M. Gharaibeh, S. K. Estreicher, et P. A. Fedders. "Molecular-dynamics studies of self-interstitial aggregates in Si." *Physica B: Condensed Matter*, **273-274**, 532 (1999).

[137] R. Jones, T. A. G. Eberlein, N. Pinho, B. J. Coomer, J. P. Goss, P. R. Briddon, et S. Öberg. "Self-interstitial clusters in silicon." *Nuclear Instruments and Methods in Physics Research Section B: Beam Interactions with Materials and Atoms*, **186**, 10 (2002).

[138] D. A. Richie, J. Kim, S. A. Barr, K. R. A. Hazzard, R. Hennig, et J. W. Wilkins. "Complexity of Small Silicon Self-Interstitial Defects." *Phys. Rev. Lett.*, **92**, 045501 (2004).

[139] A. Carvalho, R. Jones, J. Coutinho, et P. R. Briddon. "Density-functional study of small interstitial clusters in Si: Comparison with experiments." *Phys. Rev. B*, **72**, 155208 (2005).

[140] I. Santos, M. Aboy, P. López, L. A. Marqués, et L. Pelaz. "Insights on the atomistic origin of X and W photoluminescence lines in c-Si from ab initio simulations." *Journal of Physics D: Applied Physics*, **49**, 075109 (2016).

[141] Y. Baron, *et al.* “Detection of single W-centers in silicon.” *arXiv:2108.04283 [physics, physics:quant-ph]* (2021).

[142] J. Wang, *et al.* “Scalable Fabrication of Single Silicon Vacancy Defect Arrays in Silicon Carbide Using Focused Ion Beam.” *ACS Photonics*, **4**, 1054 (2017).

[143] S. Lindner, *et al.* “Strongly inhomogeneous distribution of spectral properties of silicon-vacancy color centers in nanodiamonds.” *New Journal of Physics*, **20** (2018).

[144] S. Li, *et al.* “Giant shift upon strain on the fluorescence spectrum of VNNB color centers in h-BN.” *npj Quantum Information*, **6**, 1 (2020).

[145] G. Davies, E. C. Lightowlers, et Z. E. Ciechanowska. “The 1018 meV (W or I1) vibronic band in silicon.” *Journal of Physics C: Solid State Physics*, **20**, 191 (1987).

[146] C. D. Clark, G. W. Maycraft, et E. W. J. Mitchell. “Polarization of Luminescence.” *Journal of Applied Physics*, **33**, 378 (2004).

[147] C. Lethiec, *et al.* “Measurement of Three-Dimensional Dipole Orientation of a Single Fluorescent Nanoemitter by Emission Polarization Analysis.” *Physical Review X*, **4**, 021037 (2014).

[148] K. Murata, Y. Yasutake, K.-i. Nittoh, S. Fukatsu, et K. Miki. “High-density G-centers, light-emitting point defects in silicon crystal.” *AIP Advances*, **1**, 032125 (2011).

[149] W. B. Gao, A. Imamoglu, H. Bernien, et R. Hanson. “Coherent manipulation, measurement and entanglement of individual solid-state spins using optical fields.” *Nature Photonics*, **9**, 363 (2015).

[150] C. K. Hong, Z. Y. Ou, et L. Mandel. “Measurement of subpicosecond time intervals between two photons by interference.” *Physical Review Letters*, **59**, 2044 (1987).

[151] B. Lounis et M. Orrit. “Single-photon sources.” *Reports on Progress in Physics*, **68**, 1129 (2005).

[152] L. Robledo, H. Bernien, I. van Weperen, et R. Hanson. “Control and Coherence of the Optical Transition of Single Nitrogen Vacancy Centers in Diamond.” *Physical Review Letters*, **105**, 177403 (2010).

[153] H. Bernien, L. Childress, L. Robledo, M. Markham, D. Twitchen, et R. Hanson. “Two-Photon Quantum Interference from Separate Nitrogen Vacancy Centers in Diamond.” *Physical Review Letters*, **108**, 043604 (2012).

[154] D. D. Awschalom, R. Hanson, J. Wrachtrup, et B. B. Zhou. “Quantum technologies with optically interfaced solid-state spins.” *Nature Photonics*, **12**, 516 (2018).

[155] W. M. Chen et B. Monemar. “Role of free carriers in the application of optically detected magnetic resonance for studies of defects in silicon.” *Applied Physics A Solids and Surfaces*, **53**, 130 (1991).

[156] H. Weman, Q. X. Zhao, et B. Monemar. “Impact ionization of excitons and electron-hole droplets in silicon.” *Physical Review B*, **36**, 5054 (1987).

[157] A. E. Morishige, M. A. Jensen, D. B. Needleman, K. Nakayashiki, J. Hofstetter, T.-T. A. Li, et T. Buonassisi. “Lifetime Spectroscopy Investigation of Light-Induced Degradation in p-type Multicrystalline Silicon PERC.” *IEEE Journal of Photovoltaics*, **6**, 1466 (2016).

[158] J. M. Shainline. “Optoelectronic intelligence.” *Applied Physics Letters*, **118**, 160501 (2021).

[159] G. K. Wertheim et W. M. Augustyniak. “Measurement of Short Carrier Lifetimes.” *Review of Scientific Instruments*, **27**, 1062 (1956).

[160] G. K. Wertheim. “Energy Levels in Electron-Bombarded Silicon.” *Physical Review*, **105**, 1730 (1957).

[161] G. Bemski. “Paramagnetic Resonance in Electron Irradiated Silicon.” *Journal of Applied Physics*, **30**, 1195 (1959).

[162] G. D. Watkins, J. W. Corbett, et R. M. Walker. “Spin Resonance in Electron Irradiated Silicon.” *Journal of Applied Physics*, **30**, 1198 (1959).

[163] A. V. Yukhnevich. “The structure of the spectrum of radiative capture of holes by the a-center in silicon.” *Fiz. Tverd. Tela*, **Vol: 7** (1965).

[164] J. Walker. “Comments on “Luminescence from electron-irradiated silicon”.” *Journal of Applied Physics*, **45**, 4653 (1974).

[165] J. R. Noonan, C. G. Kirkpatrick, et B. G. Streetman. “Photoluminescence from Si irradiated with 1.5-MeV electrons at 100K.” *Journal of Applied Physics*, **47**, 3010 (1976).

[166] K. L. Brower. “EPR of a Jahn-Teller distorted (111) carbon interstitialcy in irradiated silicon.” *Physical Review B*, **9**, 2607 (1974).

[167] H. C. Wolf. “ODMR-Spektroskopie: Triplet State ODMR Spectroscopy. Techniques and Applications to Biophysical Systems.” *Nachrichten aus Chemie, Technik und Laboratorium*, **30**, 947 (1982).

[168] G. Davies, E. C. Lightowlers, et M. d. Carmo. “Carbon-related vibronic bands in electron-irradiated silicon.” *Journal of Physics C: Solid State Physics*, **16**, 5503 (1983).

[169] M. X. Yan, K. P. Homewood, et B. C. Cavenett. “PDMR and ODMR crystalline p $^+$ -i-n $^+$ silicon diodes.” *Journal of Physics C: Solid State Physics*, **19**, L189 (1986).

[170] P. Siyushev, *et al.* “Photoelectrical imaging and coherent spin-state readout of single nitrogen-vacancy centers in diamond.” *Science*, **363**, 728 (2019).

[171] L. W. Song, X. D. Zhan, B. W. Benson, et G. D. Watkins. “Bistable interstitial-carbon–substitutional-carbon pair in silicon.” *Physical Review B*, **42**, 5765 (1990).

Abstract

Being able to control the physical properties of individual quantum systems has triggered the boom of the field of quantum technologies aimed at creating new components and machines with functionalities unmatched by conventional physical systems. Among the quantum systems studied, the optically active point defects in semiconductors have the advantage of behaving like artificial atoms in the solid state. Isolated on an individual scale, they exhibit an emission of single photons that can be used for quantum communications. Some defects also have a controllable electronic spin that can serve as a quantum memory and a nanoscale quantum sensor. The NV center of diamond is currently by far the most studied fluorescent defect because its quantum properties can be exploited at room temperature. However, the ideal platform for developing large-scale technologies is silicon. Still, this semiconductor was left out because of its low bandgap energy. In fact, no optically active defect had been detected in it at the start of this thesis.

After initial work on the NV center and its state of charge conversion dynamics, the core of this thesis was devoted to the study of fluorescent defects in silicon to be able to isolate them on an individual scale. This objective first required the development of a new optical microscopy setup at low temperature, optimized for the near infrared. The first efforts were devoted to the detection of a defect based on carbon impurities, called the G center, which exhibits an optical emission at telecom wavelengths suitable for propagation in optical fibers, and potentially advantageous spin properties for quantum technologies. The exploration of carbon-implanted silicon samples enabled the detection of single G centers, but also uncovered seven other families of individual fluorescent defects not listed in the literature on ensemble measurements. In parallel, individual defects associated with a complex of interstitial silicon atoms were also observed in another silicon sample. The analysis of the emission of single photons from these different emitters, as well as their optical spectroscopy, made it possible to determine properties inaccessible on the ensemble measurements.

The detection of individual optically active defects in silicon opens a new path for quantum technologies in this learning material of the semiconductor industry. One of the next challenges will be to demonstrate the control of the spin states associated with these unique defects. Beyond quantum applications, the study at the individual scale of fluorescent silicon defects could also bring new discoveries on these systems of both fundamental and applied interest.

Résumé

Pouvoir contrôler les propriétés physiques de systèmes quantiques individuels a déclenché l'essor du domaine des technologies quantiques visant à créer de nouveaux composants et machines aux fonctionnalités inégalables par des systèmes physiques classiques. Parmi les systèmes quantiques étudiés, les défauts ponctuels optiquement actifs des semiconducteurs ont l'avantage de se comporter comme des atomes artificiels à l'état solide. Isolés à l'échelle individuelle, ils présentent une émission de photons uniques pouvant être utilisée pour réaliser des communications quantiques. Certains défauts possèdent également un spin électronique contrôlable qui peut servir de mémoire quantique et de capteur quantique nanométrique. Le centre NV du diamant est actuellement le défaut fluorescent de loin le plus étudié car ses propriétés quantiques peuvent être exploitées à température ambiante. Cependant, la plateforme idéale pour développer des technologies à large échelle est le silicium. Ce semiconducteur a toutefois été laissé de côté en raison de sa faible énergie de bande interdite. De fait, aucun défaut optiquement actif n'y avait été détecté de façon individuelle au début de cette thèse.

Après de premiers travaux sur le centre NV et sa dynamique de conversion d'état de charge, le cœur de cette thèse a été consacré à l'étude des défauts fluorescents dans le silicium pour pouvoir les isoler à l'échelle individuelle. Cet objectif a d'abord requis le développement d'un nouveau montage de microscope optique à froid, optimisé pour le proche infrarouge. Les premiers efforts ont été consacrés à la détection d'un défaut à base d'impuretés de carbone, appelé le centre G, qui présente une émission optique aux longueurs d'onde télécom adaptées à la propagation dans les fibres optiques et des propriétés de spin potentiellement avantageuses pour les technologies quantiques. L'exploration d'échantillons de silicium implantés en carbone a permis de détecter des centres G uniques, mais également de mettre à jour sept autres familles de défauts fluorescents individuels non répertoriées dans la littérature sur les mesures d'ensembles. En parallèle, des défauts individuels associés à un complexe d'atomes de silicium interstitiels ont aussi été observés dans un autre échantillon de silicium. L'analyse de l'émission de photons uniques de ces différents émetteurs ainsi que leur spectroscopie optique ont permis de mettre en évidence des propriétés inaccessibles sur les mesures réalisées à partir d'ensembles de défauts.

La détection de défauts individuels optiquement actifs dans le silicium ouvre une nouvelle voie d'exploration pour les technologies quantiques dans ce matériau majeur de l'industrie des semiconducteurs. Un des prochains challenges sera notamment de démontrer le contrôle des états de spin associés à ces défauts uniques. Au-delà des applications quantiques, l'étude à l'échelle individuelle des défauts fluorescents du silicium pourrait également apporter de nouvelles découvertes sur ces systèmes d'intérêt à la fois fondamental et appliqué.